

INFORMATION TO USERS

This was produced from a copy of a document sent to us for microfilming. While the most advanced technological means to photograph and reproduce this document have been used, the quality is heavily dependent upon the quality of the material submitted.

The following explanation of techniques is provided to help you understand markings or notations which may appear on this reproduction.

1. The sign or "target" for pages apparently lacking from the document photographed is "Missing Page(s)". If it was possible to obtain the missing page(s) or section, they are spliced into the film along with adjacent pages. This may have necessitated cutting through an image and duplicating adjacent pages to assure you of complete continuity.
2. When an image on the film is obliterated with a round black mark it is an indication that the film inspector noticed either blurred copy because of movement during exposure, or duplicate copy. Unless we meant to delete copyrighted materials that should not have been filmed, you will find a good image of the page in the adjacent frame. If copyrighted materials were deleted you will find a target note listing the pages in the adjacent frame.
3. When a map, drawing or chart, etc., is part of the material being photographed the photographer has followed a definite method in "sectioning" the material. It is customary to begin filming at the upper left hand corner of a large sheet and to continue from left to right in equal sections with small overlaps. If necessary, sectioning is continued again—beginning below the first row and continuing on until complete.
4. For any illustrations that cannot be reproduced satisfactorily by xerography, photographic prints can be purchased at additional cost and tipped into your xerographic copy. Requests can be made to our Dissertations Customer Services Department.
5. Some pages in any document may have indistinct print. In all cases we have filmed the best available copy.

University
Microfilms
International

300 N. ZEEB RD., ANN ARBOR, MI 48106

8219169

Wagner, John Scott

A COMPUTER SIMULATION OF AURORAL ARC FORMATION

University of Alaska

PH.D. 1981

University
Microfilms
International

300 N. Zeeb Road, Ann Arbor, MI 48106

Copyright 1982

by

Wagner, John Scott

All Rights Reserved

PLEASE NOTE:

In all cases this material has been filmed in the best possible way from the available copy. Problems encountered with this document have been identified here with a check mark .

1. Glossy photographs or pages
2. Colored illustrations, paper or print _____
3. Photographs with dark background
4. Illustrations are poor copy _____
5. Pages with black marks, not original copy _____
6. Print shows through as there is text on both sides of page _____
7. Indistinct, broken or small print on several pages _____
8. Print exceeds margin requirements _____
9. Tightly bound copy with print lost in spine _____
10. Computer printout pages with indistinct print _____
11. Page(s) _____ lacking when material received, and not available from school or author.
12. Page(s) _____ seem to be missing in numbering only as text follows.
13. Two pages numbered _____, Text follows.
14. Curling and wrinkled pages _____
15. Other _____

University
Microfilms
International

A COMPUTER SIMULATION OF AURORAL ARC FORMATION

A
THESIS

Presented to the Faculty of the University of Alaska
in Partial Fulfillment of the Requirements
for the Degree of

Doctor of Philosophy

By
John S. Wagner, B.S., M.S.

Fairbanks, Alaska

May 1981

A COMPUTER SIMULATION OF AURORAL ARC FORMATION

RECOMMENDED:

Mr. Rowden

Dr. P. R. I.

Dr. H. Free.

Mr. R. Kan

Chairman, Advisory Committee

Head, Space Physics and Atmospheric Sciences Program

Head, Space Physics and Atmospheric Sciences Program

Mr. Rowden

Director, Division of Geosciences

APPROVED:

K. B. Barber
Vice Chancellor for Research and Advanced Study

May 3, 1981
Date

Abstract

Recent satellite measurements have revealed two intriguing features associated with the formation of auroral arcs. The first is that an auroral arc is produced by a sheet of electrons accelerated along a geomagnetic field-aligned potential drop, and the second is that these electrons carry a field-aligned, upward-directed electric current. In order to explain these measurements, a self-consistent, time-dependent, computer simulation of auroral arc formation has been developed. The simulation demonstrates for the first time that a stable V-shaped potential structure, called an auroral double layer, develops spontaneously as a result of an ion-shielded electron current sheet interacting with a conducting ionosphere. The double layer accelerates current-carrying electrons into the upper atmosphere at auroral energies. The double layer potential depends critically on the drift speed of the current-carrying electrons and on the temperature of the ambient shielding ions. Localized double layers occur near the ionosphere when the geomagnetic field is assumed to be uniform, but, when a converging magnetic field is introduced, the double layer becomes extended due to the presence of an additional population of electrons trapped between the magnetic mirror and the double layer potential. The simulated auroral current sheet is subject to auroral curl and fold-type deformations due to unstable Kelvin-Helmholtz waves. The previously incompletely understood auroral fold-producing mechanism is described.

Acknowledgements

I was very fortunate to have the support of my parents and family throughout these past years of arctic madness. The adventure is ending with a very special appreciation of Hickories, Oaks, fields of corn, the Skunk River and good old home cooking. This thesis would still be a scrambled mess of notes if it weren't for the generous help and gentle (but often) prodding of Sandra Stephens. Thanks are due to my advisor, Professor S.-I. Akasofu for constant help, but the freedom to work independently on the problems of my choice. I would like to thank Professor Joe Kan for rescuing me many years ago and getting me started on the auroral arc problem. Much of the work was done at UCLA, where I learned plasma simulation from my friends Professor Toshi Tajima and Dr. Jean-Noel Leboeuf.

Table of Contents

Abstract.....	iii
Acknowledgements.....	iv
Table of Contents.....	v
List of Figures.....	viii
List of Tables.....	xvi
1.0 Introduction.....	1
1.1 Morphology of Auroral Arcs.....	2
1.2 The Optical Aurora.....	8
1.3 Auroral Acceleration Mechanisms.....	15
1.3.1 Double Layers.....	18
1.3.2 Electrostatic Shocks.....	22
1.3.3 Pitch Angle Anisotropy.....	24
1.3.4 Anomalous Resistivity.....	25
1.3.5 Thermoelectric Effect.....	27
1.3.6 Alfvén Waves.....	27
2.0 Plasma Simulation Techniques Applied to Space Physics.....	28
2.1 Historical Background for Particle Simulation.....	33
2.2 Finite Size Particles.....	37
2.3 The Solution to Poisson's Equation.....	41

2.3.1	Description of the Superposition Technique for a Bounded Poisson Solver.....	43
2.3.2	Description of the Bounded Fourier Poisson Solver....	46
2.4	Particle Handling at the Boundaries.....	48
3.0	Simulation of Two-Dimensional V-Potential Double Layers.....	50
3.1	V-Potential Double Layers in a Uniform Magnetic Field.....	57
3.2	V-Potential Double Layers in a Dipole Mirror Field.....	63
3.2.1	The $v_d = 0$ Case.....	65
3.2.2	The $v_d = 0.75$ Case.....	73
3.3	The Effects of a Background Plasma on Double Layer Formation in a Dipole Mirror Field.....	81
3.3.1	The Simulation at $\tau = 40\omega_{pe}^{-1}$	83
3.3.2	The Simulation at $\tau = 120\omega_{pe}^{-1}$	87
3.3.3	The Simulation at $\tau = 200\omega_{pe}^{-1}$	92
3.3.4	The Simulation at $\tau = 320\omega_{pe}^{-1}$	96
3.3.5	The Simulation at $\tau = 400\omega_{pe}^{-1}$	96
3.3.6	The Evolution of the Velocity Distribution Functions in Time.....	104
3.4	Simulation Summary.....	109
4.0	Simulation of Small Scale Auroral Arc Deformations.....	111
4.1	The Formation of Auroral Curls.....	123
4.2	The Formation of Auroral Folds.....	131

5.0 Conclusion.....	153
5.1 Summary of Work Done.....	153
5.2 Suggestion for Future Research.....	157
References.....	159

List of Figures

- Figure 1.1 The two principal planes containing the auroral electron current sheet. One plane contains the V-shaped potential structure and the other contains the small scale deformations known as curls or folds.....3
- Figure 1.2 Diagram showing distribution of electron precipitation across polar cap with the resulting displays of discrete and diffuse auroras.....7
- Figure 1.3 Schematic processes leading to the optical aurora.....10
- Figure 2.1 Schematic diagram showing parameter regimes of space, ionospheric, and laboratory plasmas.....29
- Figure 2.2 Basic structure of an electrostatic simulation code using finite size particles and a computational grid for the solution of Poisson's equation.....32
- Figure 2.3 An illustration of the relationship between the computational grid for the solution of Poisson's equation.....38

Figure 3.1	The initial and boundary conditions used for the V-potential simulation.....	52
Figure 3.2	Double layers at $t = 2500\omega_{pe}^{-1}$. (a)-(c) $T_e/T_i = 0.2$; (d)-(f) $T_e/T_i = 0.6$	59
Figure 3.3	(a) The effective collision frequency as a function of temperature ratio.....	61
Figure 3.3	(b) The double layer voltage drop as a function of temperature ratio T_e/T_i	62
Figure 3.4	Properties of the double layer as a function of electron drift velocity $v_D(L)$	64
Figure 3.5	(a) The electron positions for a simulation including the mirror effects of a dipole field, at time $\tau = 400\omega_{pe}^{-1}$	66
	(b) The ion positions.....	67
	(c) The electron phase space $v(x)$ vs. x for this simulation.....	68
	(d) The ion phase space $V(x)$ vs. x for this simulation.....	69
	(e) Equipotential contours for the double layer.....	70

(f) The potential down the center of the current sheet.....	71
(g) Velocity distribution functions.....	74

Figure 3.6 (a) The electron position for a simulation including the mirror effects of a dipole field, at time $\tau = 400\omega_{pe}^{-1}$	75
(b) The ion positions for this simulation at the same time, $\tau = 400\omega_{pe}^{-1}$	76
(c) Electron phase space.....	77
(d) Ion phase space.....	79
(e), (f) Spatially integrated velocity distribution functions for the electrons.....	80
(g) Potential drop as a function of x down the center of the double layer.....	82

Figure 3.7 (a) The electron position at $\tau = 0.0\omega_{pe}^{-1}$ including the dipole field and a background plasma.	
(b) The initial ion positions.....	84

Figure 3.8 (a) Electron phase space at $\tau = 40\omega_{pe}^{-1}$.	
(b) Ion phase space at $\tau = 40\omega_{pe}^{-1}$	86

- Figure 3.9 (a) Electric potential contours at $\tau = 40\omega_{pe}^{-1}$, with a spacing of $\Delta\phi = 0.4T_e$.
 (b) The electric potential down the center of the current sheet.....88
- Figure 3.10 (a) Electron phase space at time $\tau = 120\omega_{pe}^{-1}$.
 (b) Ion phase space at time $\tau = 120\omega_{pe}^{-1}$90
- Figure 3.11 (a) Electric potential contours at $\tau = 120\omega_{pe}^{-1}$, with a separation of $\Delta\phi = 0.5T_e$.
 (b) The electric potential down the center of the double layer.....91
- Figure 3.12 (a) Electron positions at time $\tau = 200\omega_{pe}^{-1}$.
 (b) Ion positions at time $\tau = 200\omega_{pe}^{-1}$93
- Figure 3.13 (a) Electron phase space at time $\tau = 200\omega_{pe}^{-1}$.
 (b) Ion phase space at time $\tau = 200\omega_{pe}^{-1}$94
- Figure 3.14 (a) Potential contours at time $\tau = 200\omega_{pe}^{-1}$ spaced $\Delta\phi = 0.4T_e$ apart.
 (b) The potential down the center of the double layer at time $\tau = 200\omega_{pe}^{-1}$95

Figure 3.15	(a) Electron phase space at $\tau = 320\omega_{pe}^{-1}$.	
	(b) Ion phase space at $\tau = 320\omega_{pe}^{-1}$	97
Figure 3.16	(a) Potential contours at $\tau = 320\omega_{pe}^{-1}$ spaces $\Delta\phi = 0.6T_e$ apart.	
	(b) The potential down the center of the double layer at time $\tau = 320\omega_{pe}^{-1}$	98
Figure 3.17	(a) Electron positions at the final time $\tau = 400\omega_{pe}^{-1}$.	
	(b) Ion positions at the final time $\tau = 400\omega_{pe}^{-1}$	99
Figure 3.18	(a) The electron phase space at $\tau = 400\omega_{pe}^{-1}$.	
	(b) The ion phase space at $\tau = 400\omega_{pe}^{-1}$	101
Figure 3.19	(a) Electric potential contours at $\tau = 400\omega_{pe}^{-1}$	102
	(b) The electric potential down the center of the double layer at $\tau = 400\omega_{pe}^{-1}$	103
Figure 3.20	(a) Spatially integrated ion velocity distribution $f(v_x)$ vs. v_x function for five different times.....	105
	(b) Spatially integrated ion velocity distribution functions $f(v_y)$ vs. v_y	106

Figure 3.21	(a) The spatially integrated electron velocity distribution functions $f(v_x)$ vs. v_x	107
	(b) The spatially integrated electron velocity distribution functions $f(v_y)$ vs. v_y	108
Figure 4.1	The dispersion relationship for Kelvin-Helmholtz waves in an ion-shielded electron charge sheet.....	122
Figure 4.2	The electron guiding center positions as a function of time illustrating the formation of auroral curls.....	125
Figure 4.3	The ion positions as a function of time as they try to shield the electric field of the deforming electron sheet.....	126
Figure 4.4	The electric potential contours at various times during the formation of auroral curls.....	128
Figure 4.5	A T.V. picture of auroral curl formation.....	129
Figure 4.6	Time history of the ion kinetic energy and the total electrostatic energy for the auroral curl simulation.....	130

- Figure 4.7 The spatially integrated velocity distribution functions for ions and electrons at time $\tau = 250\omega_{pe}^{-1}$132
- Figure 4.8 The spatially integrated velocity distribution function for ions and electrons at time $\tau = 5000\omega_{pe}^{-1}$133
- Figure 4.9 The position of the electron guiding centers at various times showing the formation of auroral curls...135
- Figure 4.10 The ion position at various times as they try to shield the electric field of the distorting electric sheet.....136
- Figure 4.11 Electrostatic potential contours for the auroral fold simulation at various times during the simulation.....138
- Figure 4.12 Spatially integrals velocity distribution functions for electrons and ions at time $\tau = 1000\omega_{pe}^{-1}$ for the auroral fold simulation.....140
- Figure 4.13 Spatially integrated velocity distribution functions of electrons and ions at time $\tau = 7000\omega_{pe}^{-1}$ for the auroral fold simulation.....141

Figure 4.14	(a)	Electron guiding centers at time $\tau = 1500\omega_{pe}^{-1}$143
	(b)	Electron guiding centers at time $\tau = 2000\omega_{pe}^{-1}$144
	(c)	Electron guiding centers at time $\tau = 2500\omega_{pe}^{-1}$145
	(d)	Ion positions at time $\tau = 1500\omega_{pe}^{-1}$146
	(e)	Ion positions at time $\tau = 2000\omega_{pe}^{-1}$147
	(f)	Ion positions at time $\tau = 2500\omega_{pe}^{-1}$148
	(g)	Equipotential contours at time $\tau = 1500\omega_{pe}^{-1}$149
	(h)	Equipotential contours at time $\tau = 2000\omega_{pe}^{-1}$150
	(i)	Equipotential contours at time $\tau = 2500\omega_{pe}^{-1}$151

List of Tables

Table 1.1	Summary of Previous Double Layer Simulation Studies	23
Table 2.1	A Summary of the Particle Code Classification Scheme, based on the number of spatial dimensions and which fields are computed self-consistently	34

1.0 Introduction

One of the most challenging problems in cosmic electrodynamics is to understand the mechanism that accelerates the electrons which cause the polar aurora. Recent satellite observations have begun to reveal two intriguing features associated with thin, curtain-like auroral forms (auroral arcs) which appear along the auroral oval, surrounding the geomagnetic pole. The first is that an auroral arc is caused by a thin sheet of electrons streaming down along geomagnetic field lines and these electrons carry a significant amount of field-aligned (upward directed) current (Cloutier et al., 1970, 1973; Arnoldy, 1974; Arnoldy et al., 1974; Anderson and Vondrak, 1975). The second feature is an indication that the sheet current is associated with a V-shaped potential structure in which a potential difference on the order of 5 kilovolts is present along the geomagnetic field lines above the auroral ionosphere at an altitude of 10,000 km (Gurnett, 1972, 1978; Gurnett and Frank, 1977; Møzer et al., 1977). Further evidence for the presence of a thin electron sheet is provided by TV-visual observations of small scale auroral deformations which appear to be the result of an electron sheet undergoing distortion caused by velocity shear (Hallinan and Davis, 1970; Hallinan, 1970). This thesis is a plasma simulation study of the interaction of a thin electron current sheet shielded by ambient ions with a conducting (ionospheric boundary). On the basis of this simulation study, a physical picture has emerged in an attempt to

explain the above observations. This thesis is the first time-dependent two-dimensional study of auroral arc formation. The acceleration mechanism is not prescribed but allowed to evolve self-consistently, and then identified as an auroral double layer.

The simulation demonstrates that the thin electron sheet is able to be deformed into the small scale auroral forms known as curls and folds. The relationship between curls and folds has not been previously understood, and this study demonstrates that the confusion was due to the fact that previous studies have not examined the role of the ambient ions, which try to shield the electric field of the electrons. The current sheet is shown schematically in Figure 1.1. The plane parallel to the ionosphere contains the sheet deformations, while the plane intersecting the ionosphere contains the accelerating V-potential structure. In this introduction, the morphology of auroral arcs is reviewed, including the elementary physics of the interaction between the precipitating electrons and the upper ionosphere. Then the theoretical models of auroral arc formation are reviewed.

1.1 The Morphology of Auroral Arcs

Energetic particle precipitation, comprised primarily of electrons and protons, is observed across the polar cap regions of the earth's ionosphere. This precipitation can be measured directly by polar-orbiting satellites, or by rocket-launched and balloon-borne detectors. The impact of this precipitation with the outer ionosphere initiates a complex process leading to the production of optical

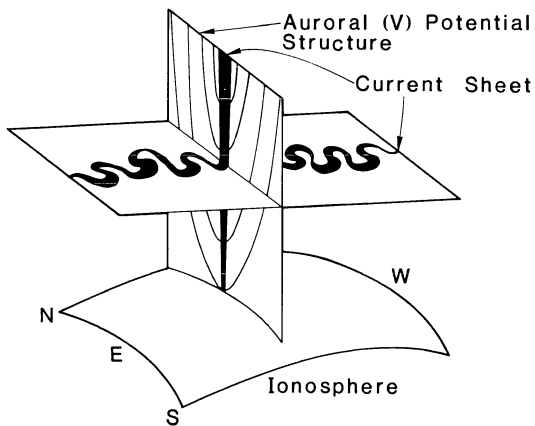


Figure 1.1 The two principal planes containing the auroral electron current sheet. One plane contains the V-shaped potential structure and the other contains the small scale deformations known as curls or folds.

radiation (and other effects) which can be visually observed on the ground (when it is intense enough and in the visible spectrum). The physics of the auroral particle interaction with the ionosphere will be reviewed in the next section. In this section the spatial distribution of the electron precipitation across the polar caps, in particular, the distribution of visual aurora, and the subject of auroral morphology, will be discussed.

The characteristics of the precipitation are complicated functions of latitude, local time, and magnetospheric activity (see Akasofu (1976), (1977) and Davis (1978)). Hence, the aurora is visually observed from the ground, is also complex in form and motion. Historically, the early studies of the aurora concentrated on identifying the regions and frequency of auroral occurrence. The region from 60° to 75° in latitude has been defined in the International Auroral Atlas (1963) as the 'auroral zone.' The term 'auroral zone' was used as the time-averaged locus of points on the earth's surface with a high-incidence of aurora. More recently, after extensive analysis of all-sky camera pictures taken during the IGY (1957-58) by Feldstein (1963), Akasofu (1977), and others, the 'auroral oval' was identified as a more important concept, being the instantaneous region of auroral occurrence. The oval is a narrow, eccentric belt encircling the magnetic dipole pole. The center of the oval is displaced about 3° toward the dark hemisphere, fixed with respect to the sun. The earth rotates under the oval once a day. The polar regions which sweep under the oval make up the previously mentioned 'auroral zone', which is the

locus of the midnight part of the oval on the earth's surface. The geometry of the auroral oval is closely related to the structure of the magnetosphere. The eccentricity of the oval is a result of the day-night asymmetry of the magnetosphere. The equatorward edge of the oval projected along the earth's magnetic field lines marks the outer boundary of the outer radiation belt. The magnetic field lines emanating from the interior of the oval traverse the outer magnetosphere. It is generally believed that the polar cap field lines leaving the inside of the inner edge of the oval are connected to the interplanetary field lines.

Because the field lines equatorward, inside, and poleward of the oval connect to different source regions of magnetospheric plasma, the characteristics of the precipitating particles also vary with respect to the different regions. As a result, the aurora observed in these three regions have unique characteristics as well.

Recent progress using montage photographs from the DMSP satellites (Akasofu, 1976) shows that there are basically two general types of aurora occurring in the three regions delineated by the oval. The two types of aurora are known as the 'discrete' and 'diffuse' aurora. The discrete aurora is a thin, curtain-like structure a few kilometers in width. The discrete aurora often appears as a single arc, or multiple parallel arcs separated by dark sky. The spacing of parallel arcs is of the order of a few tens of kilometers. The discrete aurora is predominantly an evening feature, lying in the region of the instantaneous auroral oval. Discrete auroras occur less frequently on

the interior of the oval, in which case they are known as polar cap auroras. They differ from the discrete arcs in the oval which are usually oriented along an east-west direction, in that polar cap auroras are oriented roughly along the sun-earth line. During quiet periods polar cap discrete auroras align themselves along the noon-midnight meridian, bending toward the evening sector, and ultimately lying parallel to arcs in the evening part of the oval. During the recovery phase of substorms the polar cap aurora can occupy the entire morning half of the polar cap.

In addition, discrete auroras are observed in the midday segment of the auroral oval. Midday auroras tend to fragment and to align radially toward the midday point of the poleward boundary of the oval.

The second type of aurora, the diffuse aurora, is a broad band of luminosity hundreds of kilometers in width. In many cases, it covers most of the sky for a single observer on the ground, and as a result cannot be easily resolved by all-sky cameras, although it is easily seen in recent satellite photographs. In some cases, the diffuse aurora may be many multiple, closely spaced, discrete arcs, making the difference between discrete and diffuse aurora rather arbitrary. The diffuse aurora often occupies the equatorial half of the auroral oval, especially in the evening sector. In addition, the diffuse aurora often occupies an annular belt equatorward of the oval, centered on the dipole axis. The annular belt intersects the oval in the midnight sector. The poleward boundary of the diffuse aurora often forms wavy structures

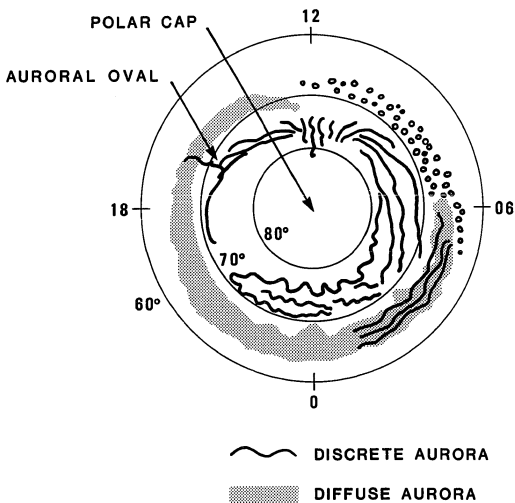


Figure 1.2 Diagram showing distribution of electron precipitation across polar cap with the resulting displays of discrete and diffuse auroras.

shaped like an inverted Ω (omega) and are called omega bands. Omega bands drift eastward. The poleward boundary also shows large torch-like structures during intense substorms. They drift westward. A summary of the distribution of discrete and diffuse auroras across the polar region is given in Figure 1.2.

Discrete auroras, when viewed from a point of the earth's surface, take on a variety of forms. The quietest and most simple form is the homogeneous arc. During times of slightly more activity, the arc develops a series of fine curls, folds or ripples. These ripples, are believed to be a result of shear flow in the current sheet, and will be discussed more later. During very active times the arc may develop larger folds, superimposed on the small scale folds. These large scale deformations are known as Rayed Bands, and if the large scale folds 'wind up' they are known as folded ribbons and spirals. These small scale curls and folds and large scale spirals have been described by Hallinan and Davis (1970), and are found to be essential elements in the plasma simulation results of Chapter 4 of this thesis.

1.2 The Optical Aurora

The precipitation pattern of electrons into the polar ionosphere and the resulting diversity of auroral occurrences with the associated auroral forms has been discussed. Now, it is appropriate to mention the physics of the electron-ionosphere interaction. A schematic diagram of processes leading to the production of the optical aurora is shown in

Figure 1.3, which is a slightly simplified version found in the work of Rees (1975).

The process begins with earthward plasma flow, initiated by various mechanisms depending upon the source of the plasma. It may be directly from the solar wind in the case of polar cap and cusp auroras, or from deep within the magnetospheric tail (beyond $10 R_E$) for discrete and diffuse auroras in the auroral oval. The plasma interacts with the ionosphere in a complicated process beginning with the formation of the auroral double layer acceleration mechanism, where the plasma sheet electrons are energized into the Kev energy range. These accelerated electrons are known as primary auroral electrons in order to be distinguishable from the other electron populations found in the region. These other populations include collisionally backscattered and degraded primaries, secondary electrons created during the collision process between the accelerated primaries and the ionospheric constituents, in addition to electrons trapped between the magnetic mirror and the accelerating region, and cold background electrons. The incident electrons can interact with the ionosphere in four principal ways. Some of the electrons collide, are decelerated (Bremsstrahlung) and emit x-rays. Some of the primary electrons collide and ionize the ionospheric neutrals releasing secondary electrons in the process. The primaries can also dissociate molecular neutrals and ions producing excited atoms and molecules. Finally, the primaries can directly excite through collisions the constituent atoms, molecules and ions of the upper ionosphere. The secondary electrons in turn can recombine with

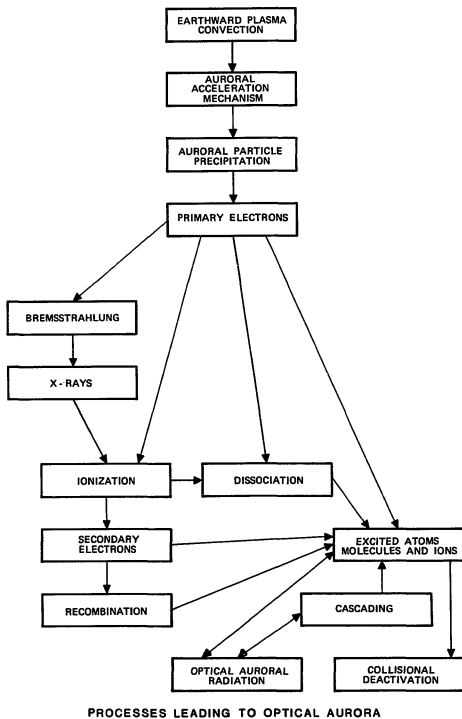
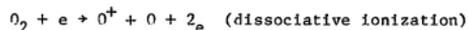
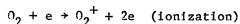
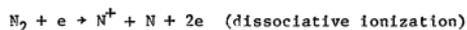
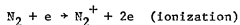


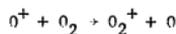
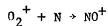
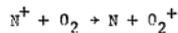
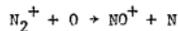
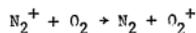
Figure 1.3 Schematic processes leading to the optical aurora.

the available ions or collide with the constituents producing more excited particles. These particles in the excited state can optically radiate producing the visual aurora, or can be collisionally deactivated. When the radiation occurs between successive excited states rather than directly to the ground state, the process is known as cascading, and is an important source of particles in excited states not created by collisions.

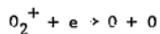
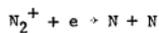
The major atmospheric constituents at auroral heights are molecular and atomic oxygen and nitrogen. Therefore, the principal reactions between the incident primaries and the major ionospheric neutrals are:



The collisional products may be in excited states, and the resulting ion chemistry can be quite complicated. The intermediate reactions which proceed after the primary reactions are:

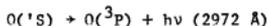
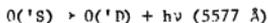


The production of secondary electrons requires a loss process where the electrons recombine with the ions, and the most important are:





Some of the most important optical transitions are found in the excited states of atomic oxygen, particularly the so called forbidden transitions which produce the common green 5577 Å color and the high altitude dark red 6300 Å. The initial transitions proceed as (given in Omholt (1971)).



or



To actually understand the electron-ionosphere interaction, and be able to compute the emission rate of any transition as a function of height in the auroral ionosphere requires a detailed knowledge of the atmosphere-ionosphere chemistry as a function of height, and a detailed knowledge of the primary electron's flux, energy, and pitch angle distribution. As the primary electrons collide with the ionosphere they deposit their energy into the ionosphere and some of this energy will be

observed as optical radiation. Very sophisticated models for computing this energy deposition are available, such as Stannnes' (1980) technique which solves the transport equation for electrons through a plane-parallel atmosphere using multiple streams to approximate the components of the primary auroral electron energy and pitch angle spectrum. The excitation rate $\eta(h)$ for any given state as a function of height can be calculated from (Rees, 1978, University of Alaska course in Auroral Physics, and Vallance Jones, (1974)).

$$\eta(h) = n(h) \int_{E_{th}}^{\infty} (\phi_S(E, h) + \phi_P(E, h)) \sigma(E) dE, \quad (1.1)$$

where $\phi_S(E, h)$ and $\phi_P(E, h)$ are the secondary and primary electron fluxes as functions of energy and altitude E_{th} is the threshold energy. $\sigma(E)$ is the collisional cross-section (in cm^2) for the given transition as a function of energy and excitation source mechanism. The emission rate can be computed by summing over all the excitation rates for the given transition, and accounting for any loss or quenching processes which deactivate the excited state before it can radiate.

Height profiles of optical emissions require considerable knowledge of the energy deposition rate as a function of height for the primary electrons, the production rate of secondary electrons, and details of the constituent chemistry including collisional cross sections, and transition probabilities.

1.3 Auroral Acceleration Mechanism

The subject of the primary auroral acceleration mechanism is still in a controversial state. For many years it was thought that no magnetic field-aligned electric fields, also called "parallel" electric fields, could exist in the magnetosphere because the supposedly infinite conductivity of the magnetospheric plasma could easily short out the potential drop, thus preventing its development. The first suggestion that field-aligned electric fields might play an important role in magnetospheric processes was by Alfvén (1958), but it went unheeded for many years until observational measurements demonstrated their existence. The first measurements of field-aligned electric fields above the ionosphere at distances from one to ten earth radii have been made by rocket-borne detectors, barium injections and satellite measurements. These measurements have shown that auroral arcs are associated with potential structures having electric fields both parallel and perpendicular to the geomagnetic field. The electric potential contours of these electric fields are shaped like the letter V, and they are referred to as V-shaped potential structures.

Values for the electric field perpendicular to the magnetic field of over 150 mV/m and values up to 30 mV/m parallel to the magnetic field have been measured, and are discussed in the reviews, by Cattell et al. (1979) and Mozer et al. (1976). The very recent results of Mozer et al. (1977) show the existence of very strong parallel and perpendicular fields, up to 800 mV/m for altitudes of 2000-8000 km. In their results they reported several pairs of oppositely directed electric fields

having strengths 400-800 mV/m and having a spatial separation of around 30 km, associated with a parallel electric field of 200-800 mV/m.

Barium injection experiments by Wescott et al. (1976) found a 40 mV/m electric field perpendicular to the magnetic field at altitudes above 5500 km. Haerendel et al. (1976) found barium ions to accelerate up the magnetic field lines to energies near 200 eV in the presence of red aurora at an altitude of 2500 km. They found the ions to be accelerated to almost 7 keV at 7500 km in the presence of a green arc.

The association of auroral arcs with field-aligned currents was shown by Arnoldy (1974) and Arnoldy et al. (1974) using auroral sounding rockets. Similar measurements were made by Cloutier et al. (1970, 1973), with field-aligned current up to 10^{-6} A/m^2 being measured. Recent current density measurements by Anderson and Vondrak (1975) show the field-aligned current to be as high as 10^{-5} A/m^2 in bright discrete auroras, decreasing to 10^{-6} A/m^2 under quiet conditions (Iijima and Potemra, 1978).

It was pointed out by Kan et al., (1979) that large scale inverted-V type (the electron precipitation energy flux has the shape of an inverted letter V) precipitation reported by Frank and Ackerson (1971) in which the electrons are found with energy peaks in the keV range (suggesting field-aligned potential drops), should not be confused with the precipitation producing the small scale auroral arcs. The latitudinal width of the inverted-V type precipitation is typically around 50 km (Lin and Hoffman, 1979), much larger than the width of an auroral arc which is around 100 meters (Hallinan and Davis, 1970). Kan et al.

(1979) concur with Meng (1978) suggesting that auroral arcs are very small scale V-shaped structures, imbedded in the large scale inverted-V precipitation.

Together, these observations point to the presence of field-aligned potential drops, as originally suggested by Gurnett (1972). The physical mechanism which produces and sustains the observed potential drop is not well understood. Double layers, shocks, anomalous resistivity, pitch angle anisotropy, the thermoelectric effect, and Alfvén waves have all been proposed as possible mechanisms that could explain the measurements. The most up-to-date summary of the role of these mechanisms can be found in Kan and Lee (1981). Any plasma process proposed to explain the observations must include both parallel and perpendicular electric field components, sustained by at least six species of different constituent particles (Meng, 1978; Hultqvist 1972, 1979) including precipitating magnetospheric electrons, background magnetospheric ions, upstreaming ionospheric ions, ionospheric electrons, electrons trapped between the accelerating region and the magnetic mirror, and backscattered primary and secondary electrons produced by collisions in the ionosphere. The thickness of the thin auroral arc is on the order of the Debye length (Kan, 1975) and is less than the average ion gyroradius, $\lambda_{De} \lesssim \text{sheet thickness} < \rho_i$. For the larger-scale inverted-V type precipitation $\lambda_{De} < \rho_i < \text{sheet thickness}$. This thesis concentrates on the thin auroral arc only because the thicker inverted-V type precipitation requires a large scale model which exceeds our current computer capabilities.

1.3.1 Double Layers

Double layers were originally observed by Langmuir (1929), while he was studying the phenomena of sheaths occurring in vacuum tubes. He was particularly interested in the double sheaths which formed around flat hot cathodes and anodes, and measured excess negative charge around the cathode and excess positive charge around the anode. He found the electric potential was nearly constant between the concentrations of charge, and was located in the regions between the conductors. He called this phenomena a double layer.

Since Langmuir's work, numerous laboratory experiments have verified the existence of laboratory double layers, including Torvén and Babic (1975), Quon and Wong (1976), Levine et al. (1978, 1980), Coakeley and Hershkowitz (1979), Iizuka and Potemra (1979), Baker et al. (1980) and Stenzel et al. (1980). Torvén used a device to produce a perturbation leading to unstable but periodic double layer formation. Anderson et al. (1969) was the first to measure the velocity distributions of electrons on both sides of the double layer and noticed the accelerated electron thermalized quickly after passing through the double layer. High number densities ($n \sim 10^{11} \text{cm}^{-3}$) and short Debye lengths, $\lambda_{De} \sim .05$ cm prevented detailed analysis of double layer formation. Quon and Wong achieved what they called 'weak' double layer formation for a slightly less dense ($n \sim 10^8 \text{cm}^{-3}$) and longer Debye lengths $\lambda_{De} \sim 2$ cm.

They found their double layer to be unstable when the electron drift speed was more than three times the electron thermal velocity.

Coakely et al. (1979) were the first to establish the laboratory existence of strong double layers using the triple plasma device at the University of Iowa. They did not find the resultant electron beam to be thermalized unlike in the previous experiments. The double layer thickness in their experiments was around $200 \lambda_{De}$. Laboratory devices inspired by magnetospheric conditions include Baker et al. (1980) and Stenzel et al. (1980), whose two-dimensional double layers show the V-shaped potential expected.

Theoretical work on double layers began with Langmuir's (1929) work, followed by Block (1972), Knorr and Goertz (1974), Kan (1975), and Levine and Crawford (1980). These works were primarily concerned with conditions for double layers in one-dimension. Recently the double layer theory has been extended to two-dimensions using auroral boundary conditions and particle populations by Kan and Lee (1979), and they pointed out that the presence of electrons trapped between the dipole mirror and the accelerating region reduced the double layer criterion given by Block on the minimum required streaming speed for the electrons. Block (1972) showed that the pre-acceleration energies must be greater than the sum of the electron and ion thermal energies,

$$\begin{aligned}
 mv_D^2(L) &> \gamma v_{th}(L) + v_{th}(L) \\
 & \\
 MV_D^2(0) &> \gamma v_{th}(0) + v_{th}(0)
 \end{aligned}
 \tag{1.2}$$

where $v_D(x)$ is the electron drift velocity as function of distance through the double layer, and $V_D(x)$ is the ion drift velocity as a function of distance through the double layer. M and m are the ion and electron mass respectively, and γ is the specific heat ratio. When applied to the auroral double layer, $v_{th}(0)$ is the thermal velocity at the ionosphere while $v_{th}(L)$ is the thermal velocity at some height L , above the double layer, in contact with the hot plasma sheet or magnetospheric plasma. Kan and Lee (1980a, 1980b) on the other hand showed that if $v_D(L) > 0$, the Block criterion is relaxed provided that population of trapped electrons exists below the double layer, and this population has a density greater than a critical density given by

$$n_c = n(L) \frac{e\phi}{\frac{1}{2} m [v_d(L) + v_{th}(L)]^2} \quad (1.3)$$

where n_c is the critical number density of the trapped electrons, n (< 1) is the number density of the electrons at the plasma sheet boundary, and ϕ is the double layer potential.

It should be noted that all of the double layer theories presented so far have been steady state (not time dependent) solutions of Poisson's equation and have supplied some conditions on the particle populations producing the double layer. To understand the time development of double layers it is necessary to use computer simulation because of the complexity of the problem.

Particle simulations of double layer formation in one dimension (1-D simulations) have been performed by Goertz and Joyce (1975), Degroot

et al. (1977), Joyce and Hubbard (1978), Hubbard and Joyce (1979), Singh (1980), Singh and Thiemann (1980), and Sato and Okuda (1980). A two-dimensional double-layer simulation is part of this thesis, and is an extension of Wagner et al. (1980). In the 1-D simulation of Goertz and Joyce, various electron drift velocities from $V_D = 0.5$ to 1.5 ($T_e = T_i$) and system lengths from 37 to $100 \lambda_{De}$ were used. They concluded that double layers formed whenever the electron drift velocity exceeded the thermal velocity. The boundary condition they used was zero potential at one boundary and vanishing electric field at the other. In the 1-D simulation of Joyce and Hubbard (1979), a potential was applied across the system, made up of a Maxwellian plasma, $T_e = T_i$. They mentioned without comment that if $T_e < \frac{1}{2} T_i$ no double layer formed. They applied potentials from $10 - 200(T_e)$ over systems 31 to 360 Debye lengths long, and found stable double layers for most cases except when the ion-ion two stream instability occurred disrupting the double layer.

Degroot et al. (1977) used 1-D and 2-D periodic cloud-in-cell codes to study anomalous resistivity and found that when an initial perturbation was present, a localized potential drop would form in the form of a double layer. The results are unusual because of the use of a cooling algorithm on the electrons to prevent heating, and the use of high electron drift velocities $v_d > v_{th}$, and hot electron $T_e \gg T_i$, do not apply to auroral conditions.

A unique simulation has been carried out by Singh and Thiemann (in press), which is carried out by solving the one-dimensional Vlasov and Poisson equations as an initial-boundary value problem. They fix the

potential drop across the system, of around 15 times the electron thermal energy. An unusually high electron drift velocity $v_d = 2 v_{th}$ was used. They found a double layer formed, apparently triggered by strong electron-ion and electron-electron two stream turbulence.

Recently, a one-dimensional, finite-size particle simulation using periodic boundary conditions was carried out by Sato and Okuda (1980). Although this assumption of $T_e \gg T_i$ may not apply to auroral plasma, their results are special because of their use of very long systems ($> 1000 \lambda_{De}$). They found that many localized double layers would turn to limit the electron drift velocity $v_d \ll v_{th}$ and heat the electrons. The double layer did not form when the initial electron temperature was made smaller, however. A summary of the simulation studies can be found in Table 1.1.

1.3.2 Electrostatic Shocks

Electrostatic shocks are potential structures which form in current-free plasmas. Considerable confusion has occurred in the space physics community, because of the misuse of the term 'shock' by Kan (1975), Swift (1975), Mozer et al. (1977) and Hudson and Mozer (1978). The term double layer should have been used because the potential structures under study were current carrying. In the case of electrostatic shocks, the plasma flows through the shock potential and the ions slow down, decelerated by the potential, while the electrons are accelerated. The energy source of the electrons is the loss of energy by the ions. Shocks have been studied by Moiseev and Sagdeev

Summary of Double Layer Simulations

Table 1.1 Summary of Previous Double Layer Simulation Studies.

Study	Code	Boundary Conditions	Comments
Goertz and Joyce 1975	1-D particle in cell	bounded $\phi = 0$ at $x = 0$ $E = 0$ at $x = L$	$.5 < v_d < 1.5$ $T_e = T_i$ unstable double layer
Degroot et al. 1977	1-D cloud in cell 2-D cloud in cell	periodic periodic	$v_d > 1$ $T_e > T_i$ requires initial perturbations $v_d > 1$ $T_e > T_i$ and unusual cooling algorithm
Joyce and Hubbard 1978	1-D particle in cell	bounded $\phi = 0$ at $x = 0$ $\phi = \phi_0$ at $x = L$	$v_d = 0$ $T_e = T_i$ periodic double layer formation
Singh and Thiemann in press 1980	1-D initial value problem	bounded $\phi = 0$ at $x = 0$ $\phi = \phi_0$ at $x = L$	$v_d = 2 v_{th}$
Sato and Okuda 1980	1-D finite size particle	periodic	$v_d < v_{th}$ but $T_e \gg T_i$ multiple localized double layers appear periodically
Wagner et al. 1980	$2\frac{1}{2}$ -D finite size particle	ionospheric boundary converging dipole magnetic field	$v_d \lesssim v_{th}$ $T_e \ll T_i$ stable V-shaped double layer with auroral boundary conditions

(1963), Montgomery and Joyce (1969), and Sakanaka et al. (1971). Plasma simulation studies of shocks include Mason (1972), and Forslund and Shonk (1971).

As Kan and Lee (1981) point out, since the flux of electrons and ions are conserved on both sides of the shock, if the shock were to be the principal acceleration mechanism, then equal fluxes of both would be observed impacting the ionosphere. Observations clearly show auroral arcs are caused by a precipitating electron flux which is always greater than the ion flux. It is wrong to say that the shock process does not occur however, because when the accelerating potential is less than the plasma sheet ion energy, some of the ions can reach the ionosphere, giving their energy to the accelerating potential. When the accelerating potential is greater than or equal to the plasma sheet ion kinetic energy, the ions cannot reach the ionosphere and are trapped above the accelerating region. In this case, the shock process does not occur, and the acceleration process is a double layer.

1.3.3 Differential Pitch Angle Anisotropy

Alfvén and Fälthammar (1963) suggested that parallel electric fields could result from pitch angle anisotropy between electrons and ions. This is because anisotropic pitch angle distribution functions of electrons and ions would cause them to mirror at different heights, and a field-aligned electric field would result. The magnitude of the electric field would be strongly dependent upon the relative pitch angles and energies of the particles. The mechanism has been refined in

the zero current limit by Persson (1963, 1966), Whipple (1976), Ponyovin et al. (1977) and Fridman and Lemaire (1980). Ponyovin showed that the maximum potential difference generated by this process is limited by the thermal energy of either the electron or the ions, whichever is smaller. Earlier work by Knight (1973) had shown that in the presence of field-aligned currents this mechanism could give rise to potential drops of several kilovolts, provided the voltage drop was over very long distances. Pålthammar (1977) shows that the maximum sustainable potential drop of about 15 mV/m, compared to measured values of 800 mV/m. Hence, the mirror force alone is not capable of sustaining the large observed potential drop. Nonetheless, this mechanism may add to total potential drop, and it almost certainly plays a crucial role in supplying the trapped electron population necessary for a stable double layer, as shown by Kan and Lee (1980).

1.3.4. Anomalous Resistivity

A current driven through a resistor results in a voltage drop across the resistor according to Ohm's Law. This simple concept combined with observations of field-aligned currents associated with auroral arcs has led to a search for a mechanism to produce anomalous resistivity in the collisionless plasma through which the auroral current flows. An up to date review on this subject can be found in Papadopolous (1977) with much of the early work found in Kindel and Kennel (1971). Numerous proposals for the anomalous resistivity mechanism (Ionson et al., 1976; Hudson et al., 1978; and Cattell et al.

1979) have been made, but the ability of plasma to sustain the required current-driven instability in the nonlinear regime remains controversial (Shawhan et al., 1978; Fälthammar, 1977). From a theoretical point of view, electrostatic ion cyclotron turbulence is the most likely candidate for producing anomalous resistivity in the auroral resistivity region, because it has the lowest current threshold of any of the likely possibilities. Recent plasma simulations by Okuda et al. (1981) have shown that ion cyclotron waves may have much lower saturation levels than previously expected, leaving other mechanisms such as the electron-ion Buneman instability (Buneman, 1959), and the ion acoustic instabilities worth re-examining.

Studies of ion acoustic waves have shown that ion acoustic waves should be excited when the electron drift velocity exceeds the ion sound speed, but the growth rate is strongly dependent on the T_e/T_i temperature ratio. The fact that ion acoustic waves are not unstable for $T_e/T_i \lesssim 1$ makes them an unlikely candidate in auroral processes.

Fälthammar (1978) and Shawhan et al. (1978) show that the required a.c. electric fields caused by anomalous resistivity must be much greater than observed, and therefore, is unlikely to be the primary source of the field-aligned potential. Nonetheless, it may play important roles in causing localized disturbances such as local current interruption, pulsations, and may be responsible for filamentation of electron precipitation into thin sheets having widths on the order of the ion gyroradius (Kan and Lee, 1981; and Bohmer and Fornaca, 1979).

1.3.5 Thermoelectric Effect

Hultqvist (1972, 1979) has proposed a mechanism based on the thermoelectric effect. He suggests that when hot plasma coming from the earth's plasma sheet comes in contrast with cool ionospheric plasma, an electric field will be set up along the contact boundary. The mechanism does not require an electrical current. Unfortunately, the high mobility of the electrons implies that the electric field will be in the opposite direction of the auroral accelerator, and is limited in strength by the electron thermal energy. For these reasons this mechanism is unlikely to play an important role in the auroral acceleration process.

1.3.6 Alfvén Waves

It has been suggested by Fejer and Kan (1969), Boström (1974), Hasegawa (1976), and Goertz and Bosewell (1980), that parallel electric fields could be generated by the propagation of oblique Alfvén waves, generated by magnetospheric convections and imperfect magnetosphere-ionosphere coupling. A recent review of this work can be found in Chiu et al. (1980) and Kan and Lee (1981).

2.0 Plasma Simulation Techniques Applied to Space Physics

Numerical simulation techniques have rapidly expanded in scope and realism during the last few years, largely due to needs of the fusion plasma physics community. This increase in capability has come about for two reasons, the first being improvements in mathematical techniques, and the second being rapid advances in computer speed and memory size. Despite the fact that plasma computer simulation now plays an essential role in fusion physics by reducing the need for experiments (which are prohibitively expensive) to test theoretical models, the use of simulation in space physics is in its infancy. The realization that these powerful tools existed, but were not fully recognized until recently, provided the motivation in this thesis to extend their usefulness on a challenging space physics problem.

There is a tremendous disparity between the plasma processes studied in laboratory machines and the plasma which make up the solar and terrestrial magnetospheres. Despite major differences in scale sizes and process times it is possible to study all of these processes with modern simulation techniques. The relationship of space plasmas to laboratory plasmas can be seen in Figure 2.1.

Plasma simulation has taken two directions, one being the fluid technique and the other being the particle approach. Fluid simulation of plasmas use the MHD approximation and are useful for problems having very large spatial scales, and requiring very long process times. Fluid

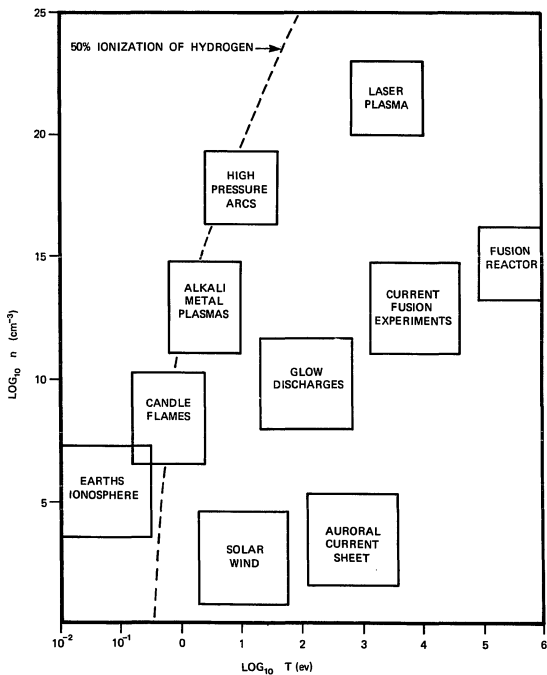


Figure 2.1 Schematic diagram showing parameter regimes of space, ionospheric, and laboratory plasmas.

techniques solve for the density, velocity, and the self-consistent magnetic field and other quantities, using the MHD equations on a computational grid. The fluid approach fails whenever the MHD approximation breaks down, which unfortunately is the case in many space physics problems. Whenever there is a field-aligned potential drop, or whenever spatial and temporal scales are on the order of the gyroradius and gyrofrequency, respectively, the fluid approach fails. For example, these criteria are violated at the bow shock, magnetopause, plasma sheet, cusp, and the auroral acceleration region. In these regions the second technique, particle simulation, must be used.

In particle simulation, the simultaneous motion of many electrons and ions are followed in both self-consistent and applied electric and magnetic fields. Unfortunately, a major approximation is required because of computer limitations. The 10^4 to 10^6 computer particles must represent 10^{23} or more particles in the real plasma. For this reason the "computer particle" must represent many real particles and must be considered to be a cloud or sphere of plasma particles. Whereas the real particle has a mass m_e or m_i (electron or ion, respectively), the computer particle, or macro-particle, will have a much larger mass M_e and M_i . Where the real plasma has 10^4 to 10^8 particles in a Debye sphere, the computer plasma will have around 10^2 to 10^3 particles.

A second approximation is needed when the force acting on each macro-particle is computed. It is not feasible to sum over all particles to find the net force on each one, because the computer is too slow to compute the net force this way in a reasonable time.

Furthermore, studies have shown that this method over-emphasizes close binary collisions which are artificial when macro-particles are used. In a real plasma a binary collision is between just two particles. In a computer plasma each particle is made up of thousands of real particles and a single binary collision of the macro-particles represents the rare close collision of all these real particles together, which is an unrealistic event. The calculation is greatly simplified, and artificial collisions and noise due to the macro-particle assumption are greatly reduced, when an electric field approach is used to find the force on a particle. This electric field is calculated from the density of the other charges through Poisson's equation, rather than summing over the contribution from each of the particles. This field approach makes it possible to incorporate conducting or dielectric boundaries, and allows the examination of a small portion of an infinite plasma when periodic boundary conditions are used.

The basic structure of a plasma simulation code is shown in Figure 2.2. The particle's initial conditions are specified by choosing the particle's position $x(i)$, and velocities $v_x(i)$ for each i 'th particle (for a one-dimensional simulation). In two dimensions $x(i)$, $y(i)$, $v_x(i)$, and $v_y(i)$ must be chosen. Particle codes are classified in two ways, according to how many physical dimensions are used, and according to what fields are computed self-consistently. A 2-D electrostatic code computes a self-consistent electric field in a plane. A $2\frac{1}{2}$ -D magneto-static code computes self-consistent electric and magnetic fields in two dimensions, and retains a third velocity coordinate to allow for gyro-

Particle Simulation Code Structure

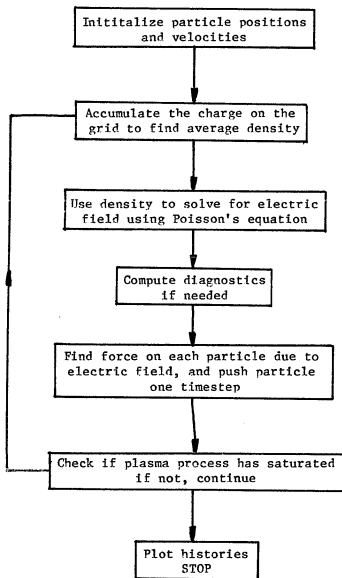


Figure 2.2 Basic structure of an electrostatic simulation code using finite size particles.

motion in and out of the simulation plane. The classification scheme is shown in Table 2.2

2.1 Historical Background for Particle Simulation

The first attempts to model nonlinear plasma behavior began with the early "sheet" models, which were one-dimensional, by Dawson (1959, 1960, 1962), and Eldridge (1962). These early codes modeled an infinite plasma in one dimension by assuming the plasma was made up of infinite charge sheets that interacted through the Coulomb force only. Mechanical collisions were ignored. One of the major problems encountered in these early attempts was that binary collisions and close particle encounters had an exaggerated effect that masked the long range Coulomb effects. These spurious effects were due to too few particles moving within a Debye length. An approach was developed to overcome this difficulty by modifying the force law between particles to reduce the Coulomb force in close particle encounters while leaving the long effects intact. This approach smoothes the fields due to individual particles over a grid. Hockney (1966) was the first to use a spatial grid in a fashion that is now known as the NGP technique, where the particle's charge is assigned to the nearest grid point (hence NGP), and then Hockney solved Poisson's equation on the grid using a finite difference technique rather than summing the contribution of each particle's electric field on every other particle. Although the finite difference technique is rarely used in simulations today, the NGP method of assigning particle quantities to grid locations is in widespread use

PARTICLE CODE CLASSIFICATION SCHEME

Table 2.1 A Summary of the Particle Code Classification Scheme, based on the number of spatial dimensions and which fields are computed self-consistently.

Dimensions
1D - x 1 $1/2$ D - x, v_x, v_y 1 $2/2$ D - x, v_x, v_y, v_z 2D - x, y, v_x, v_y 2 $1/2$ D - x, y, v_x, v_y, v_z 3D - x, y, z, v_x, v_y, v_z
Self Consistent Fields
Electrostatic - \vec{E} applied \vec{B} Magnetostatic - \vec{E}, \vec{B} no radiation Electromagnetic - E, B with radiation

in one-dimensional simulations. The use of the grid implied that there would be no collisional interaction between particles that were located less than the grid mesh size apart. The need to extend the simulation to higher dimensions led Birdsall and Fuss (1969) to the cloud in cell technique of smearing the particle charge over a two-dimensional grid, a method that has been replaced by the subtracted dipole (SUD).

The use of fast fourier transforms (FFT) by Dawson et al. (1969) allowed two major improvements in improving accuracy while reducing unnatural collisions. The FFT approach improved the accuracy of the Poisson solution by eliminating numerical problems with finite differencing. Furthermore, the FFT allowed the natural suppression of noise with wave-lengths less than the grid size.

Most recently, Langdon and Birdsall (1970), Dawson (1970) and Okuda and Birdsall (1970) introduced the concept of finite size particles to plasma simulations. The finite size particle technique assumes the plasma is made up of gaussian shaped finite sized clouds of charge, and has been put on a firm theoretical basis by Okuda and others. Using finite sized particles to model the plasma is physically meaningful, easy to understand, and accomplishes the goal of reducing collisional noise because the Coulomb force between finite size particles goes to zero as they penetrate one another. The demonstration that a finite sized particle plasma exhibits the physics of a real plasma has been given by Okuda (1972), Matsuda (1975), and many others. It is the standard technique today.

The use of a computational grid can introduce nonphysical effects under certain circumstances. These effects are largely due to aliasing, where the inter-grid distance is too large to examine the small-scale phenomena under study. These effects have been shown by Langdon and Birdsall (1970) and Okuda (1972) to be avoidable by never asking the grid distance to describe effects longer than 1-2 Debye lengths.

The most recent innovations in particle simulation techniques are the extensions of the simulation codes to higher dimensions, to include self-consistent magnetic fields, and to include radiation effects. The magnetostatic particle codes are based on Darwin's (see Jackson, 1975) formulation of Maxwell's equations, and ignore the displacement currents and radiation effects. Some of the magnetostatic codes are one-dimensional, such as Hasegawa and Okuda (1968); Haber et al. (1970); Denavit (1974), but the most recent have been multi-dimensional such as Nielson and Lewis (1976) and Busnardo-Neto et al. (1976). Fully electromagnetic codes, which use the full set of Maxwell's equations and use fully relativistic particle dynamics are being developed by Lin et al. (1974).

All of the above codes have been periodic, that is the simulation assumed periodic boundary conditions, and are appropriate for work on infinite plasmas. Simulation codes not requiring periodic boundary conditions are a topic of current research. One center for this research is J.M. Dawson's group at UCLA. Reliable bounded (nonperiodic) codes are just now being published, such as Decyk's (1977, 1979) bounded electrostatic code which was developed for space physics application in

this thesis. Rounded magnetostatic (Lin et al., 1975) and electromagnetic (Tajima, 1980) are also being published.

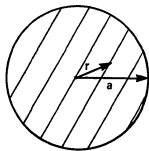
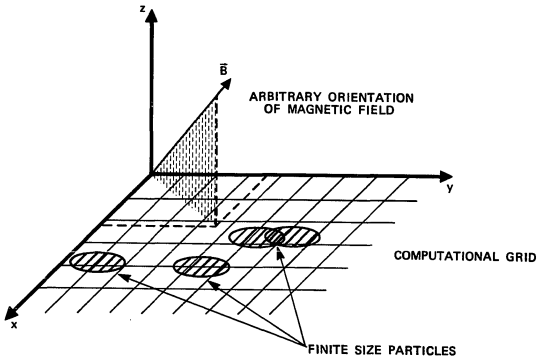
2.2 Finite Size Particles

In this section the theory for finite size particle (plasma clouds) is reviewed. The relationship between finite size particles and the computational grid is shown in Figure 2.3. To begin, let us assume that each particle in the simulation has a shape defined by a function called the shape factor, $S(r)$, which describes the distribution of charge as a function of radius for the particle. It has been shown that a Gaussian shape factor is the wisest choice when FFT techniques are going to be used to solve for the force on the particles using the computational grid. The Gaussian shape factor is defined as

$$S(r) = \frac{1}{\sqrt{2\pi}a} e^{-r^2/2a^2} . \quad (2.1)$$

The $1/\sqrt{2\pi}a$ factor is the normalization factor which guarantees that the total charge is 1. Equation 2.1 is shown schematically in Figure 2.3. It is possible to compute the electric force on finite sized particles having a shape factor by integrating over the charge distribution. If the particle is the i^{th} macro particle in the simulation, then the force on the i^{th} particle is just

$$\frac{dv_i}{dt} = \frac{q}{M} \int_0^L E(r) S(r - r_i) dr . \quad (2.2)$$



FINITE SIZE PARTICLE

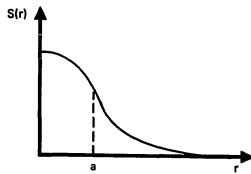
SHAPE FACTOR FOR
FINITE SIZE PARTICLE

Figure 2.3 An illustration of the relationship between the computational grid for the solution of Poisson's equation.

The integral in equation 2.2 is from 0 to L, the length of the computation grid. $E(r)$ is the electric field acting on the particle at a point r . The charge q and mass M represent the charge and mass of a plasma cloud and therefore must be equal to ne and nm_e (electrons) or nm_i (ions) where n is the number of particles in the cloud. The system length $L = N\Delta$ where N is the number of grids and Δ is the grid spacing. It is conventional to normalize the variables in the following way. The unit of length is specified to be grid spacing Δ . The unit of time is specified in terms of the inverse electron plasma frequency ω_{pe}^{-1} , defined as

$$\omega_{pe} = \left(\frac{4\pi ne^2}{m} \right)^{1/2} . \quad (2.3)$$

Then the dimensionless velocity is $v^* = v \left(\frac{1}{\omega_{pe} \Delta} \right)$, and the dimensionless time is $t^* = t \omega_{pe}$. Hence, the dimensionless force equation becomes, for the i^{th} particle

$$\frac{dv_i^*}{dt^*} = \frac{q}{m\omega_{pe}^2 \Delta} \int_0^L E(r) S(r - r_i) dr . \quad (2.4)$$

Now the major advantage of using this formulation for the force, including the Gaussian shape factor can be shown, by replacing $E(r)$ and $S(r - r_i)$ by their discrete Fourier expansions.

$$E(r) = \sum_{k_1} E(k_1) e^{ik_1 \cdot r} \quad (2.5)$$

$$S(r - r_i) = \sum_{k_2} S(k_2) e^{i k_2 (r - r_i)} \quad (2.6)$$

Substituting 2.5 and 2.6 into 2.4 yields an expression for the force on the i^{th} particle, after integration,

$$\frac{dv_i^*}{dt^*} = \frac{qL}{m\omega \frac{2}{pe}} \sum_{k_1} E(k_1) S(k_1) e^{i k_1 r} \quad (2.7)$$

An expression for $S(k_1)$ is derivable from the Gaussian definition,

$$S(k) = \frac{1}{L} e^{-k^2 a^2/2} \quad (2.8)$$

so that substituting 2.8 into 2.7 yields, and replacing k_1 , by just k ,

$$\frac{dv_i^*}{dt^*} = \frac{q}{m\omega \frac{2}{pe} \Delta} \sum_k E(k) e^{-k^2 a^2/2} e^{i k r} \quad (2.9)$$

but the expression on the right of 2.9 is identifiable as the inverse Fourier transform and can be written

$$\frac{dv_i^*}{dt^*} = \text{FFT}^{-1} F(k) \quad (2.10)$$

where

$$F(k) = \frac{e}{m\omega \frac{2}{pe} \Delta} e^{-k^2 a^2/2} E(k) \quad (2.11)$$

is the force on the particle in k-space. The quantity in front of the electric field in k-space is known as the form factor and is computed ahead of time and used whenever the force needs to be computed.

This section has developed the theory necessary to use finite size particles in a plasma simulation, in particular, how to compute the force on a Gaussian shaped particle given the electric field on a computational grid. The next section will describe how the electric field can be computed by solving Poisson equations for a bounded system.

2.3 The Solution to Poisson's Equation

As mentioned earlier, one of the most important aspects of a simulation code is its Poisson solver. The past decade of research has amply demonstrated that the fastest, most accurate, and generally most useful Poisson solver uses fast fourier transform (FFT) techniques. Periodic boundary conditions are easily handled because of the periodicity assumption in the formulation of the discrete fast fourier transform. In this thesis, a two-dimensional Poisson solver that removes the periodicity conditions is required. Poisson's equation must be solved assuming the charge distribution is given on a two-dimensional computational mesh. It is illustrative to first show how a two-dimensional periodic, or 2-D periodic Poisson solver can be derived. To begin with, Poisson's equation is

$$\nabla^2 \phi(x, y) = -4\pi\rho(x, y) \quad , \quad (2.12)$$

where $\phi(x, y)$ and $\rho(x, y)$ are the electrostatic potential and charge density, respectively. Both are specified only on the grid intersection points and interpolated when they are used off the grid points. In two dimensions the grid lengths are assumed to be L_x and L_y . Taking the Fourier integral of both sides of Poisson's equation 2.12 gives

$$\frac{1}{L_x L_y} \int_0^{L_x} \int_0^{L_y} \nabla^2 \phi(x, y) e^{-i k_n x} e^{-i k_m y} dx dy =$$

$$\frac{1}{L_x L_y} \int_0^{L_x} \int_0^{L_y} \rho(x, y) e^{-i k_n x} e^{-i k_m y} dx dy$$
(2.13)

since $\nabla^2 \phi = \partial^2 \phi / \partial x^2 + \partial^2 \phi / \partial y^2$ the first integral can be integrated by parts, and if the Fourier coefficients are defined as

$$\phi_{nm} = \frac{1}{L_x L_y} \int_0^{L_x} \int_0^{L_y} \phi(x, y) e^{-i k_n x - i k_m y} dx dy$$
(2.14)

then Poisson's equation becomes a relationship between Fourier components

$$\phi_{nm} = 4\pi \frac{\rho_{nm}}{k_n^2 + k_m^2} .$$
(2.15)

What equation (2.15) means is just that an FFT must be performed on the charge density $\rho(x, y)$ to give the Fourier charge coefficients ρ_{nm} . By

dividing this by the quantity $(k_n^2 + k_m^2)$ for any particular n and m , and then multiplying by 4π gives the Fourier coefficients of $\phi(x, y)$, namely ϕ_{nm} . An inverse Fourier transform of ϕ_{nm} gives back $\phi(x, y)$, the desired quantity. Finally, the electric force can be computed by differencing $\phi(x, y)$ to get $E(x, y)$, since $E(x, y) = -\nabla\phi(x, y)$.

Now, it can be shown how the doubly periodic technique described above can be extended to more difficult boundary conditions. Two different techniques were developed for this thesis to handle a conducting boundary at one simulation surface. One technique uses the superposition principle in electrostatic theory and adds specially computed extra charge to the grid so that the potential at the conducting boundary is zero. This technique is very powerful and can handle complicated boundaries, but consumes almost twice as much computer time to accomplish the solutions over the doubly periodic method because two FFT's are required per timestep. The second technique was developed with the help of V. Decyk (1977) at UCLA. Decyk's technique has the advantage of only requiring one FFT per timestep at the expense of a more complicated theoretical framework which makes handling more complicated boundaries a somewhat more time consuming task.

2.3.1 Description of the Superposition Technique for a Rounded Poisson Solver

To begin with, we start out with the computational grid having N_x grid points in the x -direction and N_y grid points in the y -direction.

The boundary on which the potential is to be specified must lie on a subset of the $N_x \times N_y$ grid points. As long as the boundary lies on the main grid it can have any shape. It does not have to be continuous, although accuracy may suffer if the boundary is too complicated or has too many segments. The reason for this has to do with the inversion of the capacity matrix, which will be discussed later. We assume the boundary has N_b boundary points. In the case of a conducting, lower ionospheric boundary we would have $N_b = N_y$. N_b can take on any value from 1 to $N_x \times N_y - 1$. The boundary must be determined from the indices describing the grid point it lies on,

$$i(s), j(s) \quad s = 1, N_b \quad (2.16)$$

where s is a dummy integer index which keeps track of consecutive boundary points. In the code i and j are integer arrays. The potential must be specified at each of the boundary points.

$$\phi(i(s), j(s)) = \phi(s) \quad (2.17)$$

In most cases $\phi(s) = 0.0$ for all s . In the case of a real metallic or conducting boundary charges will accumulate along the conducting surface to maintain the surface potential. Hence, if the conductor is in a plasma, the charge distribution on the conductor will create a potential that exactly cancels the potential created by the plasma so that potential on the conductor does not change. The procedure that is

followed then is to compute the potential at each of the boundary points which is due to the plasma, and define this potential to be $\phi_{\text{plasma}}(i(s), j(s))$. Then the difference in potential between the plasma and the conductor can be calculated from

$$\Delta\phi(s) = \phi_{\text{plasma}}(s) - \phi_{\text{boundary}}(s) \quad . \quad (2.18)$$

Then additional charge is added to the boundary points to cancel $\Delta\phi(s)$ like nature would do. The additional charge represents the induced surface charge that would naturally occur on the conductor having the specified potential. The charge to be added can be computed from the capacity matrix as follows.

It is necessary to know the charge $\rho(s)$ needed to add along the boundary to cancel the difference potential $\Delta\phi(s)$. Considering $\rho(s)$ and $\Delta\phi(s)$ to be vectors with integer index s , we know that the potential at any point is just a linear superposition of the potential due to the induced charge at every other boundary grid point. Hence,

$$\nabla\phi(s) = \vec{M} \rho(s) \quad (2.19)$$

where \vec{M} is the capacity matrix. \vec{M} can be computed by placing a unit test charge at each boundary point and computing the resulting potential at every other point. If $\phi(s', s)$ is defined to be the potential at s due to a test charge at s' , then $\phi(s', s)$ are just the elements of the

capacity matrix. The capacity matrix is computed during the initialization process of the simulation. It only needs to be computed once. After it is calculated, its inverse must be computed because it is the inverse capacity matrix which is actually used during the simulation, through equation 2.19 which becomes

$$p(s) = \vec{M}^{-1} \Delta\phi(s) \quad . \quad (2.20)$$

Once this additional induced charge is computed it is added to the grid and the doubly periodic FFT can be used to get the electric field in the same manner as described earlier in the section. Two FFT's were required because one was needed to compute the potential due to the plasma at the boundary grid locations. The second was needed to compute the electric force after the induced surface charge was computed using the inverse capacity matrix and added to the simulation grid.

2.3.2 Description of the Bounded Fourier Poisson Solver

Decyk (1980) has developed a very efficient technique that is capable of handling some of the simpler boundary conditions. In his method, Poisson's equation is solved for the plasma assuming double periodic boundary conditions. Then an appropriate solution of Laplace's equations is found analytically so that the sum of the two solutions satisfies the boundary conditions.

The technique requires that the system be periodic in one direction, normally the y-direction. In this case, Poisson's equation

is just

$$\phi(x, y) = -4\pi\rho(x, y) \quad . \quad (2.21)$$

The Fourier integral in this direction gives

$$\phi_m(x) = \frac{1}{L_y} \int_0^{L_y} \phi(x, y) e^{-ik_m y} dy \quad , \quad (2.22)$$

so that 2.21 becomes

$$\frac{d^2 \phi_m(x)}{dx^2} - k_m^2 \phi_m(x) = -4\pi\rho_m(x) \quad . \quad (2.23)$$

This is a standard differential equation and its solution is just the sum of a particular solution and a solution of the homogeneous equation. A particular solution has already been found, and is just the doubly periodic result. The solution to the homogeneous equation is gained by

$$\phi_m(x) = \frac{4\pi\rho_{nm}}{k_n^2 + k_m^2} e^{ik_n x} + A_m e^{k_m x} + B_m e^{-k_m x} \quad . \quad (2.24)$$

A_m and B_m can be evaluated once the boundary conditions are specified. Appropriate boundary conditions for this thesis are the potentials

specified at $x = 0$ and the component of the electric field $E_x(L) = 0$ so that no accelerating potential is assumed or allowed to exist a priori. By setting $\phi_m(0) = 0$ and $E_x(L) = 0$, equation (2.24) becomes

$$\phi_m(x) = \frac{4\pi\rho_{nm}}{k_n^2 + k_m^2} e^{ik_n x} + \frac{1}{k_m \cosh(k_m + L_x)} - \frac{-ik_n}{k_n^2 + k_m^2} 4\pi\rho_{nm} \sinh(k_m x) - \frac{k_n^2 4\pi\rho_{nm}}{k_n^2 + k_m^2} \cosh k_m(L_x - x) \quad (2.25)$$

Then $\phi(x, y)$ is computed from

$$\phi(x, y) = \sum_m \phi_m(x) e^{ik_m y} \quad (2.26)$$

and the electric field computed from differencing as before.

2.4 Particle Handling at the Boundary

Kinetic theory predicts that the number of particles having speeds between v_x and $v_x + dv_x$ is given by

$$dN_{v_x} = \frac{N}{\sqrt{\pi} v_{th}} e^{-\left(\frac{v_x}{v_{th}}\right)^2} dv_x \quad (2.27)$$

The flux of particles moving in one direction can be found by integrating $v_x dN_{v_x}$ from zero to infinity,

$$\text{flux} = \int_0^{\infty} \frac{N}{v_{th} \sqrt{\pi}} v_x e^{-v_x^2/v_{th}^2} dv_x, \quad (2.28)$$

or

$$\text{flux} = \frac{N v_{th}}{2\sqrt{\pi}}. \quad (2.29)$$

Since $N = 2N_b$, where N_b is the beam, or sheet density, the number of particles per time step introduced from one of the boundaries is given by $N_b v_{th} / \sqrt{\pi}$. Special care had to be taken because equation 2.29 in general does not take integer values, and failure to account for this was observed to cause a loss of energy conservation in test runs.

3.0 Simulation of Two-Dimensional V-Potential Double Layers

The interaction of the auroral electron current sheet with the ionosphere can be studied in two planes, one containing the V-potential structure, and the other containing the deformations of the current sheet known as curls and folds. This is shown schematically in Figure 1.1. In this chapter, several simulation results are presented which suggest strongly that the formation of the V-potential structure and the acceleration of the auroral electron is a natural consequence of the interaction of a magnetized electron current sheet shielded by ambient ions with a conducting boundary. The interaction causes the formation of a V-shaped auroral double layer, a term used in the general sense of Kan and Lee (1981) because it incorporates all the proposed mechanisms (with the exception of Alfvén waves).

Because of the complexity of the model and resulting physics, it was instructive to develop the simulation in steps to show how the interaction of the acceleration mechanism (pitch angle effects, anomalous resistivity, and double layer formation) combine to form the acceleration mechanism. Hence, three different simulations are presented. The first and simplest contains the most essential features required for two-dimension double layer formation, but has a uniform magnetic field instead of a dipole field, and hence lacks the mirror effects. It also neglects the effect of the ionosphere on ion temperature by assuming that all ions are of plasma sheet origin. The

second simulation includes a dipole magnetic field and cool ionospheric ions. The results show the importance of the mirror force in forming a population of trapped electrons. The last simulation shows the additional effect of a background plasma.

In order to simulate the formation of the V -potential structure, the initial and boundary conditions must be specified, modeling the auroral environment as closely as possible under the constraint of limited computer time and core size. The initial and boundary conditions used in the simulations are shown schematically in Figure 3.1. The initial conditions used are:

- 1.) Electrons are loaded uniformly forming a current sheet. They have an initial temperature T_e and drift velocity v_D , added to their thermal velocity, with the initial drift aimed towards the lower conducting ionospheric boundary. In the simulation with a uniform magnetic field, the current sheet is given a thickness L , measured in electron Debye lengths. In the simulation with a converging magnetic field, the initial thickness of the electron sheet is computed to reflect the compression of the sheet by the converging dipole field.

- 2.) Initially, the ions are loaded with mass m_i , and temperature T_i , with their guiding centers on top of the electrons. To do this, the ion's velocity was chosen randomly from a Maxwellian generator, then the gyroradius and phase computed, and then

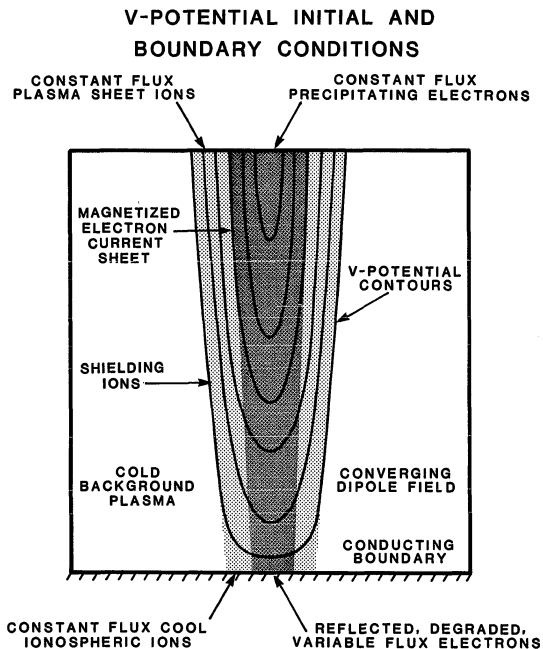


Figure 3.1 The initial and boundary conditions used for the V-potential simulation.

placed with the guiding center on an electron position. This initial loading does not form an ion sheath around the electron in perfect equilibrium, but was found to work well, and was very economical. The slight non-equilibrium caused some ion plasma oscillation perpendicular to the sheet, but these quickly damped out.

- 3.) In the simulations with a background plasma, the background electrons and ions were loaded uniformly throughout the simulation grid. The neutralizing background of thermal ions loaded with their guiding centers on top of the electrons, set up an electric field perpendicular to the sheet, due to their larger gyroradius they occupy a larger volume of space. The details of the initial particle loading are not observed to be important to the long term formation of the accelerating potential, which depends primarily on the boundary condition at the ionospheric and plasma sheet boundaries.

The boundary conditions we have used to model the auroral environment in this study are as follows:

- 1.) A lower conducting boundary to model the ionospheric effect. The Pedersen conductivity is much greater in the ionosphere than in the accelerating region above it, so that we can model

the ionosphere as an equipotential surface at the lower edge of our simulation. We assume $\phi = 0.0$ at $x = 0.0$.

- 2.) An upgoing flux of electrons is introduced from the ionospheric boundary, representing three different electron sources. They are: mirroring primary electrons reflected at their incident energy, backscattered secondary electrons which are energy degraded by collisions in the ionosphere (their energy is degraded by 6% in the simulations shown), and cold ionospheric electrons. The flux of the upgoing electrons is varied to maintain overall charge neutrality in the simulation. (Other combinations of handling the particles at the boundaries were tried, but resulted in unstable accelerating potentials.)

- 3.) An upgoing constant flux of ionospheric ions is injected from the lower boundary, in some simulations having a temperature ratio $T_e/T_i = 1$ with the ionospheric electrons, from a half-Maxwellian reservoir.

- 4.) A constant current electron sheet is introduced at the upper "plasma sheet" boundary. The sheet is assumed to be a drifting Maxwellian. In the special case of zero drift half-Maxwellian source was used.

- 5.) A constant flux of hot plasma sheet ions having a temperature ratio $T_e/T_i < 1$ with respect to the plasma sheet electrons introduced from a half-Maxwellian source from the upper "plasma sheet" boundary.

- 6.) A converging dipole magnetic field. This magnetic field magnetizes the electron sheet and provides for the mirroring of both ions and electrons of plasma sheet origin. It also provides for a population of electrons trapped between the mirror and the accelerating potential after it develops.

- 7.) A cold background plasma uniformly distributed throughout the simulation grid, but free to interact with the current sheet during the simulation run.

The potential drop along the field lines is not applied, but is allowed to evolve self-consistently as a result of the interaction. This is different from previous double layer simulations and laboratory experiments where the potential drop and/or the total current was externally given so that the origin of the electron acceleration process remains unexplained. The total current is not fixed by the particle sources at the boundaries because the flux of upgoing electrons from the ionosphere fluctuates to maintain overall charge neutrality and particles are free to leave the system through any boundary. However, when the double layer potential becomes large enough to trap upstreaming

electrons and downstream ions between double layer and the boundaries, then the current is controlled by the electron current source and the upstreaming ions.

On the basis of the present simulation study the following physical picture has emerged in an attempt to explain the presently available observations on the auroral potential structure. A magnetized sheet of current-carrying electrons and hot shielding ions (of plasma sheet origin) is injected through a cool background plasma towards a conducting (ionospheric) boundary. As the hot ions try to shield the current sheet, a potential drop forms perpendicular to the magnetic field as a result of their larger Larmor radius (the potential contours being parallel to the magnetic field). The partially shielded electron beam approaches the conducting boundary and is accelerated towards it, because the electrons near the boundary "see" their oppositely charged images on the other side of the boundary. As the electron sheet beam reaches the conductive layer, the potential contours close, forming a V-shaped potential structure. The resulting potential drop is limited by the plasma sheet ion kinetic energy T_i , which is in agreement with a two-dimensional, double layer solution to Poisson's equation for a steady-state condition (Kan et al., 1979).

However, once the electrons become accelerated, or if their initial drift velocity is high enough, they excite electrostatic waves through the electron-ion two-stream instability, and they become trapped in the waves. When this occurs, the total potential drop results from the interaction potential (limited by T_i), and anomalous resistivity

(unlimited by T_i). Thus, the double layer develops in a two-step process involving both the conducting boundary and the effects of anomalous resistivity. The backscattered and mirroring electrons play a crucial role because without them the double layer is not stable and the collisionless plasma is unable to sustain a steady-state voltage drop. They also distribute the potential drop over many more Debye length than is observed otherwise. The simulation shows that not only does a double layer solution exist, but it forms spontaneously and remains stable provided that the proper initial and boundary conditions are met. This is the first two-dimensional simulation which shows that a double layer can form under auroral conditions, and demonstrates that it is capable of accelerating the current-carrying electrons to the observed energies.

3.1 V-Potential Double Layers in a Uniform Magnetic Field

The simulation is carried out according to the bounded $2^{1/2}$ -dimensional electrostatic algorithm described earlier periodic in the y -direction, and bounded in the x with the potential $\phi = 0$ specified at $x = 0$ (the conducting boundary) and $E_x = 0$ at $x = N_x \Delta$. This simulation is also described in Wagner et al. (1980). The current-carrying electrons are magnetized and remain as a sheet of finite thickness L_y immersed in hot ions. At $x = 0$, downstreaming electrons are reflected up by degrading the energy by 6%. The reflected electrons are to simulate backscattering of the energy-degraded primary electrons, which we find to play an important role in the formation of the V-potential double

layer. Typical parameters employed are grid size $N_x \times N_y = 128 \times 32$, $L_y = 6\Delta$, the particle number 32,768, $v_D = 0.76v_{th}$, where v_{th} denotes electron thermal velocity, the electron cyclotron and plasma frequencies $\Omega_e = 2\omega_{pe}$, the mass ratio $m_i/m_e = 10$, and the electron Debye length $\lambda_{De} = \Delta$.

Figure 3.2 shows the potential structure, the electron and ion phase spaces at $t = 2500\omega_{pe}^{-1}$. (Figures 3.2(a)-3.2(c) for the case with temperature ratio $T_e/T_i = 0.2$, while (d)-(f) for a cooler in case with $T_e/T_i = 0.6$.) The temperature ratio $T_e/T_i = 0.2$ more closely models magnetospheric conditions. A field-aligned potential drop is observed in both cases. A double layer structure is evident in the ion and electron phase spaces for both sequences. In time, the double layer structure approaches steady state around $75\omega_{pe}^{-1}$, and remains for the length of the run (up to $2500\omega_{pe}^{-1}$).

The potential for the case $T_e/T_i = 0.2$ shows that the majority of the potential drop ($0.7T_i$) occurs over a short distance of $6\lambda_{De}$ and then continues to increase at a slower rate, but to considerably higher energy ($21T_i$) over a distance of $100\lambda_{De}$. This suggests that there are two complementary mechanisms which produce the total potential drop when the T_e/T_i ratio increases toward unity. The first mechanism occurs only within $\sim 7\lambda_{De}$ and the potential is limited by the ion kinetic energy; this is the same for the case $T_e/T_i = 2$. The second mechanism operates when T_e approaches or becomes greater than T_i . Associated with this "additional potential drop" is the prominent electron trapping by large amplitude electrostatic waves as seen in Figure 3.2(e). These waves are

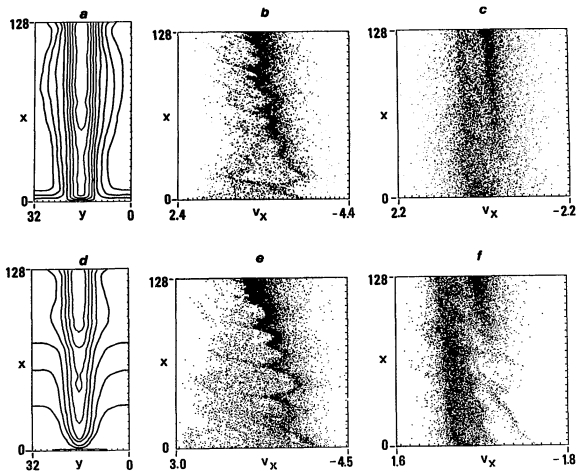


Figure 3.2 Double layers at $t = 2500\omega_{pe}^{-1}$. (a)-(c) $T_e/T_i = 0.2$; (d)-(f) $T_e/T_i = 0.6$.

due to the Buneman instability excited by the accelerated electrons. Since the most unstable wave number $k \sim \omega_{pe}/v_D(x)$ changes as the electron beam is accelerated, the electron phase space modulation wavelength increases as the beam propagates toward the conducting boundary. The wavelength of the vortex structure can be scaled approximately by $\lambda(x) = 2\pi v_D(x) \omega_{pe}^{-1}$. The trapping of electrons by these waves can lead to an increase of the effective resistivity (anomalous electron dragging) and thus contributes to the additional voltage drop distributed over the length where the instability is active.

The effective collision frequency associated with the additional voltage drop as a function of the temperature ratio T_e/T_i is shown in Fig. 3.3(a). The effective collision frequency ν_e^* is determined by the effective conductivity $\sigma^* = \omega_{pe}^2/4\pi\nu_e^*$, where the conductivity is measured by electronic current density divided by the electric field at the location where the additional drop takes place. When T_e/T_i reaches about 1, the effective collision frequency becomes well over the level given by normal collisions ν_e . Figure 3.3(b) indicates that the two-dimensional double layer potential provides approximately the same amount of voltage drop ϕ/T_i irrespective of T_e/T_i . The total voltage drop ϕ/T_i across the system, however, increases as T_e/T_i increases. At the same time, the V-shaped equipotential lines become more and more straight horizontal stripes, i.e., one-dimensional structure. For larger temperature ratios (T_e/T_i), it is easier to overcome the threshold of the Buneman instability as well as those of the ion-acoustic and ion-cyclotron instabilities.

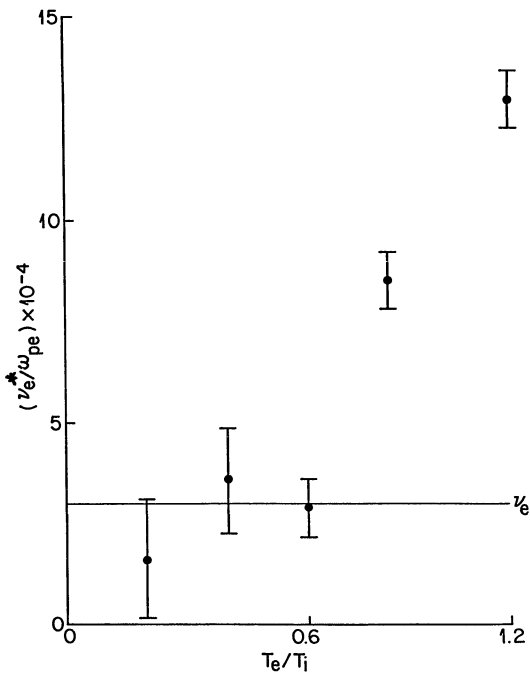


Figure 3.3 (a) The effective collision frequency as a function of temperature ratio.

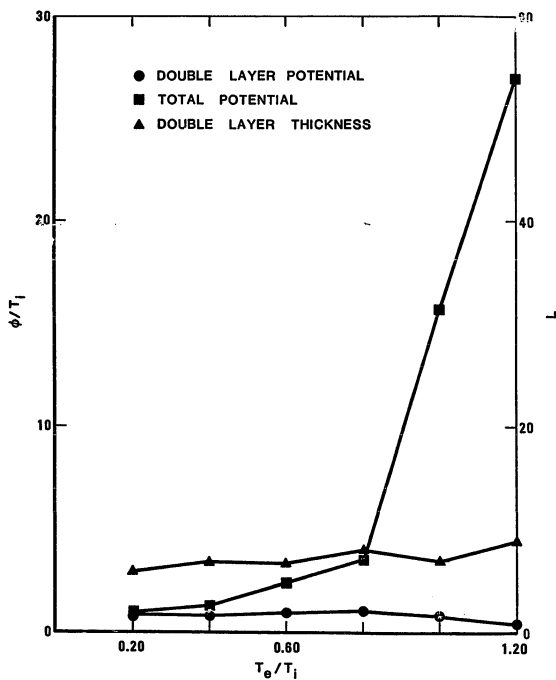


Figure 3.3 (b) The double layer voltage drop as a function of temperature ratio T_e/T_i .

The present simulation of the two-dimensional V-potential double layer reproduces many of the features which are found in the formation of auroral arcs. The essential elements include a field-aligned electron sheet current interacting with the surrounding magnetospheric ions and the conducting ionosphere. The stable two-dimensional double layer accelerates electrons to the energy of the ambient hot ions in agreement with the observations for the case of $T_e/T_i \sim 0.2$ which is reasonable in the plasma sheet. In this temperature-ratio regime $T_e/T_i < 0.6$, the contribution of anomalous resistivity to the acceleration of electrons is not important (see Fig. 3.2(a)); it becomes important when $T_e/T_i \geq 0.6$. The tendency of increasing potential drop in the double layer for increasing field-aligned electron velocity $v_D(L)$ (see Fig. 3.4) is also consistent with auroral observations: A brighter aurora is associated with a higher intensity of the field-aligned current. When the temperature ratio is fixed at $T_e/T_i = 0.2$, the structure stays as V-shaped even when $v_D(L)$ is increased; the length of the double-layer is found to be proportional to v_D as shown in Figure 3.4.

3.2 V-Potential Double Layer in a Dipole Mirror Field

In this section two simulations are described which include a converging dipole field and cool ionospheric ions. These simulations are also described in Wagner et al. (1981). The first computer run is with zero drift velocity for the electron current sheet (the current is from a half-Maxwellian source) and the other computer run with a drift velocity of $0.75 v_{th}$, where v_{th} is the electron thermal velocity at the

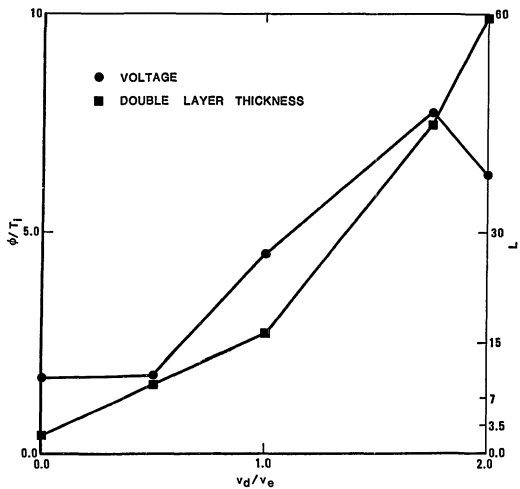


Figure 3.4 Properties of the double layer as a function of electron drift velocity $v_d(L)$.

plasma sheet boundary. The boundary conditions used are periodic in the y -direction and bounded in the x -direction with the potential $\phi = 0$ specified at $x = 0$ (the conducting boundary) and $E_x = 0$ at $x = N_x \Delta$ ($\Delta = 2 \lambda_{De}$ is the grid distance). Typical parameters employed are grid size $N_x \times N_y = 256 \times 128\Delta$, L_y (electron sheet thickness) $= 6\Delta$, the particle number 65,536, the electron cyclotron and plasma frequencies $\Omega_e = 4.4 \omega_{pe}$ at the ionospheric boundary and $\Omega_e = 4.0\omega_{pe}$ at the plasma sheet boundary (this is a magnetic field convergence of 10% over 512 Debye lengths). These parameters model the auroral environment as accurately as our computer resources will allow.

3.2.1 The $v_D = 0$ Case

Results from the $v_D = 0$ case shown in Figure 3.5, taken at time $\tau = 400\omega_{pe}^{-1}$. The electron positions are shown in Figure 3.5(a), the ion positions in 3.5(b). The slight field line convergence is evident in Figure 3.5(b). The hotter ions near the plasma have a higher temperature, and hence a larger gyroradii. This causes a larger potential drop perpendicular to the sheet (near the upper boundary) as seen in the contour plot 3.5(e). The electron phase space is shown in 3.5(c) and the ion phase space in 3.5(d).

The most important feature of this simulation is that a quiet, stable double layer has formed and the resulting potential drops in a linear fashion (Figures 3.5(e) and 3.5(f)) between the upper and lower boundaries. This extended distribution of the potential across the grid is in contrast to the results in the previous section with the uniform

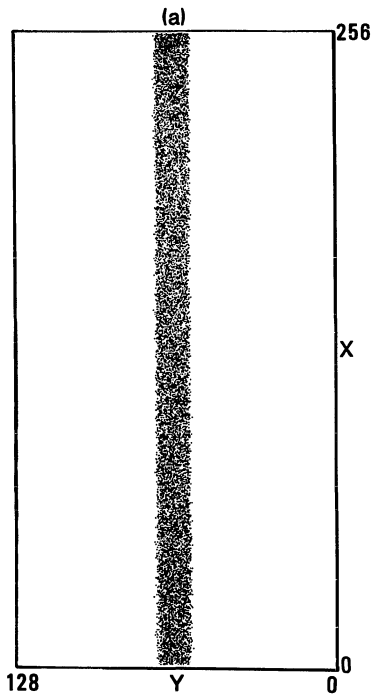


Figure 3.5 (a) The electron positions for a simulation including the mirror effects of a dipole field, at time $\tau = 400\omega_{pe}^{-1}$.

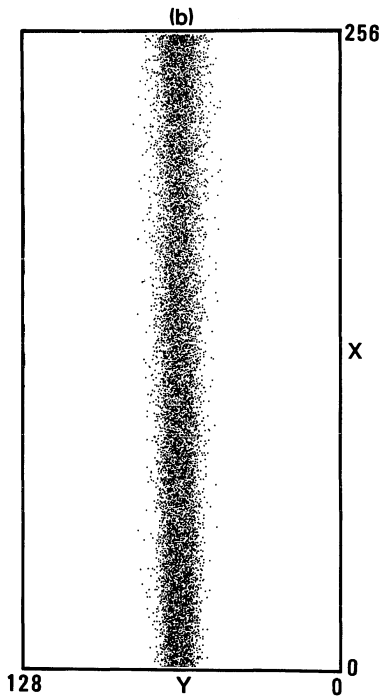


Figure 3.5 (b) The ion positions.

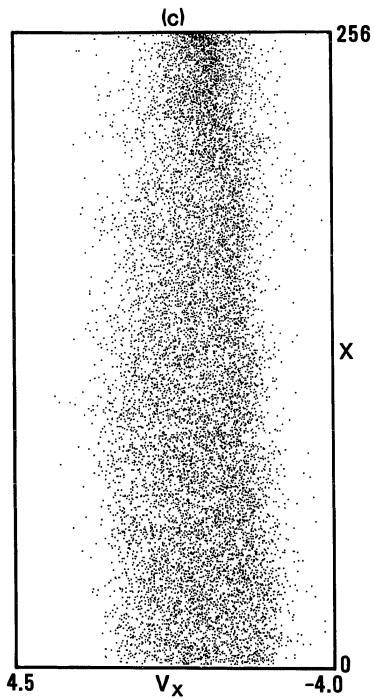


Figure 3.5 (c) The electron phase space $v(x)$ vs. x for this simulation.

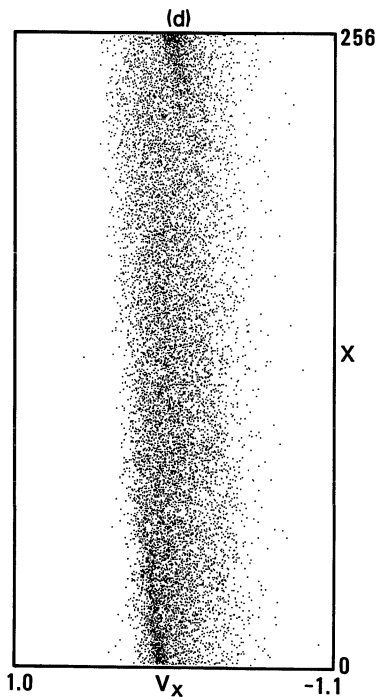


Figure 3.5 (d) The ion phase space $V(x)$ vs. x for this simulation.

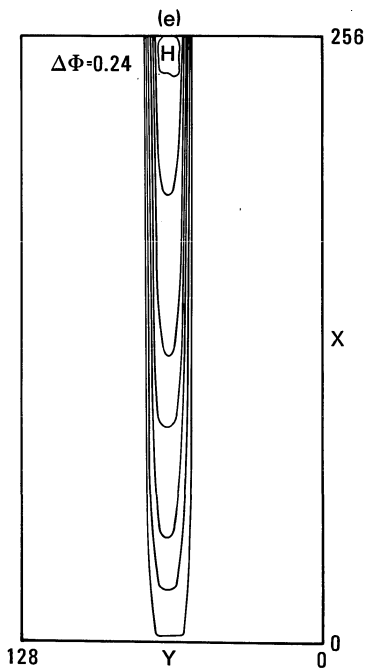


Figure 3.5 (e) Equipotential contours for the double layer.

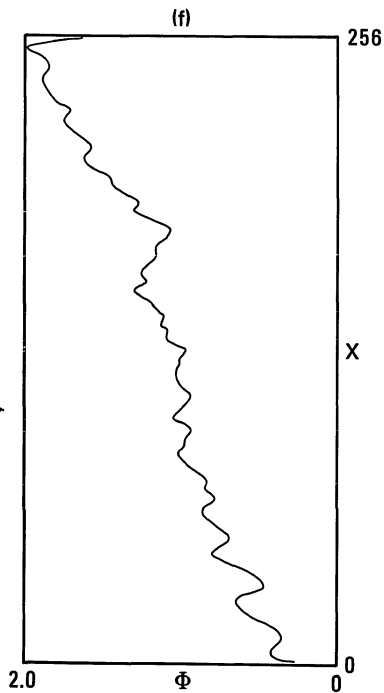


Figure 3.5 (f) The potential down the center of the current sheet.

magnetic field. In this simulation the dipole field naturally supplies the population of mirroring particles, some of which become trapped between the double layer and the mirror. This population allows the double layer to extend over many Debye lengths, and not to concentrate near the lower conducting boundary.

The net potential drop is slightly less than the ion kinetic energy at the plasma sheet, $0.8T_i$. It is important to notice in the electron phase space 3.5(c) that the electrons from the plasma sheet are accelerated into the ionosphere with a beam velocity 3-4 times than the electron thermal velocity in the plasma sheet almost equal to the ion kinetic energy. These electrons are plotted near the lower right edge of phase space in Figure 3.5(c). A very large population of electrons trapped between the mirror and the potential drop, and a large population of backscattered degraded primaries are also evident (the degraded primary is almost, but not quite, able to reach the upper plasma sheet boundary). These electrons are plotted along the verticle center-line, and left of the center-line respectively, in the phase space Figure 3.5(c). In the ion phase space Figure 3.5(d) some, but very few, of the plasma sheet ions have sufficient energy to reach the ionospheric boundary. These ions are found plotted with negative (downward) velocities near the lower boundary in Figure 3.5(d). The cold ionospheric ions can be seen to be heated and accelerated as they pass through the double layer, which has a thickness of about $51\lambda_D$. The fact that the electron current source is half-Maxwellian means that the drift velocity is too low to satisfy the Block criterion. The

presence of the trapped electrons, not included in the Block model, still allows the double layer to form, in agreement with the recent results of Kan et al. (1980a, 1980b).

The spatially integrated velocity distribution functions for the electrons and ions is shown in Figure 3.5(g). The $f(v_x)$ curve shows the electrons are accelerated into the ionosphere because the bell-shaped curve is displaced in the negative (downward) direction. The ion distribution function $f(v_x)$ is skewed because of the large number of downward traveling plasma sheet ions. Both electrons and ions show an undisturbed Maxwellian distribution for $f(v_y)$ which is important because no heating process is operative in the direction perpendicular to the magnetic field.

3.2.2 The $v_D = 0.75$ Case

The second simulation example with ($v_D = 0.75v_{th}$) is shown in Figure 3.6. The figures are taken at time $\tau = 400\omega_{pe}^{-1}$. Figures 3.6(a) and 3.6(b) show the electron and ion positions respectively. A noticeable density depression occurs in the region of maximum potential drop, from $x = 80 \lambda_{De}$ to $x = 200 \lambda_{De}$. This is seen in the central region of the column plotted in Figure 3.6(a). The ion positions are plotted in Figure 3.6(b). The electron phase space 3.6(c) shows the plasma sheet electrons being accelerated through a double layer into the ionosphere at 6-8 times their initial thermal velocity. A large population of trapped, degraded primary and secondary electrons are also evident in phase space, although none are able to pass through the

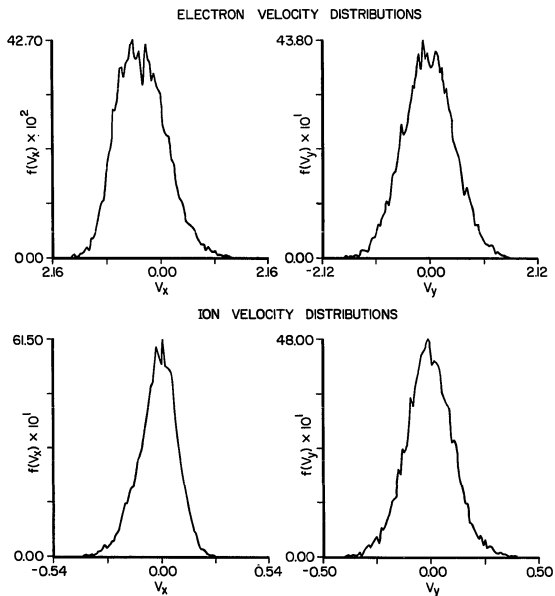


Figure 3.5 (g) Velocity distribution functions.

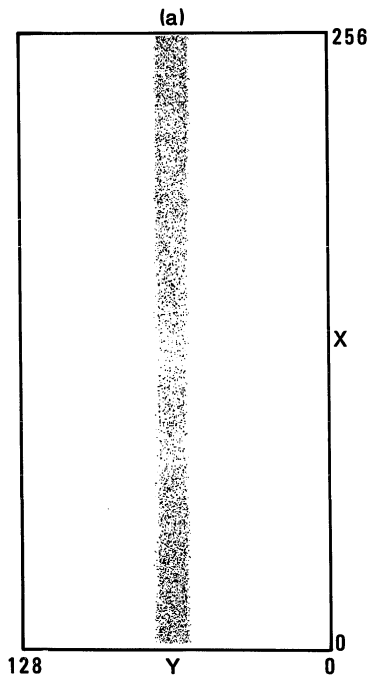


Figure 3.6 (a) The electron position for a simulation including the mirror effects of a dipole field, at time $\tau = 400\omega_{pe}^{-1}$.

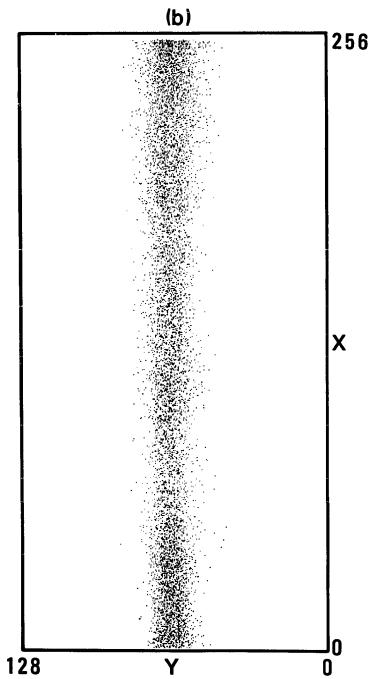


Figure 3.6 (b) The ion positions for this simulation at the same time, $\tau = 400\omega_{pe}^{-1}$.

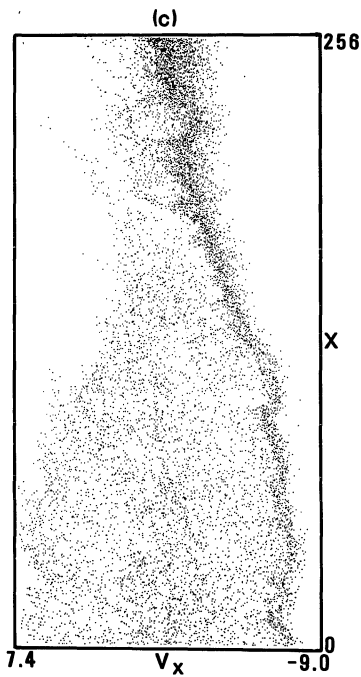


Figure 3.6 (c) Electron phase space.

double layer to reach the upper boundary. These trapped and degraded electrons are those plotted to the left of the accelerated beam in the region below $x = 200$. Significant electrostatic waves due to the Buneman electron-ion two stream instability are excited and are capable of trapping some of the current-carrying electrons. The most unstable wave number for Buneman waves is $k \sim \omega_{pe}/v_d$, which changes as the electron beam is accelerated, so that the electron phase space modulation wavelength increases as the beam propagates toward the conducting boundary. The wavelength of this vortex structure can be scaled by $\lambda(x) = 2\pi v_d \omega_{pe}^{-1}$. The trapping of electrons by these waves can lead to an increase of the effective resistivity (anomalous electron dragging) and thus contributes to the additional voltage drop distributed over the length where the instability is active.

Figure 3.6(d) show the ion phase space at this same time $\tau = 400\omega_{pe}^{-1}$. The hot plasma sheet ions with negative velocities are plotted near the top of the figure. To the left and also below these downgoing and reflected ions the upgoing accelerated ions are plotted. The acceleration region near the center of the plot is where the ions are accelerated, and is exhibited by the vertical strip of upgoing ions bending to the left, indicating higher positive (upward) velocities.

The spatially averaged electron velocity distribution functions for v_x and v_y are shown in Figures 3.6(e) and 3.6(f), respectively (notice the velocity scales in the two figures are not the same). Figure 3.6(e) shows the various populations of electrons, the accelerated beam with negative velocities 4-6 times the initial thermal velocity are plotted

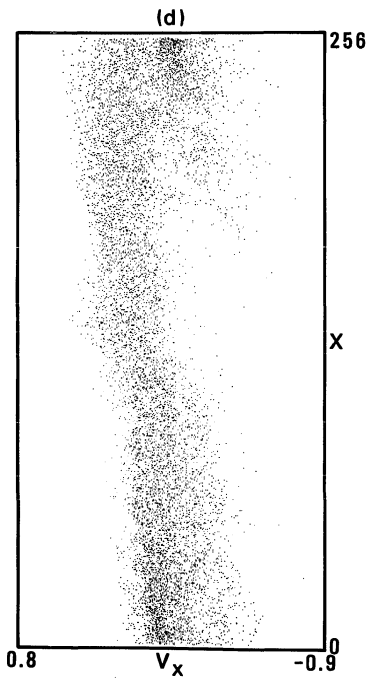


Figure 3.6 (d) Ion phase space.

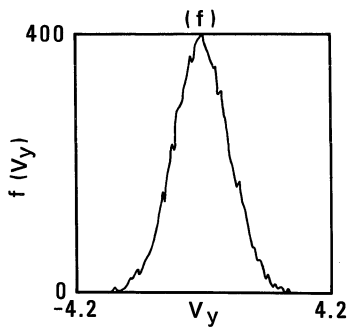
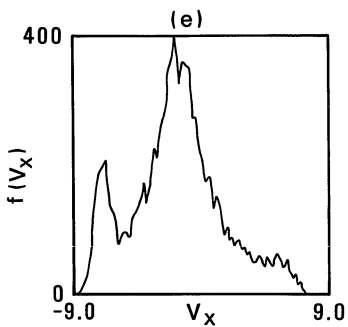


Figure 3.6 (e), (f) Spatially integrated velocity distribution functions for the electrons.

on the left hand side of the distribution in Figure 3.6(e). The trapped electrons near the thermal velocity form the part of distribution function near $v_x = 0$ in the center of the plot, and the energy degraded primaries streaming upwards with positive velocities on the right side of the curve. Note that there is no significant heating of the electrons in $f(v_y)$, since 3.6(e) shows an undisturbed Maxwellian distribution. Figure 3.6(g) shows the potential drop a function of x at $y = 64 \lambda_{De}$ (the center of the sheet). The magnitude of the potential drop is $16T_e$, or 6 times the ion thermal energy at the plasma sheet. These quasi-stable strong double layers occur whenever the accelerated drift velocity of the beam exceeds the Buneman threshold over a significant region of the simulation grid.

3.3 The Effects of a Background Plasma on Double Layer Formation in a Dipole Mirror Field

In this section, a simulation will be described which includes a background plasma. The other simulation features are very similar to the previous simulations. Initially the current sheet electrons are loaded with a sheet thickness of $6 \lambda_{De}$ at the plasma sheet boundary, with a temperature T_e , and an initial drift velocity $v_D = v_{th}$ where v_D is the electron drift velocity and v_{th} is the electron thermal velocity. The ions are loaded with their guiding centers on top of the electrons, having a temperature $T_i = 5T_e$ at the plasma sheet and $T_i = T_e$ at the ionospheric boundary. The background plasma is initially loaded uniformly over the computational grid, and is assumed to be cold. These

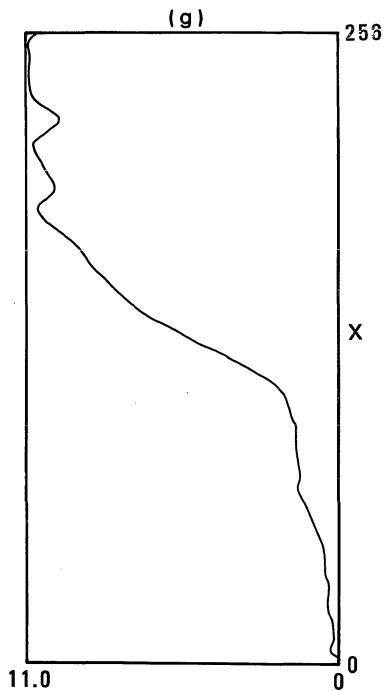


Figure 3.6 (g) Potential drop as a function of x down the center of the double layer.

initial conditions can be seen in Figure 3.7(a), which shows the electron positions at $\tau = 0.0\omega_{pe}^{-1}$, and Figure 3.7(b) which shows the initial ion positions, also at $\tau = 0.0\omega_{pe}^{-1}$. The convergence of the magnetic field can be seen, along with the cooler ionospheric temperature, and the background plasma particle locations. The code is the $2^{1/2}$ -D bounded electrostatic algorithm described earlier, with the lower boundary assumed to be infinitely conducting, with potential arbitrarily set to zero, at $x = 0$. The grid used $N_x \times N_y = 256 \times 128\Delta$, with $\Delta = \lambda_{De}$ the grid size. The particle number used was 131,072. The electron cyclotron and electron plasma frequencies used are $\Omega_e = 4.4\omega_{pe}$ at the ionospheric boundary, and $\Omega_e = 4.0\omega_{pe}$ at the plasma sheet boundary. This corresponds to a magnetic field convergence of 10% over 256 Debye lengths. The particle size used was $a_x = a_y = \Delta$. In the following sections the development of the V-potential structure is described at several times, $\tau = 40\omega_{pe}^{-1}$, $120\omega_{pe}^{-1}$, $200\omega_{pe}^{-1}$, $320\omega_{pe}^{-1}$ and $400\omega_{pe}^{-1}$.

3.3.1 The Simulation at $\tau = 40\omega_{pe}^{-1}$

Figure 3.8(a) shows the electron phase space at $\tau = 40\omega_{pe}^{-1}$ with the velocity v_y plotted on the horizontal axis and position x plotted on the vertical axis. The cold background electrons have negligible velocity and can be seen as the thin vertical strip in the center of the plot. Several features are important in the plot. The electron beam, with its initial downward (negative) velocity is Buneman unstable. Regions of strong trapping occur, which can be seen as the eddy structures (the

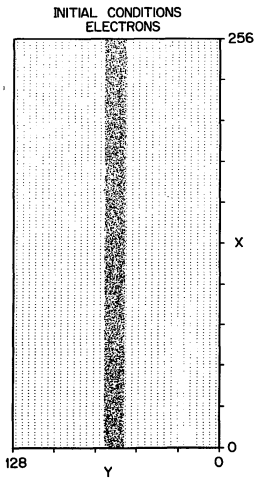
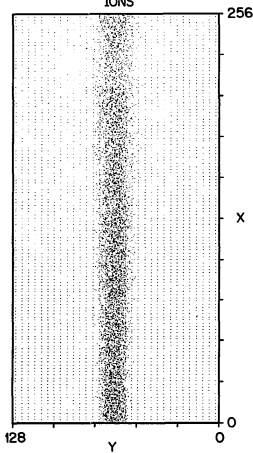


Figure 3.7 (a) The electron position at $t = 0$.
(b) The initial ion positions.

INITIAL CONDITIONS
IONS



$= 0.0\omega_{pe}^{-1}$ including the dipole field

elliptical regions of trapping stacked on top of each other in the figure). Near the conducting boundary, from $x = 50 \lambda_{De}$ to $x = 0 \lambda_{De}$ the electron beam is accelerated into the ionosphere with a final velocity of twice its initial drift velocity. These accelerated electrons are on the right hand side near the lower edge of Figure 3.8(a). Some backscattered electrons, along with degraded primaries can be seen coming up from the ionosphere, but the population is in the very early stage of development at this early time.

Figure 3.8(b) shows the ion phase space at $\tau = 40\omega_{pe}^{-1}$, the same time as the electrons just discussed. The cold background ions form the thin vertical stripe in the center of the plot. The converging appearance of the ions in phase space is due to the initial distribution of ion temperature as a function of height. Cooler ions are at the lower boundary with hotter (plasma sheet) ions at the upper boundary. The mass ratio $m_i/m_e = 64$ is used. These heavy ions move slower than their electron counterparts and therefore the ion phase space shows little change from its initial configuration. The electric potential contours are shown in Figure 3.9(a). The separation between contours is $\Delta\phi = 0.4T_e$, and the total potential drop is nearly equal to $4.5T_e$, very close to the plasma sheet ion temperature ($T_i = 5T_e$). There is a minor leakage of the potential into the background plasma. Whenever the local accelerating potential differs from the potential drop perpendicular to the sheet there is leakage of the potential into the background plasma. In these cases the potential contours of the V-shaped potential can reach the simulation side boundaries. This can provide some heating

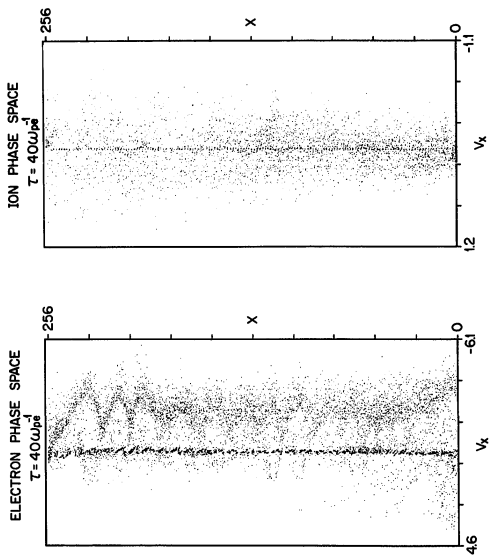


Figure 3.8 (a) Electron phase space at $\tau = 40 \omega_{pe}^{-1}$.
 (b) Ion phase space at $\tau = 40 \omega_{pe}$.

of the neighboring background plasma, and will be discussed more later. Since the lower boundary is conducting all contours very near to it must lie parallel to it, and this is also seen. Figure 3.9(b) shows the potential down the center of the V-shaped contours, $\phi(x)$ vs. x , at the same time as for the contour plot. The potential drops almost linearly between boundary, but is modulated slightly by the electric field responsible for the Buneman trapping, and falls off somewhat more steeply near the conducting boundary because of the interaction of the electrons with the ionospheric boundary.

3.3.2 The Simulation at $\tau = 120\omega_{pe}^{-1}$

Figure 3.10(a) shows the electron phase space at a later time, $\tau = 120\omega_{pe}^{-1}$. The strong Buneman instability observed earlier has almost saturated, but can still be seen. Buneman trapping can be identified because its wavelength is a function of drift velocity, faster electron drifts cause longer wavelength instabilities and wider trapping regions. Hence, short wavelength trapping regions occur near the current source while larger regions occur progressively as the beam is accelerated into the ionosphere. The wavelength of the instability scales according to $\lambda = 2\pi v_D(x)\omega_{pe}^{-1}$. The saturation process is almost complete throughout most of the simulation, and can be verified by noticing that the beam is not accelerated from almost $x = 180 \lambda_{De}$ to $x = 0 \lambda_{De}$, but drifts along at an accelerated $v_D = 3 v_{th}$, three times the initial drift. At this time most of the acceleration occurs near the upper boundary from $x = 256 \lambda_{De}$ down to $x = 180 \lambda_{De}$, a distance of about

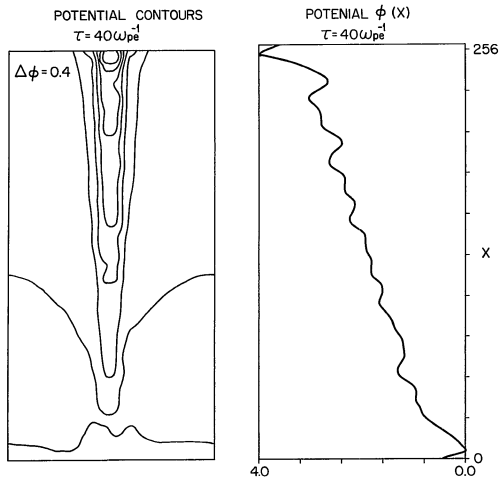


Figure 3.9 (a) Electric potential contours at $\tau = 40\omega_{pe}^{-1}$, with a spacing of $\Delta\phi = 0.4T_e$.
 (b) The electric potential down the center of the current sheet.

$80 \lambda_{De}$. Earlier in the simulation the potential drop was more linear, enhanced near the ionospheric boundary. At this later time, the potential drop is not so linear, because anomalous resistivity due to Buneman wave trapping has saturated, and growing population of trapped and degraded primary electrons near the ionospheric boundary have begun to shield out the effect of the boundary on the current sheet. Some heating of the background electrons is evident at this time. The ion phase space, in Figure 3.10(b), shows that the ions have not had much of a chance to respond to accelerating potential, although downward traveling ions do show some structure, resulting from the Buneman waves. A density enhancement is in the early stages of formation near the plasma sheet boundary.

Figure 3.11(a) shows the electric potential contours at the same time $\tau = 120 \omega_{pe}^{-1}$, with the potential contours spaced $\Delta\phi = 0.5 T_e$ apart. One can see that the lower half of the simulation is essentially equipotential. A V-shaped double layer has formed near the upper boundary, and drops its potential over about $80 \lambda_{De}$. The double layer potential is equal to the plasma sheet ion kinetic energy. This is verified by Figure 3.11(b) which shows the potential drop down the center of the current sheet. It shows that 2/3 of the potential drop occurs across the double layer, and 1/3 across in the lower part of the simulation grid, and this latter potential drop is due to anomalous resistivity and ionospheric interaction.

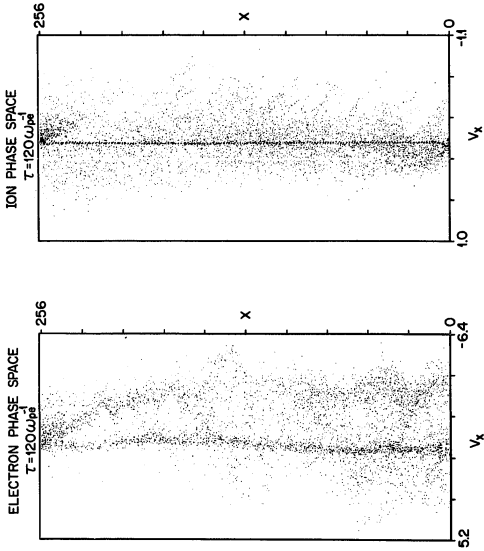


Figure 3.1.0 (a) Electron phase space at time $\tau = 120\omega_{pe}^{-1}$.
 (b) Ion phase space at time $\tau = 120\omega_{pe}^{-1}$.

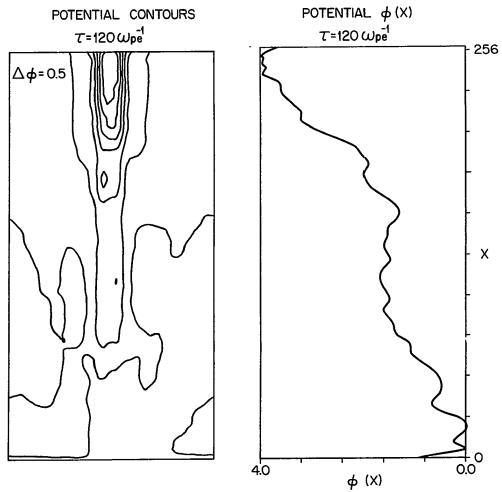


Figure 3.11 (a) Electric potential contours at $\tau = 120\omega_{pe}^{-1}$, with a separation of $\Delta\phi = 0.5T_e$.
 (b) The electric potential down the center of the double layer.

3.3.3 The Simulation at $\tau = 200\omega_{pe}^{-1}$

Figure 3.12(a) shows the electron positions at a later time $\tau = 200\omega_{pe}$. A naturally forming density gradient has formed, with the higher density region near the upper plasma sheet boundary, before the beam is accelerated by the potential. The background plasma remains uniformly distributed. Figure 3.12(b) shows a similar distribution for the ions.

Figure 3.13(a) shows the electron phase space at the same time as the positions shown, $\tau = 200\omega_{pe}^{-1}$. The Buneman instability, which had saturated, has begun to reinstate itself. Figure 3.13(b) shows the ion phase space at this same time. The background ions are still evident, with no change. The density buildup near the plasma sheet boundary of downward traveling ions can be seen. The ionospheric ions traveling up from the ionosphere show they are heated as they are accelerated upwards.

The resulting V-shaped potential is shown in Figure 3.14(a), where the contours are separated by $\Delta\phi = 0.4 T_e$. The potential plot in Figure 3.14(b) shows the potential drop down the center line of the V-shaped potential. Most of the potential drop occurs from $x = 256 \lambda_D$ down to $x = 128 \lambda_D$, dropping over a distance of about $128 \lambda_D$. This drop across the double layer has moved down from the previous plot from the upper boundary. The noise, around $x = 200 \lambda_{De}$ is due to Buneman waves.

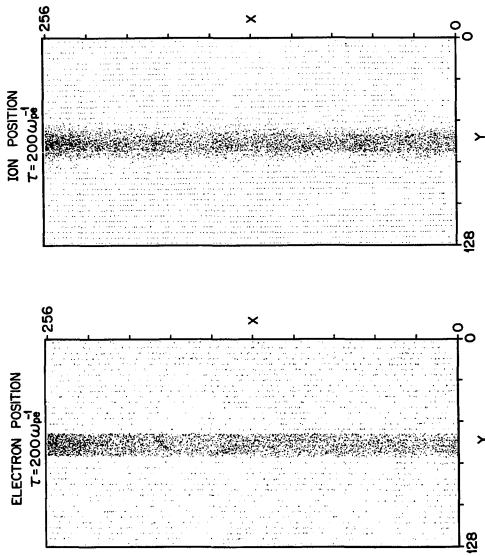


Figure 3.12 (a) Electron positions at time $\tau = 200\omega_{pe}^{-1}$.
 (b) Ion positions at time $\tau = 200\omega_{pe}^{-1}$.

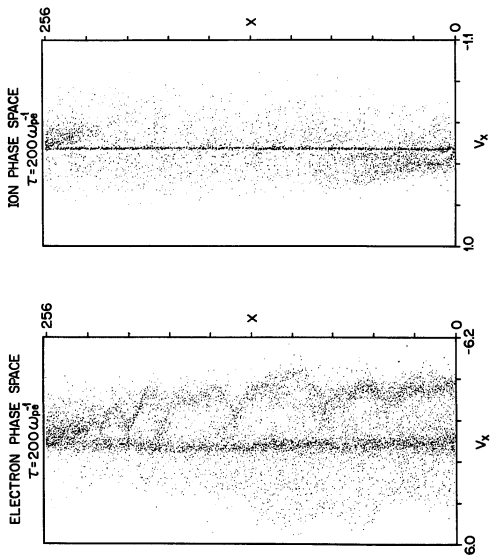


Figure 3.13 (a) Electron phase space at time $\tau = 200\omega_{pe}^{-1}$.
 (b) Ion phase space at time $\tau = 200\omega_{pe}^{-1}$.

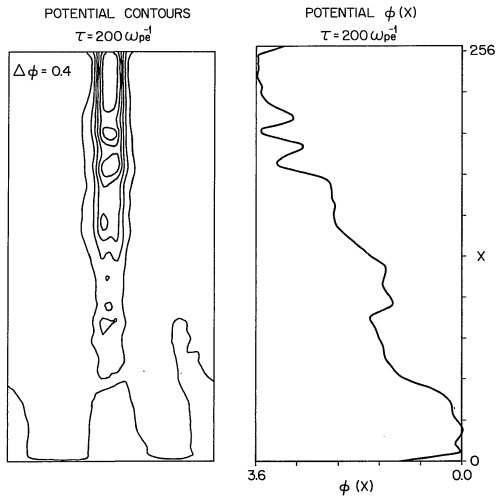


Figure 3.14 (a) Potential contours at time $\tau = 200 \omega_{pe}^{-1}$ spaced $\Delta \phi = 0.4 T_e$ apart.
 (b) The potential down the center of the double layer at time $\tau = 200 \omega_{pe}^{-1}$.

3.3.4. The Simulation at $\tau = 320\omega_{pe}^{-1}$

Figure 3.15(a) shows the electron phase space at time $\tau = 320\omega_{pe}^{-1}$. The electrons entering at the plasma sheet boundary are accelerated into the ionosphere at almost five times its initial drift velocity. A considerable population of degraded and mirroring primaries has built up underneath the acceleration region. The Buneman waves have saturated and not reappeared since the last time plotted. Continued heating of the background plasma is evident from the thickening of the vertical stripe of background electrons centered in phase space diagram. The phase space diagram for the ions at this same time is shown in Figure 3.15(b). The down flowing plasma sheet ions are becoming trapped above the acceleration region, hence, there is a depletion of downward traveling ions on the right (negative) side of the phase space plot. The ionospheric ions are accelerated and heated and they travel up through the acceleration region. The potential counterpart in Figure 3.15(a), with contours spaced $\Delta\phi = 0.6$ apart shows a potential double layer which is formed roughly half-way between the two boundaries. Once again the total potential drop is very nearly equal to the plasma sheet ion kinetic energy. Beneath the double layer the plasma both background and current sheet. The potential drop falls over the region $x = 30 \lambda_{De}$ to $x = 80 \lambda_{De}$, a distance of $140 \lambda_{De}$.

3.3.5 The Simulation at $\tau = 400\omega_{pe}^{-1}$

The electron position of time $\tau = 400\omega_{pe}^{-1}$ is shown in Figure 3.17(a). This is the finish time for this run. The plot of electron

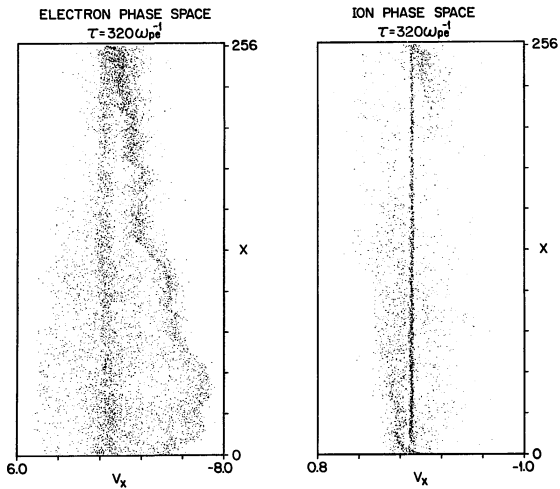


Figure 3.15 (a) Electron phase space at $\tau = 320\omega_{pe}^{-1}$.
(b) Ion phase space at $\tau = 320\omega_{pe}^{-1}$.

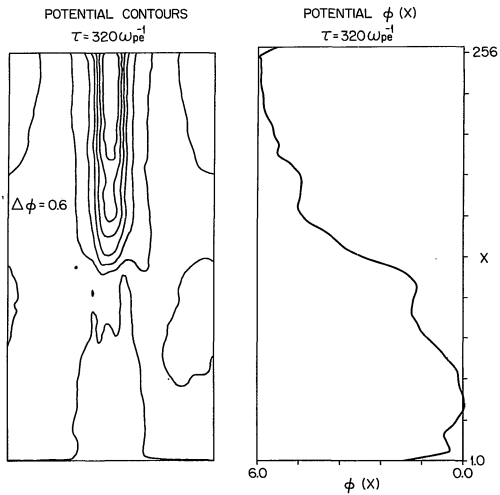


Figure 3.16 (a) Potential contours at $\tau = 320 \omega_{pe}^{-1}$ spaces $\Delta \phi = 0.6 T_e$ apart.
 (b) The potential down the center of the double layer at time $\tau = 320 \omega_{pe}^{-1}$.

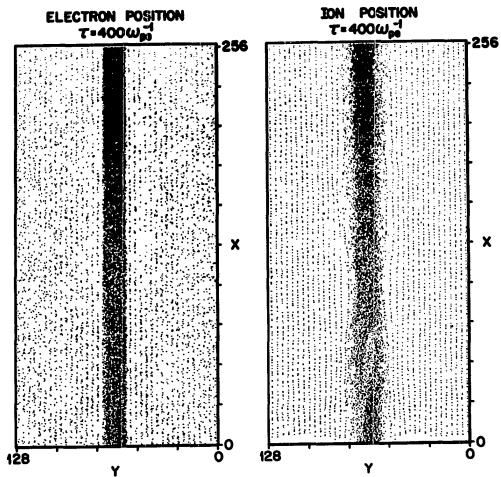


Figure 3.17 (a) Electron positions at the final time $\tau = 400\omega_{pe}^{-1}$.
 (b) Ion positions at the final time $\tau = 400\omega_{pe}^{-1}$.

positions at this time shows uniform distribution of background electrons, and a density gradient of the electron current sheet as it accelerates into the ionosphere. The current sheet remains magnetized having the same thickness as it had initially. The ion positions at this final time are shown in Figure 3.17(b) the background ions also remain roughly uniformly distributed, and density gradient similar to the electrons is also evident. The ion sheet shows some thickening in the lower half of the simulation. It is not clear whether the thickening is to a clump of mirroring plasma sheet ions with corresponding larger gyroradii. It could be due to heating of ionospheric ions in the perpendicular direction, possibly due to ion cyclotron waves. This requires more study.

The electron phase space at $\tau = 400\omega_{pe}$ is shown in Figure 3.18(a). Some Buneman trapping has reappeared but has not grown strong enough to provide significant trapping. The electrons are accelerated into the ionospheric boundary at over six times the initial drift velocity. The heating process on the background electron continues. Figure 3.18(b) shows the ion phase space at this late time, and it shows the classic double layer structure superimposed on the central undisturbed cold ion background. Ionospheric ions are considerably heated as they are accelerated up through the accelerating potential.

The electrostatic potential contours for the simulation at $\tau = 400\omega_{pe}^{-1}$ is shown in Figure 3.19(a), with the contours separated by $\Delta\phi = 0.5T_e$. The cut through the center of sheet in Figure 3.19(b) shows the double layer has moved down toward the ionospheric boundary, and some

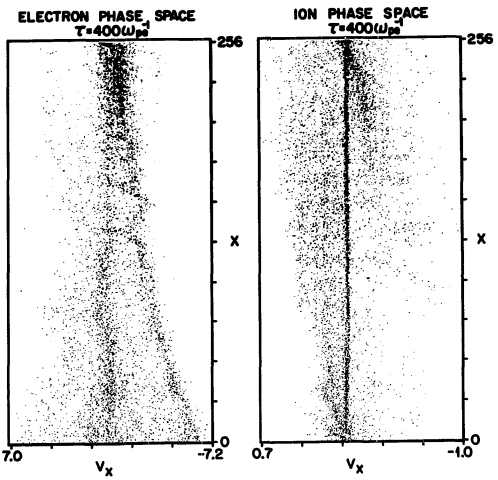


Figure 3.18 (a) The electron phase space at $\tau = 400\omega_{pe}^{-1}$.
 (b) The ion phase space at $\tau = 400\omega_{pe}^{-1}$.

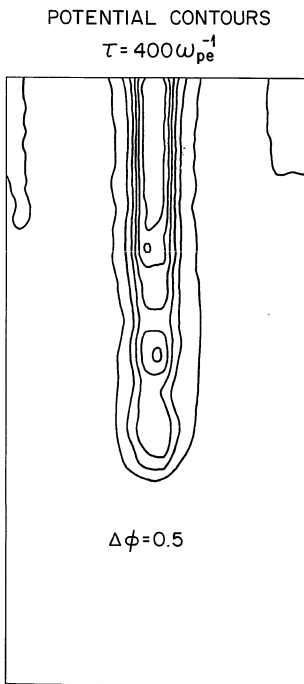


Figure 3.19 (a) Electric potential contours at $\tau = 400\omega_{pe}^{-1}$.

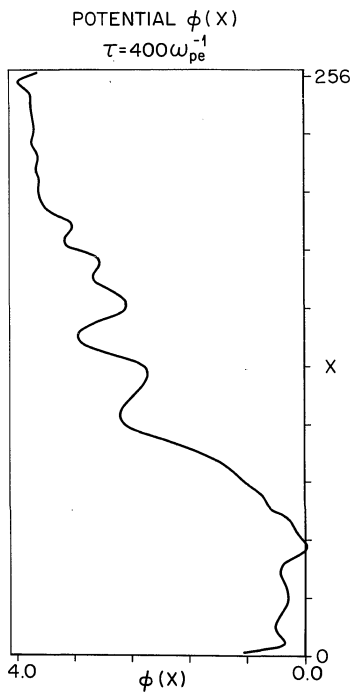


Figure 3.19 (b) The electric potential down the center of the double layer at $\tau = 400\omega_{pe}^{-1}$.

perturbations due to Buneman trapping are also present in the central region. The potential drop, almost equal to the ion kinetic energy, drops from $x = 200 \lambda_{De}$ to $x = 50 \lambda_{De}$, a distance of $150 \lambda_{De}$.

3.3.6 The Evolution of the Velocity Distribution Function in Time

Figure 3.20(a) shows the ion velocity distribution functions $f(v_x)$ vs. v_x for the five different times, $\tau = 40, 120, 200, 320, 400\omega_{pe}^{-1}$ corresponding to phase space and potential contour plots just described. These velocity distribution functions are integrated over space, and include the background plasma. Figure 3.20(b) shows the ions $f(v_y)$ vs. v_y . The central peak, near zero, is due to the background cold ions, while the bottom distribution shows the thermal distribution of the ions which shield the current sheet. Slow heating of the background ions is evident, but the shielding ions show very little change. The perpendicular velocities of the ions are left almost undisturbed during the acceleration process. Strongly excited ion cyclotron waves would have shown some heating, but none is evident from this simulation run.

The similar set of distribution functions for the electrons is shown in Figure 3.21(a). Once again the slow thermalization of the background electrons is evident, but there is no heating of the electron velocities in the perpendicular direction.

Figure 3.21(a) shows the velocity distribution functions for the electron in the parallel direction $f(v_x)$ vs. x . At $\tau = 40\omega_{pe}$ the drifting Maxwellian and the cold background are evident. At later

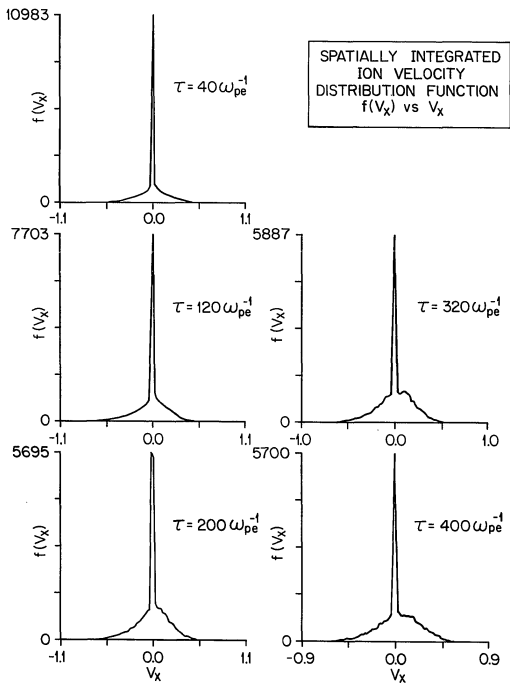


Figure 3.20 (a) Spatially integrated ion velocity distribution $f(v_x)$ vs. v_x function for five different times.

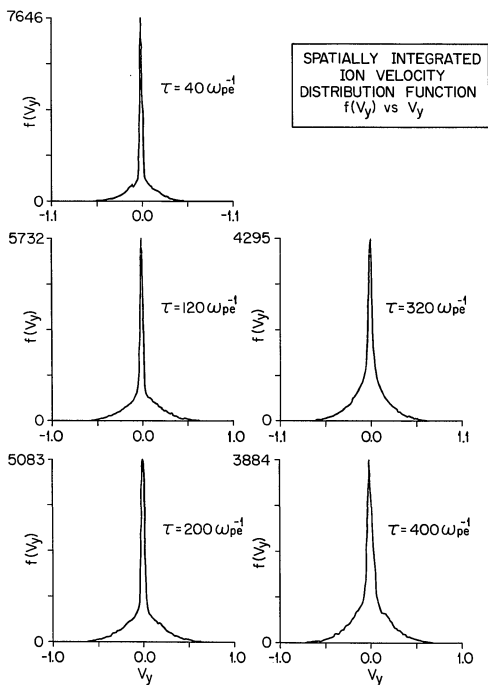


Figure 3.20 (b) Spatially integrated ion velocity distribution functions $f(v_y)$ vs. v_y .

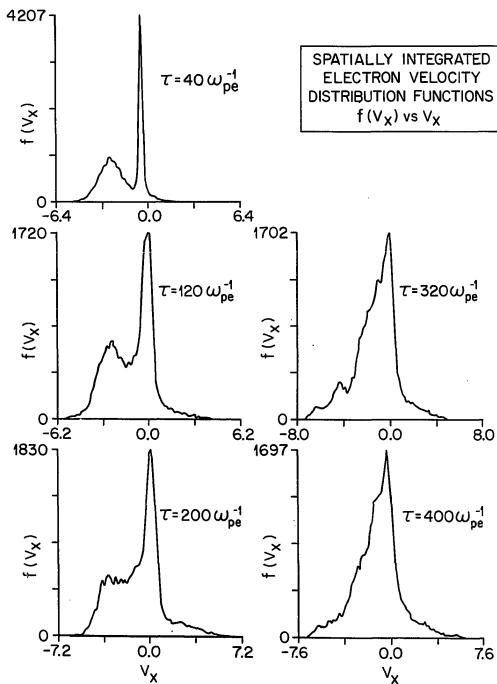


Figure 3.21 (a) The spatially integrated electron velocity distribution functions $f(v_x)$ vs. v_x .

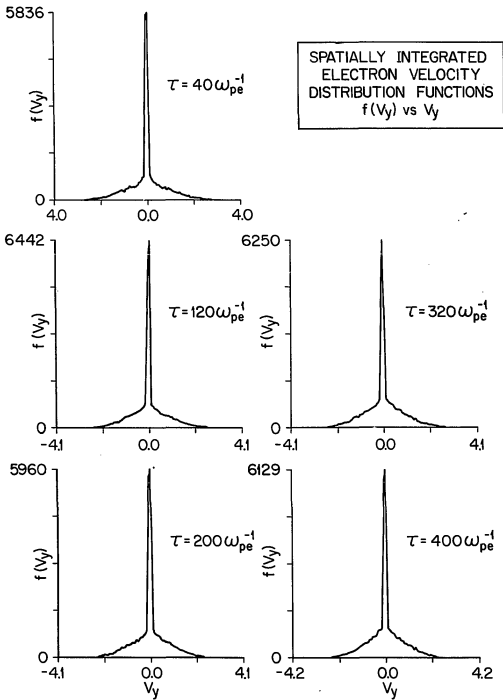


Figure 3.21 (b) The spatially integrated electron velocity distribution functions $f(v_y)$ vs. v_y .

times, heating of the background electrons is seen. The drifting Maxwellian evolves quickly into high energy tails with many trapped electrons filling in the distribution near zero. No change in time is evident.

3.4 Simulation Summary

The simulations described in the previous sections of this chapter show that the acceleration of auroral electrons into the ionosphere is a natural consequence of the interaction of a field-aligned current-carrying electron sheet shielded by ambient ions with a conducting ionosphere. The details of the accelerating potential are a function of the particle sources at the upper and lower boundaries. When the current carrying electrons have a drift speed greater than about one half of their thermal speed, anomalous resistivity effects are important. The anomalous resistivity is identified to be caused by the electron-ion two stream (or Buneman) instability. This instability causes a large amplitude electrostatic wave to grow and trap the current carrying electrons in the wave. This trapping limits the ability of the electrons to carry current. Another type of anomalous resistivity due to current driven ion-cyclotron waves was not seen (see Hudson et al., 1978). This is for two reasons, the first is that the thickness of the electron sheet was less than the average ion gyroradius and therefore, many of the ions were unmagnetized and could not participate in the ion-cyclotron instability. The second reason for the absence of ion-

cyclotron waves in this simulation may be due to the low mass ratio used. The ion-cyclotron instability is mass ratio dependent.

The simulation in a uniform magnetic field demonstrated that in the absence of anomalous resistivity the accelerating potential was concentrated near the lower ionospheric boundary. The simulation with a converging magnetic field showed that this localized double layer became distributed over hundreds of Debye lengths. The reason the double layer becomes distributed in a converging field is shown to be due to the presence of a population of electrons trapped between the dipole mirror and the accelerating potential.

The simulation with the background plasma demonstrates that the background plasma can insulate the distributed double layer from ionospheric boundary. The simulation also shows that background electrons in the near vicinity of current sheet become accelerated along with the current-carrying electrons. There is some indication that the background plasma maybe heated by the leakage of the electric field into the background plasma.

The simulations exhibited a stable V-shaped potential double layer when the particles were handled at the boundaries in the manner described. A time-varying flux of ionospheric ions or current-carrying electrons caused an unstable or oscillating double layer to form.

4.0 Auroral Arc Deformations

Ground based observations of auroral curtain deformations, in particular studies of the distortions known as auroral curls and folds, began with Stormer (1955). From his visual observations he suggested that rayed arcs might actually be thin curtains with many tiny folds viewed from the side. Akasofu and Kimball (1967) published photographs of folded arcs seen in the magnetic zenith which convincingly demonstrated that rayed arcs viewed from the side are actually folded curtains viewed from below.

Problems with lengthy exposure times compared to fast deformation times and the resulting photographic averaging limited further study until Hallinan (1970) and Hallinan and Davis (1970) carefully analyzed their results from TV images and categorized the small scale distortions into classes according to shape, rotational sense, and statistical occurrence.

Parallel to the study of small scale auroral forms the experimental results of Kyhl and Webster (1956), Pierce (1956), Cutler (1956) and Webster and Hallinan (1973) concerning the breakup of hollow and sheet electron beams in vacuum tubes showed a structure remarkably similar to those seen in the aurora, and suggested that the mechanisms producing the distortions are closely related.

Alfvén (1950) was possibly the first to suggest that the folds could be caused by $E \times B$ shear flow arising from a charge sheet within

the aurora. Theoretical analysis of shear flow in crossed field electron beams by Buneman, Levy and Linson (1966) and Levy and Hockney (1968) demonstrated that $E \times B$ shear flow in a magnetically confined electron sheet would lead to the excitation of electrostatic Kelvin-Helmholtz waves, and in some cases the waves would grow nonlinearly and lead to curl-type distortions similar to those observed in the aurora. Levy and Hockney were the first to apply the techniques of plasma simulation to the development of Kelvin-Helmholtz waves in a magnetized electron sheet, and observed that the nonlinear development of the instability was consistent with the experimental vacuum tube observations.

Unfortunately, since the theoretical works and early simulation results were primarily concerned with the deformation of an electron charge sheet in vacuum tubes, it is not obvious that they have direct applicability to the aurora. The primary difference between the auroral environment and the vacuum tube experiments is that quasi-neutrality considerations in the aurora demand that the electron current sheet producing the aurora is imbedded in a neutralizing background of ions. Near the ionosphere the temperature ratio T_e/T_i of the electron sheet and its ion shield is about

$$T_e/T_i \sim 1 \text{ (ionosphere)}. \quad (4.1)$$

The temperature ratio for the plasma originating in the plasma sheet is

$$\frac{T_e}{T_i} \approx 1/5 \text{ (plasma sheet).} \quad (4.2)$$

The electric field perpendicular to the sheet, which is responsible for the zeroth order $E \times B$ shear, is a strong function of the temperature ratio. This is because hot ions make large excursions away from the sheet, setting up the electric field.

The electric field perpendicular to the sheet is not easy to compute theoretically. If the electrons are magnetized to form a charge sheet with half thickness a , the electric field will depend on the density distribution of ions across the sheet. The density distribution in turn, depends on the thickness a , the velocity distribution, and the initial positions of the ions. There are two cases to consider in a time-dependent problem; the first is for an equilibrium situation where the perpendicular electric field is not a function of time, and the second is the nonequilibrium case is when the electric field perpendicular to the sheet changes (oscillates) with time. The equilibrium case has been studied by Albano et al. (1979). Since the spatial distribution of ions across the sheet may be due to properties of the current source or to anomalous diffusion across the magnetic fields by current driven instabilities, there is no reason to expect that the auroral current sheet be in exact equilibrium.

Since it was computationally and economically unfeasible to begin the following simulation with an equilibrium profile for the ions, an alternative had to be chosen. Experimentation with many simulations

showed that an initial guiding center placement, i.e., magnetized ions, worked well and is inexpensive. The use of initial guiding center placement for the ions has several advantages, with simplicity already mentioned. Another advantage is that it greatly simplifies an estimation of the electric field at $t = 0$, a quantity that is necessary so that the unstable modes of deformation can be computed theoretically. The simulation shows that this initial placement of the ions causes damped oscillations of the ions perpendicular to the sheet at a frequency approximately equal to the ion plasma frequency. Oscillations at the ion cyclotron frequency were also observed. These oscillations damped out after several thousand ω_{pe}^{-1} , depending on the initial ion temperature and the sheet thickness. The coupling of these oscillations to the unstable Kelvin-Helmholtz waves appears to be minor.

It is possible to estimate the zeroth-order perpendicular field arising from the ion shielding by a simple model. Assume the electron sheet has a half-thickness a and density n_e . The ions, if we assume for the sake of simplicity that they are monoenergetic, must occupy a sheet having a half-thickness b given by

$$b = a + \rho_i \quad , \quad (4.3)$$

where ρ_i is the ion gyroradius. Quasi-neutrality demands

$$n_e a = n_i (a + \rho_i) \quad , \quad (4.4)$$

the maximum electric field occurs at the edge of the electron sheet, and is given by (from Gauss' Law)

$$E(a) = \left(\frac{\rho_i}{a + \rho_i} \right) a n_e \quad \left(\begin{array}{c} \text{shielded} \\ \text{by ions} \end{array} \right) \quad (4.5)$$

The factor $\rho_i / (a + \rho_i)$ is always less than 1 so that $E(a)$ is always less than the unshielded value,

$$E(a) = a n_e \quad \left(\begin{array}{c} \text{not shielded} \\ \text{by ions} \end{array} \right) \quad (4.6)$$

We can explicitly include the ion temperature if we assume the ions are monoenergetic, in which case we have

$$\rho_i = \frac{m_i v_i}{q B} = \frac{m_i (kT_i/m_i)^{1/2}}{q B} \quad (4.7)$$

and substitute (4.7) into (4.5).

Having shown that the presence of shielding ions around the electron sheet controls the zeroth order electric field perpendicular to the sheet, it remains to be shown how electrostatic Kelvin-Helmholtz waves are affected by the thermal ion background. It is easy to see that the electric field is always less than an unshielded case. As a result, the zeroth order drift of the electrons,

$$v_D = \frac{E \times R}{B^2} \quad (4.8)$$

will be less too.

Consider a charge sheet having a half width a , magnetized by a uniform magnetic field in the z -direction B , and shielded by a background of monoenergetic ions having a thermal velocity V_{th} . The ions therefore have a gyroradius ρ_i given by

$$\rho_i = \frac{m_i V_{th}}{qB} \quad (4.9)$$

Since the ion guiding centers lie on top of the electron guiding centers, the electron and charge distributions form profiles given approximately by (in this case the ions are magnetized)

$$n_i(y) = \begin{cases} n_{i0}, & |y| < a + \rho_i \\ 0, & |y| > a + \rho_i \end{cases} \quad (4.10)$$

and

$$n_e(y) = \begin{cases} n_{e0}, & |y| < a \\ 0, & |y| > a \end{cases} \quad (4.11)$$

where $n_{i0} = a/(a + \rho_i)n_{e0}$, and $\rho_i = m_i V_{th}/q B_z$ is the mean ion gyroradius with m_i the ion mass, q the electron charge, B_z the magnetic

field, V_{th} the ion thermal velocity, and n_{e0} and n_{i0} are constant electron and ion number densities, respectively. This allows us to estimate the charge separation Δ , defined to be one minus the ratio n_{i0}/n_{e0} . In this case $\Delta = 1 - a/(a + \rho_i)$. Notice $\Delta = 1$ reduces to the case with no ion shielding while $\Delta = 0$ indicates perfect shielding and hence no electric field.

A simple application of Gauss' Law yields the zeroth order electric field from the density profile;

$$E_o(x) = \begin{cases} (n_i - n_e)x & x < a \\ (n_i - n_e)a + n_i(x - a) & x \geq a \end{cases} \quad (4.12)$$

In addition, charge neutrality demands

$$n_e a = n_i (\rho_i + a) \quad , \quad (4.13)$$

so that

$$n_e = \left(\frac{\rho_i}{\rho_i + a} \right) n_i \quad . \quad (4.14)$$

Then $E(x)$ becomes

$$E(x) = \begin{cases} n_i \left(1 - \frac{\rho_i}{\rho_i + a}\right) x & x < a \\ n_i (a - \rho_i) + n_i (x - a) & x \geq a \end{cases} \quad (4.15)$$

$E(x)$ is zero at $x = 0$ and $x = a + \rho_i$. $E(x)$ is a minimum, but largest in absolute value, at $x = a$ where it takes on a value of $E(a) = n_i (a - \rho_i)$. In order to compute the dispersion relationship, it is possible to extend the development of Runeman, Levey and Linson (1966). Assume $E(x)$ can be expanded into its zeroth order plus perturbation,

$$E = E_0 + E_1 \quad (4.16)$$

The corresponding potential is given by

$$\phi = \phi_0 + \phi_1 \quad (4.17)$$

Assume the perturbation is of the form

$$\phi_1 = \begin{cases} A e^{-kx} e^{i(ky - \omega t)} & x > a \\ (B e^{-kx} + C e^{kx}) e^{i(ky - \omega t)} & -a < x < a \\ D e^{kx} e^{i(ky - \omega t)} & x < -a \end{cases} \quad (4.18)$$

Using this formulation, it is possible to compute E_x and E_y , the x and y component of the electric field respectively,

$$E_{x1} = \begin{cases} -kA e^{-kx} e^{i(ky - \omega t)} & x > a \\ (-kBe^{-kx} + cke^{kx}) e^{i(ky - \omega t)} & x < a \\ kDe^{kx} e^{i(ky - \omega t)} & x < -a \end{cases} \quad (4.19)$$

The boundary conditions to be applied at the edge of the electron charge sheet at $x = \pm a$ are; first the tangential electric field $E_y = -\frac{\partial \phi_1}{\partial y}$ is continuous across the boundary, and second; the normal electric field is discontinuous by an amount equal to the surface charge density induced by the wave:

$$\begin{aligned} \frac{\partial \phi_1}{\partial y} \Big|_{x+a^+} - \frac{\partial \phi_1}{\partial y} \Big|_{x+a^-} &= 0 ; \quad \frac{\partial \phi_1}{\partial y} \Big|_{x+a^+} \Big|_{x+a^-} = 0 \\ \text{and} \quad \frac{\partial \phi_1}{\partial x} \Big|_{x+a^+} - \frac{\partial \phi_1}{\partial x} \Big|_{x+a^-} &= -\frac{\sigma(a)}{\epsilon_0} \\ \frac{\partial \phi_1}{\partial x} \Big|_{x-a^+} - \frac{\partial \phi_1}{\partial x} \Big|_{x-a^-} &= -\frac{\sigma(-a)}{\epsilon_0} \end{aligned} \quad (4.20)$$

The charge density can be derived from the continuity equation

$$\frac{\partial n_1}{\partial t} = \nabla \cdot (n_1 \underline{v}_0 + n_0 \underline{v}_1) = 0 \quad (4.21)$$

Recall the subscript "o" refers to zeroth order quantities and the subscript "1" refers to 1st order perturbations. The perturbed velocity is related to the perturbed electric field by

$$\underline{v}_1 = \frac{\underline{E}_1 \times \underline{B}_0}{B_0} \quad (4.22)$$

Since we are considering only electrostatic perturbations, $\nabla \times \underline{E}_1 = 0$. Hence, $\nabla \times \underline{v}_1 = 0$, and the continuity equation becomes (using the identity $\nabla(\underline{A} \times \underline{B}) = \underline{B} \times (\nabla \times \underline{A}) - \underline{A} \times (\nabla \times \underline{B})$)

$$\frac{\partial n_1}{\partial t} + v_0 \cdot \nabla n_1 = -v_1 \cdot \nabla n_0 \quad ,$$

so that by using the formula for v_1 we get

$$n_1(\pm a) = -\frac{k\phi_1}{\omega - kv_0} \frac{1}{B_0} \frac{\partial n_0}{\partial x} \quad (4.23)$$

The surface charge density is just the integral over the perturbed number density

$$\sigma(a) = \int_a^{a^+} n_1(a) dx$$

$$\sigma(-a) = \int_{-a}^{-a^+} n_1(-a) dx ,$$
(4.24)

which becomes

$$\sigma(\pm a) = \pm \frac{en_0}{B_0} \frac{k\phi_1}{\omega \mp kv_0} ,$$
(4.25)

and the dispersion relation can then be derived using this charge density in the formula for the boundary conditions, giving

$$\left(\frac{\omega}{\omega_0}\right)^2 - \frac{1}{4} \left(1 - \frac{2kv_0}{\omega_0}\right)^2 + \frac{1}{4} e^{-4ka} = 0 .$$
(4.26)

If we define $\Delta = 1 - \frac{a}{a + \rho_1}$, and use this expression in the zeroth order electric field, and the resulting zeroth order drift velocity, we get to a final dispersion relationship

$$\left(\frac{\omega}{\omega_0}\right)^2 - \frac{1}{4} (1 - 4ka\Delta + 4k^2 a^2 \Delta^2) + \frac{1}{4} e^{-4ka} = 0$$
(4.27)

with

$$\omega_0 = \omega_{pe}^2 / \omega_{ce} .$$

This gives the classical result (Hasegawa, 1975) for $\Delta = 0$ which is complete charge separation, or the unshielded case. The imaginary part of ω , the wave frequency, has been plotted in Figure 4.1 for the various values of Δ . The important features of this dispersion relation are

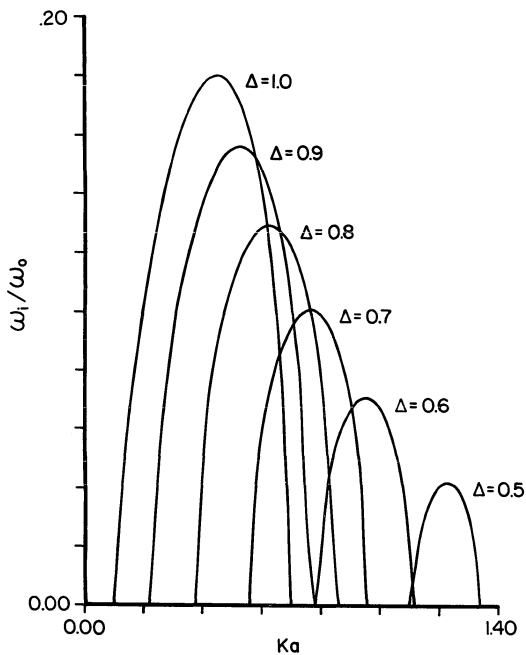


Figure 4.1 The dispersion relationship for Kelvin-Helmholtz waves in an ion-shielded electron charge sheet.

that: 1) the highest growth rates occur for largest values of charge separation, and 2) the most unstable wave number k_{\max} , which is given by the peak of each curve, is an increasing function of the charge separation. This means a tendency towards shorter wavelengths and smaller vortices for increased shielding.

The following simulations suggest a criteria that can be used to determine whether folds or curls will form. When $\rho_i > a$ the charge separation is large and the deformations scale size is much less than the thickness of the ion sheath. In this case curls will form. When $\rho_i \lesssim a$ the charge separation is small and the deformation scale size is larger or approximately equal to the sheath thickness. In this case folds will occur.

4.1 Auroral Curl Simulation

With this model in mind, a two-dimensional electrostatic particle algorithm is used to simulate the time development of the resulting charge sheet deformations. The electrons are pushed using the guiding center approximation, while the full dynamics of the ions are followed (Lee and Okuda, 1976). This is different from most previous simulations, but is an important approximation because it allows us to use realistic plasma parameters, particularly the realistic mass ratio (m_e/m_i) and magnetic field (B_z).

We use a two-dimensional computational mesh size $N_x \times N_y = 64 \times 128$. The grid spacing used was $\Delta = 1/3 \lambda_{De}$ where λ_{De} is the electron Debye length. The mass ratio $m_e/m_i = 1/1837$ was used. The electrons

and ions are assumed to be finite sized charge clouds having a radius $a_x = a_y = \Delta$. We assume an initial sheet half thickness $a = 3 \lambda_{De}$, a temperature ratio $T_e/T_i = 0.6$, and a magnetic field which gives an electron plasma to electron cyclotron frequency of $\omega_{pe}/\omega_{ce} = 1/20$. The simulation was run using a time step of $1\omega_{pe}^{-1}$ for 5000 steps, or until $5000\omega_{pe}^{-1}$. This was sufficient time for the deformations to form, saturate, and diffuse to the boundaries of the simulation grid. Periodic boundary conditions were assumed.

This choice of parameters corresponds to conditions at roughly a 2-3 R_E altitude. Note that at lower altitudes we might expect cooler ions ($T_e/T_i = 1$ in the ionosphere) and higher magnetic fields, while at higher altitudes we expect hot ions ($T_e/T_i \approx .2$ in the plasma sheet) and a lower magnetic field. By finding the plasma parameters which closely match the visual observations it is possible to discover the environment and altitude in which the instability occurred.

Figure 4.2 shows the positions of the electron guiding centers. Figure 4.3 shows the positions of the ions. The ion guiding centers lie on top of the electrons, but the ions occupy a larger area due to larger gyroradii. The potential contours perpendicular to the sheet are shown in Figure 4.4.

The linearly unstable phase of the distortions is evident in Figures 4.2(b) and 4.2(b) at $\tau = 250\omega_{pe}^{-1}$. The electric potential contours at this time show a potential drop of $\Delta\phi = 2.9 (T_e\Delta\lambda_{De}^{-1})$ between contour lines. The total potential drop on each side of the sheet is about $1.6T_e$. This corresponds well to the ion kinetic energy

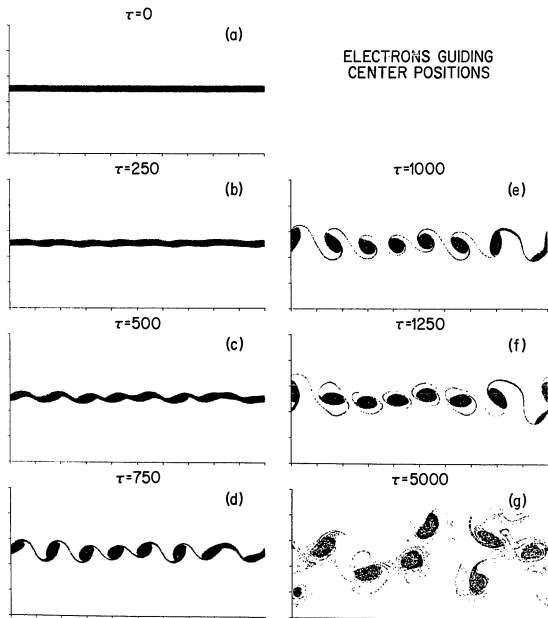


Figure 4.2 The electron guiding center positions as a function of time illustrating the formation of auroral curls.

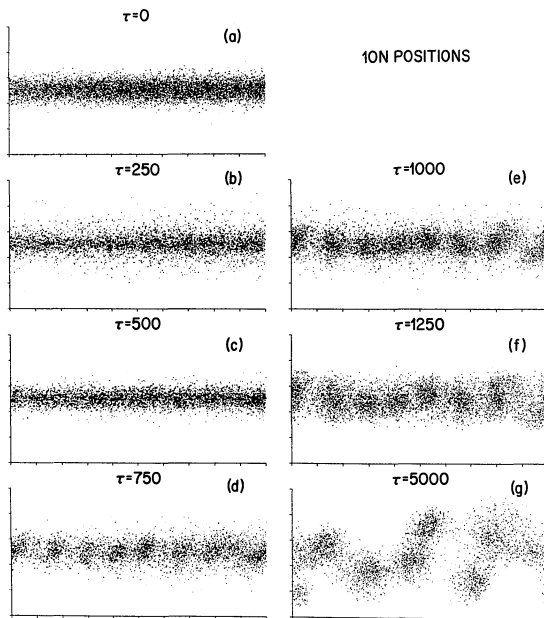


Figure 4.3 The ion positions as a function of time as they try to shield the electric field of the deforming electron sheet.

which is about $1.5T_e$. The simulation shows that the most unstable mode is $m = 8$. The integer m counts the number of eddies that will form in the simulation. Since $\rho_i \approx 11 \lambda_{De}$ and $a = 3 \lambda_{De}$ we have a charge separation of 0.8, and a predicted unstable mode number $ka \approx 0.6$, obtained from the theoretical result in Figure 4.1, or $\frac{2\pi ma}{L_x} = 0.6$, which corresponds to mode 8 in agreement with the simulation (periodic boundary conditions in the simulation require integral mode numbers). In general, our results illustrate that the assumption that the ions produce the electric potential profile and the electrons respond to it, is good as long as $\rho_i \gg a$ and the ions appear almost unmagnetized in the later stages of the simulation. If $\rho_i \approx a$ our results show that curl formation is limited and that a different deformation, one known as an auroral fold occurs, this will be described more fully in the next section.

Figure 4.4 is a sequence of plot of the electric field potential contours for the simulation at the successive times used for the previous plots of the electron and ion positions. At the early time $\tau = 250\omega_{pe}^{-1}$ the contours are horizontal indicating the electric field is perpendicular to the undisturbed electron sheet. At later times, for example at $\tau = 1000\omega_{pe}^{-1}$, the contours form islands around the deforming eddies, or curls, so that each curl is surrounded by an almost radial electric field. Figure 4.5 shows a T.V. picture of auroral curl formation and can be compared to this simulation.

Figure 4.6 is a time history of the ion kinetic energy and electrostatic energy as a function of time. The oscillation of the ion

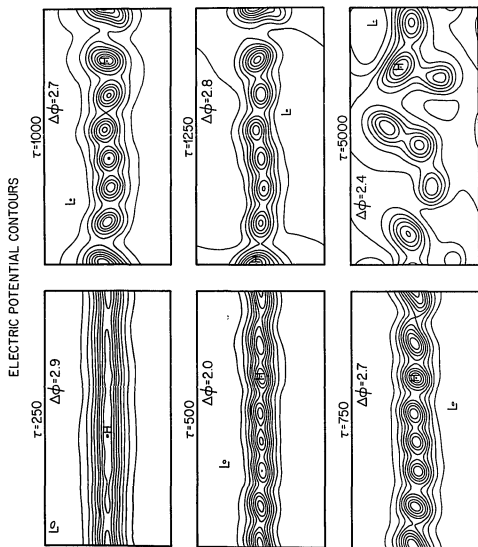


Figure 4.4 The electric potential contours at various times during the formation of auroral curls.

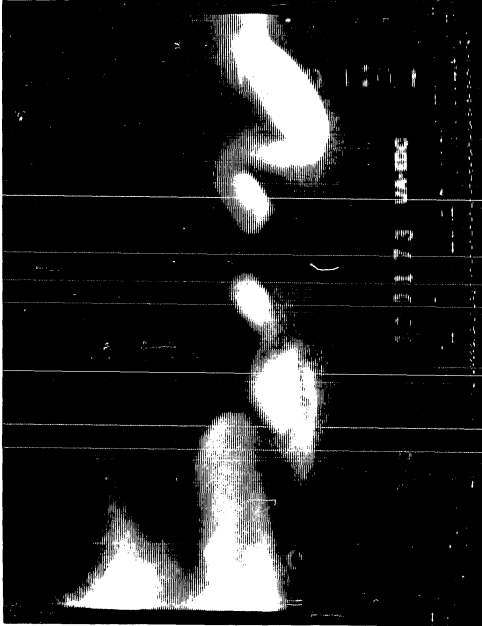


Figure 4.5 A T.V. picture of auroral curl formation.

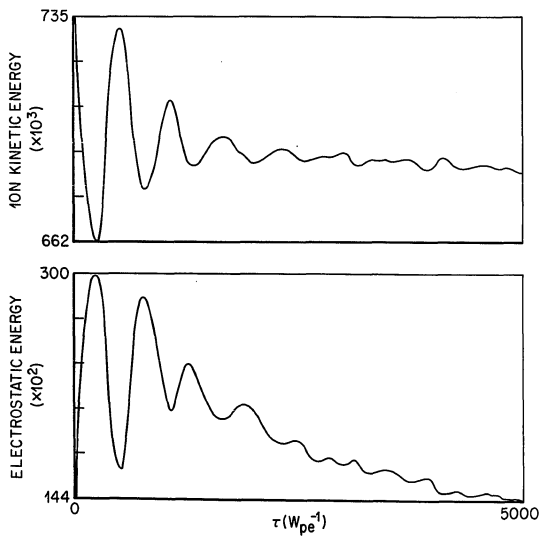


Figure 4.6 Time history of the ion kinetic energy and the total electrostatic energy for the auroral curl simulation.

kinetic energy is at the ion plasma frequency. These oscillations occur because the initial configuration of the ions is not in equilibrium. These oscillations also cause oscillations in the electric field, and this is seen in the plot. The oscillations are out of phase because the electrostatic energy is a maximum when the ions are farthest from the sheet (ion plasma oscillations perpendicular to the sheet). The oscillations eventually damp out and the electric field energy returns to its initial value.

Figure 4.7 shows the spatially integrated velocity distribution function for both ions and electrons at an early time, $\tau = 250\omega_{pe}^{-1}$. The electron velocity distribution function in the x-direction is almost flat, a result of the velocity shear of the electron guiding center. The electron velocity distribution for $f(v_y)$ does not have the same scale, and indicates that the velocities perpendicular to the sheet are small compared to the shear velocities. The ions show undisturbed Maxwellian distributions.

Figure 4.8 shows the spatially integrated velocity distribution function at a late time, $\tau = 5000\omega_{pe}^{-1}$. The ion velocity distribution functions are tending towards a thermal distribution. The ion velocities have not been effected by the instability.

4.2 Auroral Fold Simulation

The two-dimensional particle algorithm described earlier is used to simulate the time development of the resulting charge sheet deformations is known as auroral folds. The electrons are pushed using the guiding

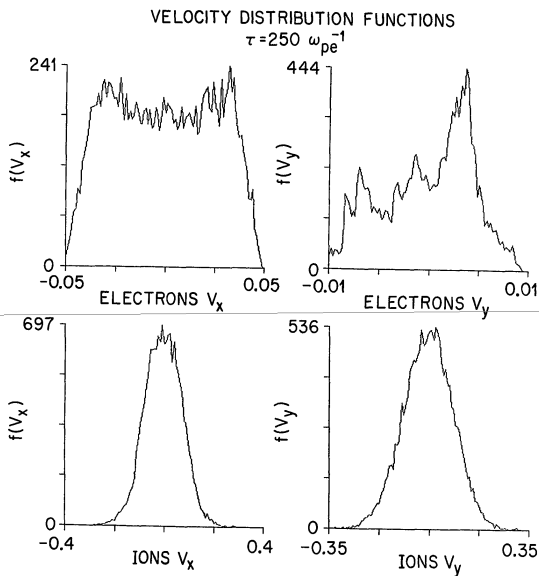


Figure 4.7 The spatially integrated velocity distribution functions for ions and electrons at time $\tau = 250 \omega_{pe}^{-1}$.

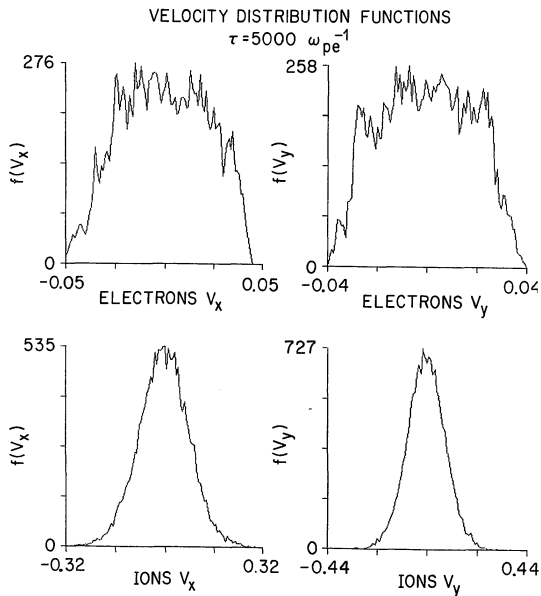


Figure 4.8 The spatially integrated velocity distribution function for ions and electrons at time $\tau = 5000 \omega_{pe}^{-1}$.

center approximation, while the full dynamics of the ions are followed. This is different from most previous simulations, but is an important approximation because it allows us to use realistic plasma parameters, particularly the correct mass ratio (m_e/m_i) and magnetic field (B_z). This simulation is also described in Wagner et al. (1981).

We use a two-dimensional computational grid having $N_x \times N_y = 64 \times 128$. The grid spacing Δ was used $\nabla = 1/5 \lambda_{De}$ where λ_{De} is the electron debye length. The correct mass ratio $m_e/m_i = 1/1837$ was used. The electrons and ions are assumed to be finite sized charge clouds having a radius $a_x = a_y \Delta$. We assume an initial sheet half thickness $a = \lambda_{De}$, a temperature ratio $T_e/T_i = 0.4$, and a magnetic field which gives an electron plasma to electron cyclotron frequency of $\omega_{pe}/\omega_{ce} = 1/75$. The simulation was run using a time step of $1\omega_{pe}$ for 10000 steps, or until $10000\omega_{pe}^{-1}$. This was sufficient time for the deformations to form, saturate, and diffuse to the boundaries of the simulation grid. Periodic boundary conditions were assumed.

This choice of parameters correspond to conditions at roughly a 3 R_E altitude. Note that at lower altitudes we might expect cooler ions ($T_e/T_i = 1$ in the ionosphere) and higher magnetic fields, while at higher altitudes we expect hot ions ($T_e/T_i \approx .2$ in the plasma sheet) and a lower magnetic field. By finding the plasma parameters which closely match the visual observations it is possible to discover the environment and latitude in which the instability occurred.

Figure 4.9 shows the positions of the electron guiding centers. Figure 4.10 shows the positions of the ions. The ion guiding centers

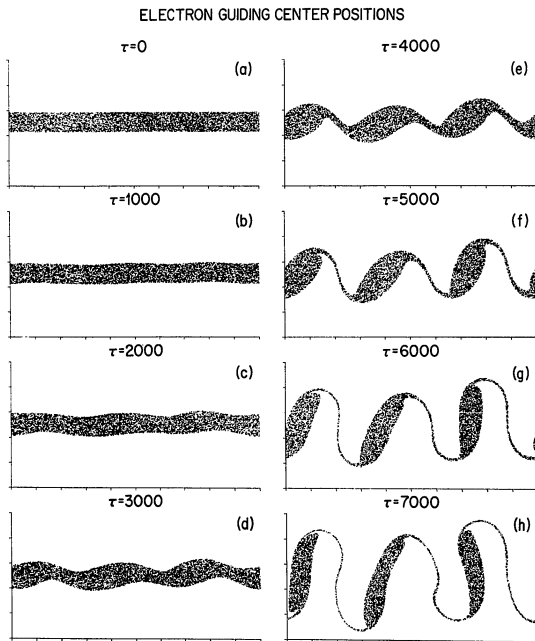


Figure 4.9 The position of the electron guiding centers at various times showing the formation of auroral curls.

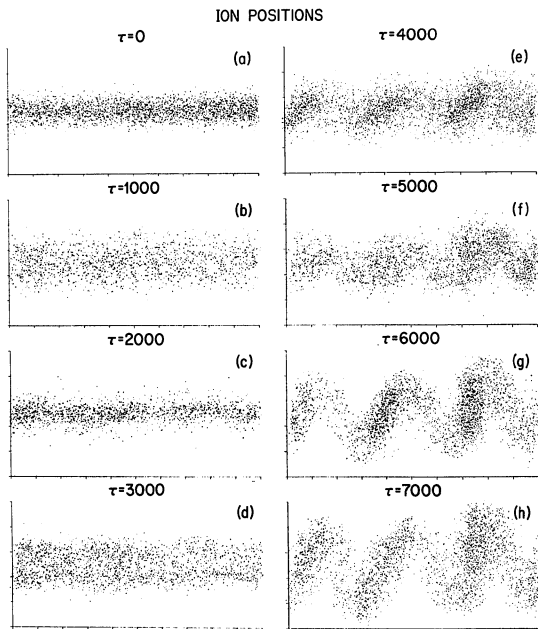


Figure 4.10 The ion position at various times as they try to shield the electric field of the distorting electric sheet.

lie on top of the electrons, but the ions occupy a larger area due to their larger gyroradii. The electric potential contours are shown in Figure 4.11.

The linear phase of the distortions is evident in Figures 4.9(b) and 4.10(b) at $\tau = 1000\omega_{pe}^{-1}$. The electric potential contours at this time show a potential drop of $\Delta\phi = 1.9 (T_e\Delta\lambda_{pe}^{-1})$ in between contour lines. The total drop on each side of the sheet is about $2.8T_e$. This corresponds well to the ion kinetic energy which is about $2.5T_e$ (since $T_e/T_i = 0.4$). By $\tau = 3000\omega_{pe}^{-1}$, the deformations have progressed to a point where it is clear that the most unstable mode is $n = 3$. In contrast, the linear unshielded theory predicts $n = 2$ for this case. The discrepancy is accounted for in the dispersion relationship. To verify this, we compute the charge separation, Δ . For this simulation we have $a = 5$, $\rho_i = 10$, and therefore $\Delta = 0.7$. From Figure 4.1 this value of charge separation predicts the most unstable wavenumber to be $k = 0.75$. Since $k = 2\pi na/L_x$, and recalling $L_x = 128\lambda_{pe}$, we get mode $n = 3$, in excellent agreement with the simulation.

From Figure 4.9, using $\Delta = 0.7$, it is clear that the most unstable mode has a growth rate of about $0.10 \omega_0$. Since $\omega_0 = \omega_{pe}^2/\omega_e$, the value of ω_0 for this simulation is $\omega_0 = 0.013$, and we then expect a growth rate of about $1.3 \times 10^{-3}\omega_{pe}$. This gives an e-folding time of about ω_{pe}^{-1} , in agreement with the simulation.

Notice the deformation proceeds as predicted by the typical Kelvin-Helmholtz theory, similar to the development of auroral curls (which "wind up") until $\tau = 6000\omega_{pe}^{-1}$. At this point the formation of vortices

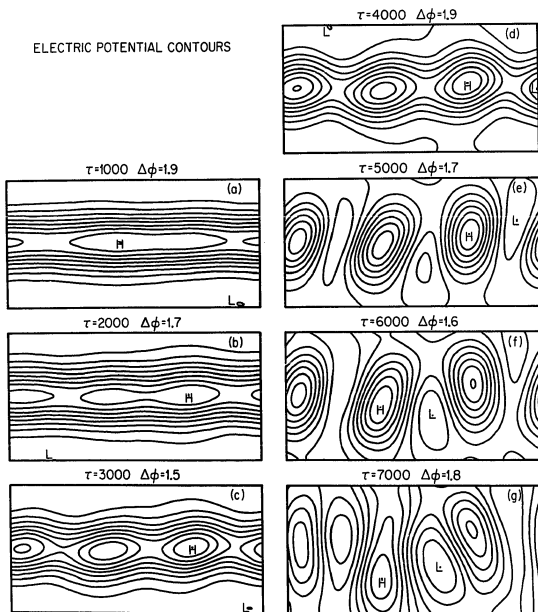


Figure 4.11 Electrostatic potential contours for the auroral fold simulation at various times during the simulation.

is limited, and the electron clumps begin to flatten and elongate. The reason for this change can be seen from the ion positions in Figure 4.10. The potential contours are shown in Figure 4.11. The ion guiding centers lag behind the electron guiding centers. Due to this, regions of positive space charge form on the inside radius of the curvature of the deforming sheet and on the trailing arms of the deforming eddies. The electric field due to this small space charge causes an $E \times B$ drift in addition to the zeroth order drift, and this additional drift can be seen to elongate the vortices and cause the thin connecting arms of the vortices to hook around the positive charge centers. This is clearly seen in Figure 4.10(h). In general, the space charge does not accumulate if $\rho_i > \lambda$, where λ is the wavelength of the deformation, indicating that when $\rho_i > \lambda$ curls form, not folds. Other simulations show that the elongated vortices which stretch to become folds continue to filamentate and form thin strands which are themselves susceptible to the shear instability. The strands are thinner than the original sheet, and ultimately become thin enough for $\rho_i > \lambda$, in which case quasi-stable curls form and persist for very long times.

The velocity distribution functions for the electron guiding center and for the ion are shown at an early time, $\tau = 1000\omega_{pe}^{-1}$, in Figure 4.12, and a late time $\tau = 7000\omega_{pe}^{-1}$ in Figure 4.13. In Figure 4.12 the shear is clearly seen in the x-velocity distribution of the electron guiding centers. The maximum shear velocity occurs very near the edge of the electron charge sheet. The small electron velocities in the y-direction are consistent with the fact that E_x is very small during the early

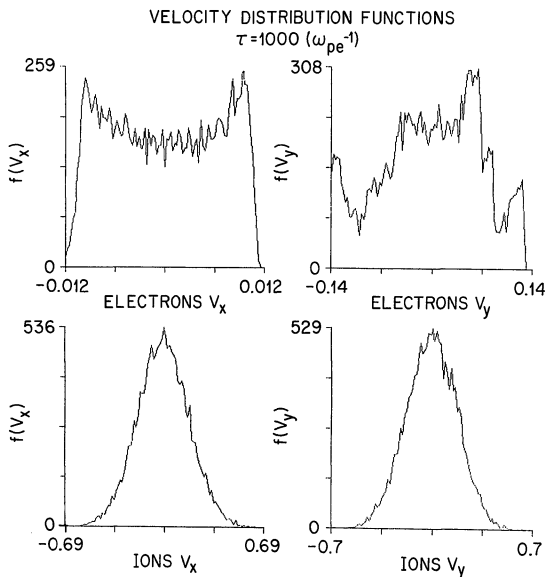


Figure 4.12 Spatially integrals velocity distribution functions for electrons and ions at time $\tau = 1000\omega_{pe}^{-1}$ for the auroral fold simulation.

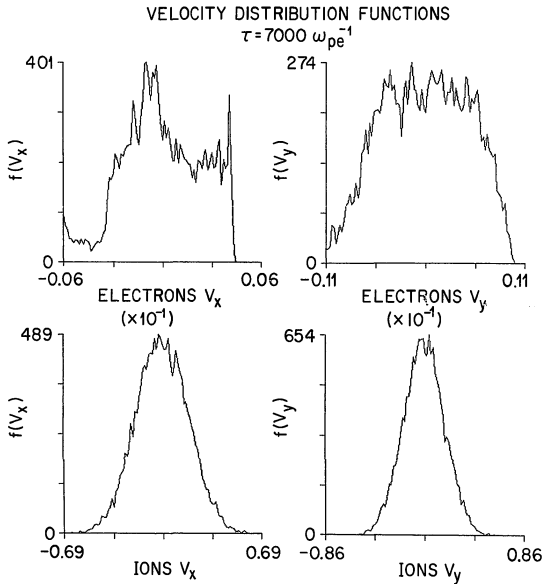


Figure 4.13 Spatially integrated velocity distribution functions of electrons and ions at time $\tau = 7000 \omega_{pe}^{-1}$ for the auroral fold simulation.

stages of development, and the velocities of the electrons in the y -direction are just random fluctuations. At this same time, the ions show a Maxwellian velocity distribution due to their finite temperature. The maximum $E \times B$ shear speed is much less than the ion thermal speed and therefore not observed in the ion profile. In Figure 4.13, at the later time $\tau = 7000\omega_{pe}^{-1}$, the vortices have rotated and are aligned in the y -direction. For this reason the distribution of electron guiding center velocities in the x -direction are small and random, while the y -direction $f(v_y)$ is flat showing considerable shear. The ion velocity distributions are essentially unchanged, indicating the developing folds leave the ions undisturbed in velocity space, with no heating or cooling taking place.

When $\rho_i \approx a$, folds (not curls) occur because the ions tend to shield the electrons much more closely, but lag behind them spatially as the deformation proceeds in time. This causes the deformations to grow with an additional perturbing electric field which inhibits vortex twisting. As a result the vortices elongate into thin bars or folds. These thin folds, which thin as they elongate, maintain a constant density and eventually become long enough (one or more wavelengths) to be once again unstable against Kelvin-Helmholtz waves (see Figure 4.14). Thus "curl type" instabilities will be superposed on the folds. An example of auroral folds unstable to further "curl-type" instabilities is shown in Figure 4.14. In this simulation $N_x \times N_y = 256 \times 128$, $T_e/T_i = 0.6$, $\omega_{ce}/\omega_{pe} = 75$, sheet width $6 \lambda_{De}$, and $\Delta(\text{grid size}) = 1/3 \lambda_{De}$. The electron guiding center position, ion positions, and

ELECTRON GUIDING CENTERS

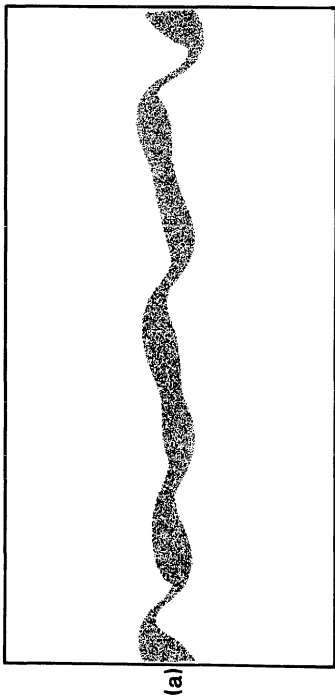


Figure 4.14 (a) Electron guiding centers at time $t = 1500\omega_{pe}^{-1}$.

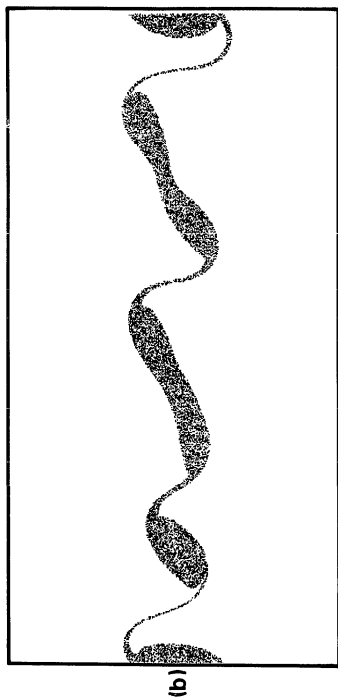


Figure 4.14 (b) Electron guiding centers at time $\tau = 2000\omega_{pe}^{-1}$.

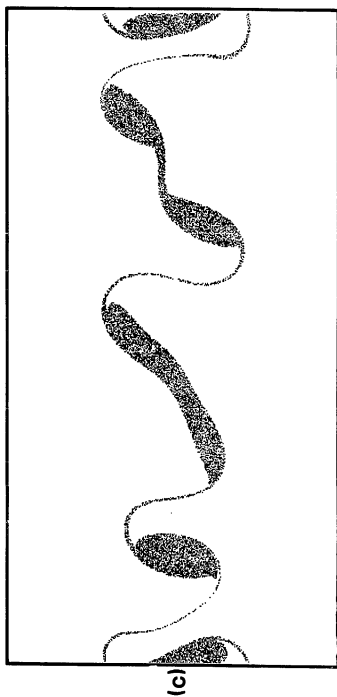


Figure 4.14 (c) Electron guiding centers at time $\tau = 2500\omega_{pe}^{-1}$.

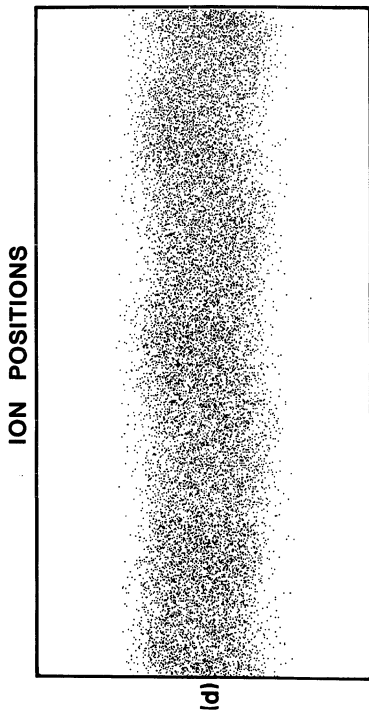


Figure 4.14 (d) Ion positions at time $\tau = 15000\omega_{pe}^{-1}$.

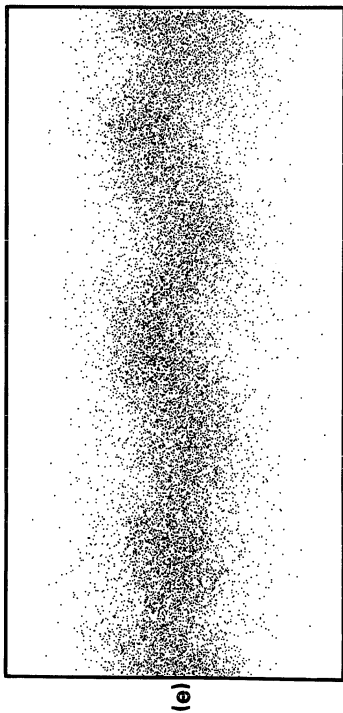


Figure 4.14 (e) Ion positions at time $\tau = 2000\omega_{pe}^{-1}$.

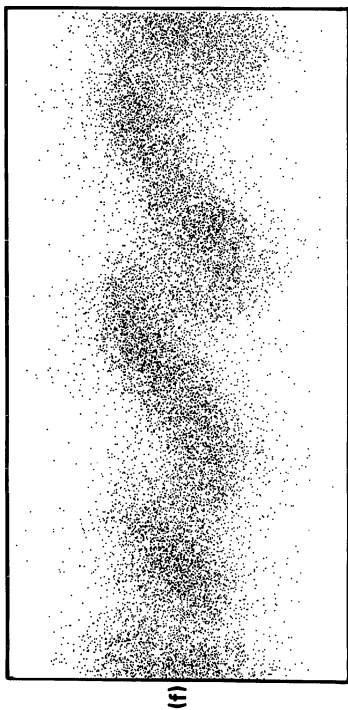


Figure 4.14 (f) Ion positions at time $\tau = 2500\omega_{pe}^{-1}$.

POTENTIAL CONTOURS

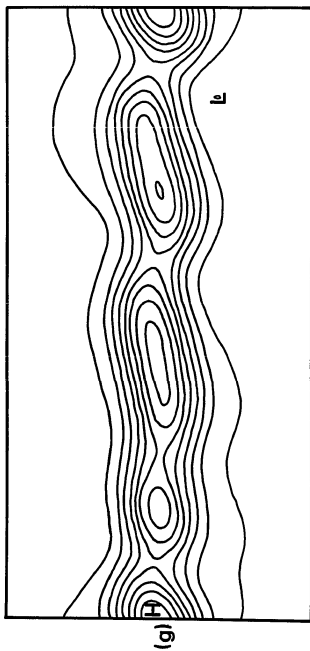


Figure 4.14 (g) Equipotential contours at time $\tau = 1500 \omega_{pe}^{-1}$.

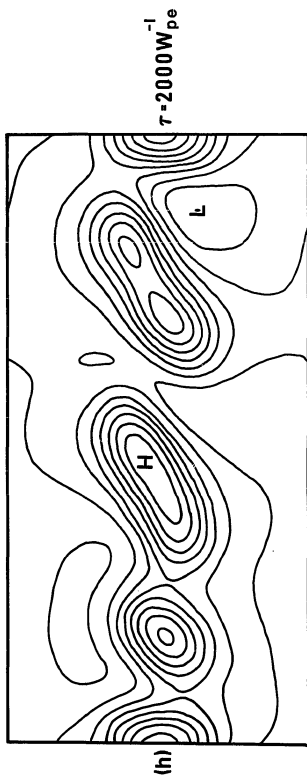


Figure 4.14 (h) Equipotential contours at time $\tau = 2000 \omega_{pe}^{-1}$.

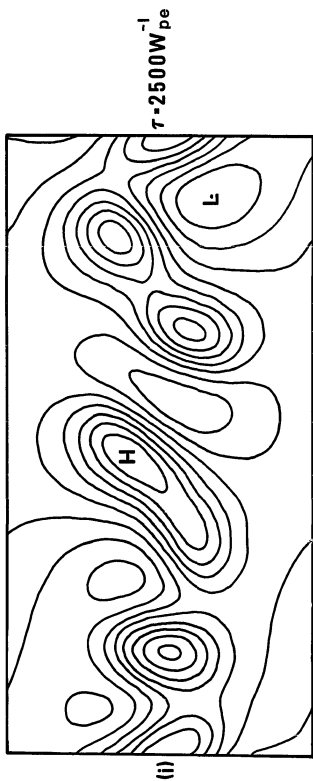


Figure 4.14 (1) Equipotential contours at time $\tau = 2500 \omega_{pe}^{-1}$.

potential contours are shown at three successive times, $1500\omega_{pe}^{-1}$, $2000\omega_{pe}^{-1}$, and $2500\omega_{pe}^{-1}$. This process continues until the sheet is thin enough for $\rho_i \gg a$, when quasi-stable curls form. This is in agreement with the observational fact that curls are observed more frequently than folds, and folds are often seen to evolve into curls, not vice-versa. Hence, our results show that curls and folds are caused by the same process, the difference being the degree to which the ions interact with the deforming electron sheet, a process which is dependent on the ion gyroradius to electron sheet thickness ratio ρ_i/a .

5.0 Conclusion

This conclusion is broken into two parts. In the first part a summary of the work done is given. Final results are given in the first section describing their importance. In the second part suggestions for future work in the area of auroral arc formation is given.

5.1 Summary of Work Done

This thesis describes, collectively, a series of simulations which attempt to model the formation of an auroral arc. The simulations are divided into two groups. The first group is a set of simulations describing the temporal evolution of the accelerating potential structure that develops above the ionosphere and energizes auroral electrons. The second group of simulations model the auroral arc in a plane parallel to the ionosphere, so that the small-scale deformations known as auroral curls and folds can be studied.

In order to simulate auroral arc formation, a computer code was written that accurately modeled the auroral environment as realistically as possible. The code uses techniques originally designed for studying fusion plasmas, and extends the techniques for use on space plasmas. The simulation models the auroral plasma as large numbers of finite-size plasma clouds moving in their own self-consistently computed electric field. The magnetic field is applied and the ionosphere is modeled as a thin, infinite, conducting boundary. At initialization, the current

sheet is placed near the ionosphere, but no accelerating potential is assumed.

In the group of simulations made in a plane perpendicular to the ionosphere, the plane including the V-potential structure, the accelerating potential was allowed to evolve self-consistently as a result of the interaction between the electron current sheet, the ambient shielding ions, and the conducting ionosphere. The resulting V-shaped potential structure was analyzed and found to be a two-dimensional auroral double layer. A two-dimensional auroral double layer incorporates all the previously studied acceleration mechanisms. The previously proposed mechanisms include electrostatic shocks, double layers, anomalous resistivity, thermoelectric effect and pitch angle anisotropy. The simulation demonstrated that the double layer process dominates, but the other mechanisms are present. Thus, the more general term, "auroral" double layer, is used for the V-shaped potential structure.

The most important result in the simulations is that the accelerating potential forms spontaneously. Thus, this is the first study to show that the auroral acceleration mechanism is a natural consequence of the magnetospheric and ionospheric boundary conditions interacting with auroral plasma. Previous studies concentrated on either time independent models of a particle mechanism or time-dependent one-dimensional models of double layers without including the auroral boundary conditions.

In addition, the simulation demonstrates the important role of the earth's converging dipole field. When a uniform magnetic field was used in the simulation the accelerating potential was concentrated near the ionosphere. When a converging field was added the potential drop became distributed over the length of the simulation. A distributed acceleration region better agrees with satellite and barium release measurements. The reason the converging field extends the length of the double layer is that a new population of electrons develops that is trapped between the mirror on the accelerating potential. As the population develops the "Block" criterion for localized double layers is relaxed and the "Kan and Lee" criteria for extended double layers become satisfied.

The simulation shows that anomalous resistivity effects are not required. This is demonstrated by the simulation with zero initial current drift velocity, because the initial drift speed is below the threshold velocity for all proposed mechanisms. The proposed mechanisms include current driven ion-acoustic, ion-cyclotron, and two stream electron-ion (Buneman) instabilities. In the simulations with higher drift velocities, resistivity effects were observed. This indicates anomalous resistivity may not be required for auroral acceleration, but may be operative when the field-aligned current is large. When resistivity effects were observed they were identified as the Buneman instability. Ion-acoustic waves were damped to the high thermal motions of the ions. Ion-cyclotrons were not observed for two reasons. The first reason is the thickness of the current sheet was small compared to

the ion gyroradius and therefore the cyclotron motion of the ions was less important than the non-adiabatic motion of the ions as they tried to shield the electric field of the magnetized electrons. A possible second reason for the absence of ion cyclotron waves is that the simulation used an unrealistic low mass ratio (to save computer time) and this mass ratio may have limited the growth of the waves. The growth rate of ion-cyclotron waves is mass ratio dependent.

Fluctuations of the accelerating potential were observed to be due to two mechanisms. The most often observed fluctuation was due to the saturation of Buneman waves. The second mechanism occurred when the upward accelerated ions interacted with the ambient ions in an ion-ion two stream fashion. This mechanism may become more important in future simulations with longer grid sizes, which model larger regions of space. In addition to fluctuations, the accelerating potential was unstable if the incident flux of any particle population varied in time, with the exception of the ionospheric electrons. The flux of the ionospheric electron must be allowed to vary in order to insure charge neutrality (the number of electrons must equal the number of ions) in the simulation.

The second group of simulations, which make up Chapter 4, deal with the formation of the small scale auroral forms known as curls and folds. These simulations are performed in a plane parallel and elevated above the ionosphere. The unique feature of these simulations is the use of a realistic mass ratio for the ambient ions. Previous studies had not included the ions at all. The inclusion of the ions has yielded

the first evidence that the two auroral forms (curls and folds) are closely related. Curls form when the ions are "unmagnetized" and do not play an active role in the long term development of the instability. When the ions are magnetized, (which occurs whenever the ion gyroradius is small compared to the sheet thickness) the ions modify the deformation shape in its later stages of development. The ions do this because their finite gyroradius and large mass allows them to lag behind the deforming sheet, forming regions of positive space charge in the wake of the collective electron deformations. This small positive space charge is sufficient to limit the "twisting" of the vortices and make them elongate into a series of folds. As the folds develop, the sheet thins allowing further deformations to grow. Hence, curls can grow out of folds once the sheet is thin enough. This progression is observed in T.V. measurements.

In addition to studying auroral forms, this group of simulations have shown that damped ion-plasma waves, and ion-cyclotron waves are present due to the non-equilibrium initial conditions and finite geometry of the sheet.

5.2 Suggestions for Future Research

While the simulations discussed in this thesis offer new insight in the understanding of the auroral process, the modeling and simulation of auroral processes are still in their infancy. As computer capabilities increase and algorithms become more advanced new simulations will become more realistic and broader in scope.

Obvious extensions to the present work include using realistic mass ratio and larger systems to model the auroral environment more accurately. As mentioned earlier, some important effects may not have been seen in the simulations because the simulation had to be scaled down (for economic reasons).

The study of thick sheets ($a \gg \rho_i$) is possible with no changes in the simulation code. A simulation with a thick electron sheet would determine whether or not current driven ion cyclotron waves are capable of filamenting the sheet into multiple parallel arcs. This filamentation mechanism has been suggested by Kan and Lee (1981).

Other important extensions of this work include fully three-dimensional simulations, the use of a finite thickness ionosphere, and the use of a finite conductivity ionosphere. Since magnetosphere-ionosphere coupling is not well understood, simulations which include the convection flow of the magnetosphere and the finite conductivity of the ionosphere may help explain why field-aligned currents flow naturally in the magnetosphere-ionosphere system. In this thesis the current flow was assumed to be determined by the current source and the details of its creation and existence was not studied.

References

- Akasofu, S.-I. and D.S. Kimball, The dynamics of the aurora - instabilities of the aurora, J. Atmosph. Terr. Phys., 26, 205, 1967.
- Akasofu, S.-I., Recent progress in studies of DMSP auroral photographs, Space Sci. Rev., 19, 169, 1976.
- Akasofu, S.-I., Physics of Magnetospheric Substorms, D. Reidel Publ. Co., Holland, 1977.
- Albano, R.K., L.C. Lee, and J.R. Kan, Non-neutral field-aligned current sheet and the auroral electric field, J. Atmos. Terr. Phys., 42, 317, 1979.
- Alfvén, H., Cosmical Electrodynamics, Oxford Univ. Press, New York, (206), 1958.
- Alfvén, H. and C.-G. Fälthammar, Cosmical Electrodynamics, Fundamental Principles, p. 162, Clarendon Press, Oxford, 1963.
- Anderson, D., M. Babic, S. Sandahl, and S. Toren, Proceedings of the Ninth International Conference of Phenomena in Ionized Gases, Romania, 1969.
- Anderson, H.R. and R.R. Vondrak, Observations of Birkeland currents at auroral altitudes, Rev. Geophys. Space Phys., 13, 243, 1975.
- Arnoldy, R.L., P.B. Lewis, and P.O. Issacson, Field-aligned auroral electron fluxes, J. Geophys. Res., 79, 4208, 1974.
- Arnoldy, R.L., Auroral particle precipitation and Birkeland currents, Rev. Geophys. Space Phys., 12, 217, 1974.

- Baker, K.D., L.P. Block, R. Kist, and W. Kampa, Strong laboratory double layers and their relevance to auroral plasma physics, Proc. ICPP, 417, 1980.
- Birdsall, C.K. and D. Fuss, Clouds in clouds, clouds in cells, Physics for Many-Body Plasma Simulations, J. Comp. Phys., 3, 494, 1969.
- Block, L.P., Potential double layers in the ionosphere, Cosm. Electrodyn., 3, 349, 1972.
- Böhmer, H. and S. Fornaca, Experiments on nonlinear effects of strong ion cyclotron wave turbulence, J. Geophys. Res., 84, 5234, 1979.
- Boström, R., Ionosphere-magnetosphere coupling in Magnetospheric Physics, ed. by B.M. McCormac, D. Reidel Publ. Co., Dordrecht-Holland, 1974.
- Buneman, O., Dissipation of currents in ionized media, Phys. Rev., 115, 503, 1959.
- Buneman, O., R.H. Levy, and L. Linson, The stability of crossed-field electron beams, J. Appl. Phys., 37, 3203, 1966.
- Busnardo-Neto, J., P.L. Pritchett, A.T. Lin, and J.M. Dawson, A self-consistent magnetostatic particle code for numerical simulation of plasmas, J. Comp. Phys., 23, 300, 1977.
- Cattell, C.A., M.K. Hudson, R.L. Lysak, M. Temerin, R.B. Torbert, and F.S. Mozer, Measurements of mechanisms associated with low altitude auroral particle acceleration by the S3-3 satellite, EOS, AGU 60, 18, 346, 1979.

- Chiu, Y.T., J.M. Cornwall, and M. Schulz, Auroral magnetosphere-ionosphere coupling: A brief topical review, Solar-Terrestrial Predictions Proceedings, ed. R.F. Donnelly, Vol. 2, p. 494, NOAA, Boulder, Co., 1980.
- Cloutier, P.A., H.R. Anderson, R.J. Park, R.R. Vondrak, R.J. Spiger, and B.R. Sandel, Detection of geomagnetically aligned currents associated with an auroral arc. J. Geophys. Res., 75, 2595, 1970.
- Cloutier, P.A., B.R. Sandel, H.R. Anderson, P.M. Pazich, and R.J. Spiger, Measurement of auroral Birkeland currents and energetic particle fluxes, J. Geophys. Res., 78, 640, 1973.
- Coakley, P. and N. Hershkowitz, Laboratory double layer, Phys. Fluids, 22, 1171, 1979.
- Cutler, C.C., Instability in hollow and strip electron beams, J. Appl. Phys., 27, 1028, 1956.
- Davis, T.N., Observed characteristics of auroral forms, Space Sci. Rev., 12, 77, 1978.
- Dawson, J., Princeton University Plasma Physics Lab., Reports MATT-4 (1959) and MATT-31 (1960).
- Dawson, J., One dimensional plasma model, Phys. of Fluids, 5, 445, 1962.
- Dawson, J.M., C.G. Hsi, and R. Shanny, Princeton University Plasma Physics Laboratory, Report MATT-719 (1969).

- Dawson, J., The electrostatic sheet model for a plasma and its modification to finite size particles, Methods in Computational Physics, Vol. 9, ed. by Alder, Fernbach, and Rotenburg, Academic Press, New York, p. 1, 1970.
- Decyk, V.K., Computer simulation study of waves in bounded plasmas with application to lower hybrid heating, Thesis, UCLA, 1977.
- Decyk, V.K. and J.M. Dawson, A computer model for a bounded plasma, J. Comp. Phys., 30, 407, 1979.
- DeGroot, J.S., G. Barnes, and A.E. Walstead, and O. Runeman, Localized structures and anomalous dc resistivity, Phys. Rev. Lett., 38, 1283, 1977.
- Denavit, J., Electromagnetic particle simulation, J. Comp Phys., 15, 449, 1974.
- Eldridge, O.C. and M. Feix, One-dimensional plasma model at thermodynamic equilibrium, Phys. of Fluids, 5, 1076, 1962.
- Fälthammar, C.-G., Generation mechanisms for magnetic-field-aligned electric fields in the magnetosphere, J. Geomag. Geoelectr., 30, 419, 1978.
- Fejer, J.A. and J.R. Kan, A guiding center Vlasov equation and its application to Alfvén waves, J. Plasma Phys., 3, 331, 1969.
- Feldstein, Y.I., Some problems concerning the morphology of auroras and magnetic disturbances at high latitudes, Geomag. Aeronom., 3, 183, 1963.
- Forslund, D.W. and C.R. Shonk, Formation and structure of electrostatic collisionless shocks, Phys. Rev. Lett., 25, 1699, 1970.

- Frank, L.A. and K.L. Ackerson, Observations of charged particle precipitation into the auroral zone, J. Geophys. Res., 76, 3612, 1971.
- Fridman, M. and J. Lemaire, Relationship between auroral electron fluxes and field-aligned electric potential difference, J. Geophys. Res., 85, 664, 1980.
- Goertz, C.K. and G. Joyce, Numerical simulation of the plasma double layer, Astrophys. Space Sci., 32, 165, 1975.
- Goertz, C.K. and R.W. Boswell, Magnetosphere-ionosphere coupling, J. Geophys. Res., 84, 7239, 1979.
- Gurnett, D.A., Electric field and plasma observations in the magnetosphere, in Critical Problems of Magnetospheric Physics, ed. by E.R. Dyer, 123, Nat. Acad. Sci., Washington, D.C., 1972.
- Gurnett, D.A. and L.A. Frank, A region of intense plasma wave turbulence on auroral field lines, J. Geophys. Res., 82, 1031, 1977.
- Gurnett, D.A., Electromagnetic plasma wave emissions from the auroral field lines, J. Geomagnet. and Geoelectr., 30, 257, 1978.
- Haber, I., C.E. Wagner, J.P. Boris, and J.M. Dawson, Proceedings of the Fourth Conference on Numerical Simulation of Plasma, p. 126, 1970.
- Haerendel, G., First observations of electrostatic acceleration of barium ions, European sounding-rocket research, 203, ESA, Nevilly, France, 1976.
- Hallinan, T.J. and T.N. Davis, Small-scale auroral arc distortions, Planet. Space Sci., 18, 1735, 1970.

- Hallinan, T.J., Small-scale auroral arc distortions, M.S. Thesis, Univ. of Alaska, Fairbanks, 1970.
- Hasegawa, A., Plasma Instabilities and Nonlinear Effects, Springer-Verlag, Berlin, Heidelberg, 129, 1975.
- Hasegawa, A. and H. Okuda, One-dimensional plasma model in the presence of a magnetic field, Phys. of Fluids, 11, 1995, 1968.
- Hasegawa, A., Particle acceleration by MHD surface waves and the formation of aurora, J. Geophys. Res., 81, 5083, 1976.
- Hockney, R.W., Computer experiment of anomalous diffusion, Phys. of Fluids, 9, 1826, 1966.
- Hubbard, R.F. and G. Joyce, Simulation of auroral double layers, J. Geophys. Res., 84, 4297, 1979.
- Hudson, M.K. and F.S. Mozer, Electrostatic shocks, double layers, and anomalous resistivity in the magnetosphere, Geophys. Res. Lett., 5, 131, 1978.
- Hudson, M.K., R.L. Lysak, and F.S. Mozer, Magnetic field-aligned potential drops due to electrostatic ion cyclotron turbulence, Geophys. Res. Lett., 5, 143, 1978.
- Hultqvist, B., On the interaction between the magnetosphere and the ionosphere, in Solar-Terrestrial Physics/Proc. of the International Symp., Leningrad, USSR, May 11-19, 1970, ed. by E.R. Dyer, pp. 176-198, D. Reidel, Dordrecht-Holland, 1972.
- Hultqvist, B., The hot ion component of the magnetospheric plasma and some relations to the electron component - observations and physical implications, Space Sci. Rev., 23, 581, 1979.

- Iijima, T. and T.A. Potemra, Large-scale characteristics of field-aligned currents associated with substorms, J. Geophys. Res., 81, 3999, 1976.
- Iizuka, S., K. Saeki, N. Sato, and Y. Hatta, Buneman instability, Pierce instability, and double layer formation in a collisionless plasma, Phys. Rev. Lett., 43, 1404, 1979.
- Ionson, J.A., R.S.B. Ong, and E.G. Fonthem, Anomalous resistivity of the auroral plasma in the topside ionosphere, Geophys. Res. Lett., 3, 549, 1976.
- Jackson, J.D., Classical Electrodynamics, John Wiley and Sons, New York, p. 593, 1975.
- Jones, V., Aurora, D. Reidel Pub. Co., Dordrecht-Holland, 136, 1974.
- Joyce, G. and R.F. Hubbard, Numerical simulation of plasma double layers, J. Plasma Phys., 20, 391, 1978.
- Kan, J.P., Energization of auroral electrons by electrostatic shock waves, J. Geophys. Res., 80, 2089, 1975.
- Kan, J.R., L.C. Lee, and S.-I. Akasofu, Two-dimensional potential double layers and discrete auroras, J. Geophys. Res., 84, 4305, 1979.
- Kan, J.R. and L.C. Lee, On the auroral double layer criterion, J. Geophys. Res., 85, 788, 1980a.
- Kan, J.R. and L.C. Lee, Double-layer criterion on the altitude of the auroral acceleration region. Geophys. Res. Lett., 7, 429, 1980b.
- Kan, J.R. and L.C. Lee, The formation of auroral arcs and inverted V-precipitation: an overview, The Physics of Auroral Arc Formations, AGU, 1981.

- Kindel, J.M. and C.F. Kennel, Topside current instabilities, J. Geophys. Res., 76, 3055, 1971.
- Knight, S., Parallel electric fields, Planet. Space Sci., 31, 209, 1974.
- Knorr, G. and C.K. Goertz, Existence and stability of strong potential double layers, Astrophys. Space Sci., 31, 209, 1974.
- Kyhl, R.L. and H.F. Webster, Breakup of hollow cylindrical electron beams, IRE Trans. Electron Devices, 3, 172, 1956.
- Langdon, A.B., Birdsall, C.K., Theory of plasma simulation using finite size particles, Phys. of Fluids, 13, 2115, 1970.
- Langmuir, I., The interaction of electron and positive ions space charges in cathode sheaths, Phys. Rev., 33, 954, 1929.
- Lee, W.W. and H.Okuda, A simulation model for studying low frequency microinstabilities, Princeton Plasma Physics Lab Report, MATT 1231, 1976.
- Lemaire, J. and M. Scherer, Ionosphere-plasma sheet field-aligned currents and parallel electric fields, Planet. Space Sci., 72, 1485, 1974.
- Levine, J.S., D.B. Ilić, and F.W. Crawford, Laboratory observations of plasma double layers, J. Geomag. Geoelectr., 30, 461, 1978.
- Levine, J.S. and F.W. Crawford, A fluid description of plasma double-layers, J. Plasma Phys., 23, 223, 1980.
- Levy, R.H. and R.W. Hockney, Computer experiments on low density crossed-field electron beams, Phys. Fluids, 11, 766, 1968.

- Lin, A.T., J.M. Dawson, and H. Okuda, Application of electromagnetic particle simulation to the generation of electromagnetic radiation, Phys. of Fluids, 17, 1995, 1975.
- Lin, C.S. and R.A. Hoffman, Characteristics of the inverted V event, J. Geophys. Res., 84, 1514, 1979.
- Matsuda, Y., H. Okuda, Collisions in multi-dimensional plasma simulations, Phys. of Fluids, 18, 740, 1975.
- Mason, R.J., Computer simulation of ion-acoustic shocks, II. Slug and piston problems, Phys. Fluids, 15, 845, 1972.
- Meng, C.-I., Electron precipitations and polar auroras, Space Sci. Rev., 22, 223, 1978.
- Moiseev, S.S. and R.Z. Sagdeev, Collisionless shock waves in a plasma in a weak magnetic field, Plasma Phys., 5, 43, 1963.
- Montgomery, D. and G. Joyce, Shock-like solutions of the electrostatic Vlasov equations, J. Plasma Phys., 3, 1, 1969.
- Mozer, F.S., Magnetospheric dc electric fields, the scientific satellite program during IMS, D. Reidel Pub. Co., 101, Hingham, Mass., 1976.
- Mozer, F.S., C.W. Carlson, M.K. Hudson, R.B. Torbert, B. Parody, Y. Yatteau, and M.C. Kelley, Observations of paired electrostatic shocks in the polar magnetosphere, Phys. Rev. Lett., 38, 292, 1977.
- Nielson, C.W. and H.R. Lewis, Methods in Computational Physics, Vol. 16, ed. by Alder, Fenbark and Rotenburg, Academic Press, New York, p.367, 1976.

- Okuda, H. and C.K. Birdsall, Collisions in a plasma of finite-size particles, Phys. of Fluids, 13, 2123, 1970.
- Okuda, H., Finite size particles in plasma simulations, J. Comp. Physics, 10, 475, 1972.
- Okuda, H., C.Z. Cheng, W.W. Lee, Anomalous diffusion and ion heating in the presence of electrostatic hydrogen cyclotron instabilities, Physics of Auroral Arc Formations, AGU Monograph, 1981.
- Omholt, A., The Optical Aurora, Springer-Verlag, New York, 1971.
- Papadopoulos, K., A review of anomalous resistivity for the ionosphere, Rev. Geophys. Space Phys., 15, 113, 1977.
- Persson, H., Electric field along a magnetic line of force in a low-density plasma, Phys. Fluids, 6, 1756, 1963.
- Persson, H., Electric field parallel to the magnetic field in a low-density plasma, Phys. Fluids, 9, 1090, 1966.
- Pierce, J.R., Instability of hollow beams, IRE Trans. Electron Devices, 3, 183, 1956.
- Ponyavin, D.I., M.I. Pudovkin, and S.S. Sazhin, Self-consistent field-aligned electric field in the earth's magnetosphere, Geomag. and Aeron., 17, 323, 1977.
- Quon, B.M. and A.Y. Wong, Formation of potential double layers in plasmas, Phys. Rev. Lett., 37, 1393, 1976.
- Rees, M.H., Magnetospheric substorm energy dissipation in the atmosphere, Planet. Space Sci., 23, 1589, 1975.
- Sakanaka, P.H., C.K. Chu, and T.C. Marshall, Formation of ion-acoustic collisionless shocks, Phys. Fluids, 14, 611, 1971.

- Sato, T. and H. Okuda, Ion acoustic double layers, Phys. Rev. Lett., 44, 740, 1980.
- Shawhan, S.D., C.-G. Fälthammar, and L.P. Block, On the nature of large auroral zone electric fields at $1R_E$ altitude, J. Geophys. Res., 83, 1049, 1978.
- Singh, N., Reflection of probing beams by an electric double layer, Cospar Space Research, 20, Pergamon Press, 1980.
- Singh, N. and H. Thiemann, Some features of inverted V events as seen from simulated double layers, Geophys. Res. Lett., (accepted), 1980.
- Stamnes, K., On the discrete ordinate method for radiative transfer calculations in anisotropically scattering atmospheres, Geophysical Institute Scientific Report, UAG R-272, 1980.
- Stenzel, R.L., M. Ooyama, and Y. Nukamura, V-shaped potential double layers in a strongly magnetized laboratory plasma, EOS, 61, 1083, 1980.
- Störmer, C., The Polar Aurora, Oxford Univ. Press, Oxford, 1955.
- Swift, D.W., On the formation of auroral arcs and acceleration of auroral electrons, J. Geophys. Res., 80, 2096, 1975.
- Tajima, T. and L.C. Lee, Bounded electromagnetic simulation and the Budden turning point technique, UCLA Report, 1980.
- Torvén, S. and M. Babić, Current chopping space charge layers in a low pressure arc plasma, Proc. 12th Int. Conf. on Phenomena in Ionized Gases, Einhoven, Netherlands, Aug. 18-22, North-Holland Publ. Co., 1975.

- Wagner, J.S., T. Tajima, J.R. Kan, J.N. Leboeuf, S.-I. Akasofu, and J.M. Dawson, V-potential double layers and the formation of auroral arcs, Phys. Rev. Lett., 45, 803, 1980.
- Wagner, J.S., L.C. Lee, T.J. Hallinan, S.-I. Akasofu, and T. Tajima, The formation of auroral folds, J. Geophys. Res., (to be submitted), 1981.
- Wagner, J.S., T. Tajima, J.R. Kan, J.N. Leboeuf, S.-I. Akasofu, and J.M. Dawson, V-potential double layers and auroral arc deformations, The Physics of Auroral Arcs, AGU Monograph, 1981.
- Webster, H.F. and T.J. Hallinan, Instabilities in charge-sheets and current sheets and their possible occurrences in the aurora, Radio Sci., 8, 475, 1973.
- Wescott, E.M., H.C. Stenbaek-Nielsen, T.N. Davis, and H.M., Peek, The Skylab barium plasma injection experiments 1. Convection observations, J. Geophys. Res., 81, 4487, 1976.
- Whipple, E.C., The signature of parallel electric fields in a collisionless plasma, J. Geophys. Res., 82, 1525, 1977.